Light-induced dynamics in correlated quantum systems

Dissertation

with the aim of achieving a doctoral degree
at the Faculty of Mathematics, Informatics and Natural Sciences
I. Institut für Theoretische Physik
Universität Hamburg

submitted by

Maximilian Hollstein

Hamburg

2016

This page is intentionally left blank.

Gutachterin/Gutachter der Dissertation:	Prof. Dr. Daniela Pfannkuche Prof. Dr. Robin Santra
Zusammensetzung der Prüfungskommission:	Prof. Dr. Daniela Pfannkuche Prof. Dr. Robin Santra Prof. Dr. Markus Drescher Prof. Dr. Wolfgang Hansen Dr. habil. Michael Martins
Vorsitzender der Prüfungskommission:	Prof. Dr. Wolfgang Hansen
Datum der Disputation:	28.03.2017
Vorsitzender des Fach-Promotionsausschusses PHYSIK:	Prof. Dr. Wolfgang Hansen
Leiter des Fachbereichs PHYSIK:	Prof. Dr. Michael Potthoff
Dekan der Fakultät MIN:	Prof. Dr. Heinrich Graener

This page is intentionally left blank.

Hiermit erkläre ich an Eides statt, dass ich die vorliegende Dissertationsschrift selbst verfasst und keine anderen als die angegebenen Quellen und Hilfsmittel benutzt habe.

Hamburg, den

This page is intentionally left blank.

to Karin and Karl-Heinz

This page is intentionally left blank.

Acknowledgments

I owe my deepest gratitude to my supervisor Daniela Pfannkuche for her continued support and advice without which this thesis would not have been possible. I am grateful for the long enlightening discussions about physics that usually made me view aspects of my research from a different perspective and in a new light. I am greatly indebted to Robin Santra for many clarifying discussions and advices and I am grateful that I could profit from his extensive knowledge concerning atomic and molecular physics. Discussions with him triggered many of my investigations whose results are presented in this thesis and also resulted in a fruitfull collaboration concerning correlation-driven charge migration following double ionization and attosecond transient absorption spectroscopy. Moreover, I would like to thank my collaborators Karolin Mertens, Nils Gerken, Stephan Klumpp, Steffen Palutke, Ivan Baev, Günter Brenner, Siarhei Dziarzhytski, Wilfried Wurth and Michael Martins who performed the interesting experiment at FLASH concerning CH_2I_2 and CH_3I molecules. I am particularly grateful to Karolin Mertens for the many explanations concerning the details of their experimental approach. Special thanks goes to Benjamin Baxevanis for advising me as a research student and during my time as diploma student. I would like to thank Mohammad Sayad for many recreational coffee breaks and Lars-Hendrik Frahm for proofreading my manuscripts. Furthermore, I would also like to express my gratitude to Benjamin Baxevanis, Christoph Hübner, Holger Niehaus, Lars-Hendrik Frahm and Daniel Duarte for the many non-physics discussions at lunch time as well as to all past and present members of the Pfannkuche group responsible for a nice working atmosphere. The rapid and flexible assistance in IT matters by Bodo Krause-Kyora, Michael Vedmedenko, Michael Richter and Martin Stieben is gratefully acknowledged.

Finally, I would like to thank the referees and the members of the examination commission for their time and the work they put into the review process.

This page is intentionally left blank.

Publications

This thesis is based on the following publications:

1. **Multielectron dynamics in the tunneling ionization of correlated quantum systems**—Maximilian Hollstein and Daniela Pfannkuche— Phys. Rev. A 92, 053421—20 November 2015

2. **Exceptionally strong correlation-driven charge migration and attosecond transient absorption spectroscopy**—Maximilian Hollstein, Robin Santra, Daniela Pfannkuche— arXiv:1605.06762 [physics.chem-ph]—22 May 2016

3. **Ultrafast charge redistribution in small iodine containing molecules**—Maximilian Hollstein, Karolin Mertens, Nils Gerken, Stephan Klumpp, Steffen Palutke, Ivan Baev, Günter Brenner, Siarhei Dziarzhytski, Wilfried Wurth, Daniela Pfannkuche, Michael Martins—arXiv:1605.09317[physics.chem-ph]—30 May 2016

This page is intentionally left blank.

Abstract

The motion of electrons is at the heart of a vast number of fundamental processes ranging from the formation and the breaking of chemical bonds to the transfer of energy and charge within and between atoms and molecules. At the very early stages during and following a light-matter interaction, prior to the onset of a significant displacement of the nuclei, the electron-electron interaction is of particular prominence potentially initiating diverse electron dynamics in molecular systems [1]. Triggering, observing as well as controlling these multi-electron dynamics by light-fields is anticipated to provide indepth insight into fundamental electronic processes and ultimately, it might result in novel pathways for controlling chemical reactions [2]. In this context, this thesis theoretically investigates the impact of multi-electron effects on light-induced electron dynamics and it is also addressed how these dynamics could be evidenced experimentally.

Two important and limiting situations are considered: First, quasi-adiabatic electron dynamics that accompany the ionization process caused by a strong, low-frequency light field—i.e., a situation that commonly occurs in strong-field experiments concerning atoms and molecular systems. In this thesis, theoretical considerations concerning a model system are presented revealing that strong-field ionization can be accompanied by correlated multi-electron motion that becomes the more prominent the larger the system's spatial extent is. Hence, in general, multi-electron dynamics during strong-field ionization can be expected to be the more prominent the larger the molecular system or nanostructure is that is exposed to intense low-frequency fields. Thus, these findings are relevant for the theoretical modeling and the understanding of strong-field ionization of a wide range of physically, chemically and biologically relevant systems.

The second limiting situation considered concerns sudden ionization that is followed by correlation-driven electron dynamics [1], i.e., electron dynamics that are only due to correlation and orbital relaxation. Such a situation occurs for instance when molecules become ionized due to their interaction with attosecond light pulses [3]. The experimental observation of these processes is still one of the central and outstanding issues of attosecond physics. In this thesis, this issue is addressed constructively by investigating how correlation-driven electron dynamics could potentially be monitored by attosecond

transient absorption spectroscopy (ATAS)—an experimental technique which is already feasible. The observed straightforward interpretability of the ATA spectra as well as the great detailedness with which electron dynamics are reflected in them allow to identify a promising route for future experiments aiming at the real-time dynamics of ultrafast charge transfer processes.

Moreover, the concept of correlation-driven charge migration [1] is extended to double ionization—a situation that is of particular importance since it commonly occurs in the course of electronic decay processes that are crucial for charge rearrangement in molecular systems. Here, it is demonstrated that in doubly ionized molecules, correlation-driven processes are of particular prominence. In contrast to single ionization, they are likely to be initiated even when the electrons are emitted from outer-valence orbitals.

Finally, with regard to a recent experiment[4], the charge state distributions arising after two sequential iodine-4d inner-shell ionization events of CH_2I_2 and CH_3I molecules are investigated theoretically. The experiment revealed a strong molecule specificity of the iodine charge state distributions emerging after fragementation. The theoretical considerations presented allow to identify two mechanisms that can cause this effect supporting the interpretation of the experimental data in terms of interatomic charge rearrangement.

Kurzfassung

Die Bewegung von Elektronen spielt eine zentrale Rolle in einer Vielzahl fundamentaler Prozesse. Zum Beispiel ist sie entscheidend bei der Bildung als auch bei dem Aufbrechen chemischer Bindungen und sie ist ausschlaggebend bei Energie- und Ladungstransfer zwischen und innerhalb von Atomen und Molekülen. In den frühen Stadien während und nach einer Licht-Materie Wechselwirkung, noch bevor sich Atomkerne nennenswert bewegen können, kann die Wechselwirkung zwischen den Elektronen eine facettenreiche Elektronendynamik in Molekülen hervorrufen [1]. Das Auslösen, die Beobachtung als auch die Kontrolle dieser Elektronendynamik durch Lichtfelder wird erwartungsgemäß tiefe Einblicke in fundamentale Prozesse erlauben und letztendlich könnten auf diese Weise neue Wege zur Kontrolle von chemischen Reaktionen gefunden werden [2]. In diesem Kontext wird in dieser Arbeit der Einfluss von Elektronenynamik, welche in essentieller Weise mehr als ein einzelnes Elektron involviert, auf lichtinduzierte Prozesse theoretisch untersucht. Es wird dabei auch untersucht wie diese Dynamik experimentell nachgewiesen werden könnte.

Dabei werden zwei wichtige Grenzfälle betrachtet: zum einen wird quasiadiabatische Elektronendynamik untersucht, die den Ionisationsprozess begleitet, welcher durch ein starkes, niedrig-frequentes Lichtfeld hervorgerufen wird. Das heißt, eine Situation wird betrachtet, die insbesondere Starkfeldexperimente mit Atomen und molekularen Systemen betrifft. Dabei wird herausgefunden, dass Starkfeldionisation eine korrelierte Elektronendynamik initieren kann, deren Bedeutung mit der örtlichen Ausdehnung des Systems, das durch das starke Feld ionisiert wird, zunimmt. Im Allgemeinen kann also erwartet werden, dass diese Art von korrelierter Elektronendynamik während der Starkfeldionisation eine um so größere Rolle spielt, desto größer das Quantensystem ist, welches intensiver niedrig-frequenter Strahlung ausgesetzt wird. Daher sind diese Resultate relevant für die theoretische Modellierung als auch für das Verständnis der Starkfeldionisation einer Vielzahl physikalisch, chemisch und biologisch relevanter Systeme.

Der zweite betrachtete Grenzfall betrifft plötzliche Ionization, welche gefolgt ist von korrelationsgetriebener Elektronendynamik [1], das heißt Elektronendynamik, die nur

aufgrund von Elektronenkorrelationen und orbitaler Relaxation hervorgerufen wird. Solch eine Situation kann zum Beispiel entstehen, wenn Moleküle mittels eines Attosekundenpulses ionisiert werden [3]. Die experimentelle Beobachtung dieser Prozesse ist zur Zeit jedoch immer noch eines der zentralen und ausstehenden Probleme der Attosekundenphysik. In dieser Arbeit wird untersucht, wie diese Prozesse experimentell mittels Attosekundenabsorptionsspektroskopie nachgewiesen werden könnten. Die beobachtete leichte Interpretierbarkeit der Spektren und die Detailliertheit, mit der Elektronendynamik wiedergegeben wird, weisen in eine vielversprechende Richtung für zukünftige Experimente.

Desweiteren wurde das Konzept der korrelationsgetriebener Ladungsmigration [1], welches 1999 für einfachionisierte Moleküle von Cederbaum et al. eingeführt wurde, für Zweifachionisation erweitert. Dabei wird demonstriert, dass korrelationsgetriebene Prozesse in zweifachionisierten Molekülen eine besonders wichtige Rolle spielen. Im Gegensatz zu einfachionisierten Molekülen findet diese Art von Prozessen in zweifachionisierten Molekülen üblicherweise auch dann statt, wenn ein Ionisationsprozess Elektronen aus der äusseren Valenzschale entfernt.

Zum Schluss wurden, im Bezug auf ein aktuelles Experiment [4], die Ladungsverteilungen theoretisch untersucht, welche in CH_2I_2 und CH_3I Molekülen nach zwei sequentiellen Innerschalenionisationen der Iod Atome entstehen. Im Experiment wurde eine starke Molekülspezifizität der sich ergebenden Ladungszustände der Iod Ionen gefunden. Die hier präsentierten theoretischen Betrachtungen erlaubten zwei Mechanismen zu identifizieren, welche den Ladungszustand nach einer Innerschalenionisation der Iod-Ionen stark beeinflussen und welche die Trends in den experimentellen Daten erklären können. Insbesondere wird durch die theoretischen Betrachtungen die Interpretation der Daten im Sinne einer interatomaren Ladungsumordnung unterstützt.

Contents

1 Introduction

Photoinduced processes in atoms, molecules and solid state samples play a key role in physics, chemistry and biology. In particular, they trigger a large variety of chemical reactions [5] which are the basis of processes with immense significance as for instance vision and photosynthesis. Moreover, they form the basis of important technical applications such as solar cells in which photoinduced charge transfer and light harvesting is essential [6–8]. Thereby, electronic motion is pivotal, being at the heart of fundamental processes involved, ranging from the formation and the breaking of chemical bonds to the transfer of energy and charge within and between atoms and molecules. In this context, particularly interesting is coherent electron dynamics which, for instance, plays an important role in energy transfer [9] and gives rise to highly efficient charge transfer processes [1, 10–14] that can operate without nuclear motion. Hence, these transfer processes can be extremely fast, taking place on the femtosecond to even the attosecond timescale. On these very short timescales on which essentially only the electrons arrange, the interaction between the electrons is of particular significance and it strongly determines their concerted motion. In particular, electron-correlation and relaxation are expected to give rise to complex and rich many-body electron dynamics following photo ionization [1, 10–13] causing positive charge induced by ionization to migrate throughout molecular ions.

Since the advent of attosecond pulses [15] at the turn of the millennium, the motion of electrons in atoms and molecules is becoming exposed to experimental investigation [16]. To date, coherent electron dynamics in atoms and molecules have been initiated in pioniering experiments by both strong-field ionization[3, 17] as well as attosecond pulses [18]. Still, most attosecond experiments that have been performed are based on the combination of an attosecond pulse and a strong infrared pulse so that usually the dynamics of electrons in atoms and molecules in the presence of the strongly perturbing infrared field were investigated. However, the advent of attosecond-pump attosecond-probe experiments is anticipated for the near future [19]; this will enable the investigation of electron dynamics that are specific to atomic and molecular systems. Strikingly, these newly emerging attosecond techniques are anticipated to provide the possibility for a

manipulation of electron dynamics on the attosecond timescale and thereby may possibly result in novel pathways towards controlling chemical reactions [2].

In this context, this thesis addresses aspects concerning light-induced multi-electron dynamics in atoms, molecules and nanostructures. In particular, the electron dynamics during ionization as well as those that occur subsequent to it are investigated. To date, theoretical considerations concerning electron dynamics following ionization have been focussed on singly ionized molecules [1, 10–13]. In this work, these kind of theoretical considerations are extended to the important situation concerning double ionization—i.e., a situation occurring in many fundamental processes, for instance as a result of secondary electron emission following a primary ionization event—a prominent electronic relaxation process commonly occurring after inner-shell ionization. Anticipating attosecond-pump attoscecond-probe experiments, it is also addressed how these typically strongly correlated electron dynamics could be observed experimentally. For this, theoretical considerations are performed that concern attosecond transient absorption spectroscopy applied to correlated electron dynamics. The results obtained from these considerations are remarkably positive with respect to the detailedness with which complex electron dynamics are reflected in the spectra. This allows to identify a highly promising route for future experiments aiming at the real-time dynamics of ultrafast charge transfer processes in molecular systems.

2 Multi-electron dynamics in strong-field tunnel ionization

The results presented in this chapter have been published in Ref. [20].

Introduction

The ionization of atomic and molecular systems by intense light fields initiates a variety of processes that are central in attosecond physics. Most prominently, strong-field ionization represents the first step of high harmonic generation [21] and it initiates valence electron motion in atomic and molecular ions [17, 18, 22].

For atoms, ionization is often remarkably well-described by single active electron theories (SAE[23–25]) or the time-dependent configuration interaction singles approach (TDCIS [26–28]). Within these theories, ionization is described by the emission of a single electron into the continuum, while the residual electrons are assumed to remain unaffected. That means, the remaining electrons are taken into account by a time-independent potential for the active electron (SAE) or they are kept residing in Hartree-Fock ground state orbitals of the field-free atom (TDCIS). However, the most weakly bound electrons in systems that consist of many atoms such as the valence electrons in molecules and atomic clusters [29] or the conduction band electrons in atom-like nanostructures, e.g. semiconductor quantum dots [30], often experience a comparably weak effective confining potential. That is, the potential which is constituted by the effective core potentials of the participating atoms in these systems confines the motion of these electrons only weakly compared to the core potential seen by the electrons confined in a single atom. As a consequence of the weak confinement, the electron-electron interaction can induce strong correlations between the electrons that are confined in these systems [31–35]. As a result, correlations between the electrons can be expected to play a role also during the exposure of these systems to light fields. In this situation, the electron-electron interaction may cause correlated electron dynamics which include more than a single actively participating electron. In this chapter, the strong-field ionization of such a correlated quantum system is investigated with the focus on ionization

in the low-frequency regime [36]. The central aspect addressed concerns if and under which circumstances, the strong-field tunnel ionization process is accompanied by multi-electron dynamics, i.e., electron dynamics that essentially involve more than a single electron. Specifically, the impact of field-induced multi-electron dynamics on the ionization probability—the key observable associated with the process—is studied. For this purpose, a model system is investigated that consists of two correlated electrons that are initially trapped in a smooth confining potential well with Gaussian spatial dependence as it is realized, for instance, in atom-like nanostructures [37]. To reveal multi-electron effects, the TDCIS approach, which restricts the dynamics to a single actively participating electron, is benchmarked against the solution of the time-dependent Schrödinger equation (TDSE) which, in contrast to TDCIS, allows for a description of dynamics that involve both electrons. Here, the comparison of the TDCIS result with that obtained from the solution of the TDSE is employed to reveal multi-electron processes and to quantify their importance. On basis of these considerations, multi-electron effects during the strong-field tunnel ionization process are evidenced in quantum systems in which the most weakly bound electrons experience a smooth confining potential well. It is demonstrated that these effects become the more important the wider this potential well is.

2.1 Model system

In contrast to the potential that is experienced by strongly bound electrons in atoms, the effective potential seen by weakly bound valence electrons in molecules or conduction band electrons in nanostructures can be very different to the bare Coulomb potential of the nuclei. The effective potential, in which these weakly bound electrons reside, is often rather smooth. In fact, in semiconductor quantum dots, the effective potential can be often modeled by a potential well with Gaussian spatial dependence [37, 38]. To study the ionization of systems in which the most weakly bound electrons experience such a smooth confining potential, in this chapter, the ionization of a model system is considered that is constituted by two electrons that are initially trapped in a potential well with Gaussian spatial dependence. All considerations are restricted to dynamics induced by a linearly polarized light field. Accordingly, the light-induced electron dynamics within the confining potential well are essentially one-dimensional. For this reason, the considerations presented in this chapter are restricted to a one-dimensional model. This reduction enables insight into the quantum dynamics associated with ionization at low computational cost. For atoms, this reduction to one-dimensional models is common

and by reproducing effects of the 3D-reality, it has already provided valuable insight into ionization processes (see for instance Refs. [39–42]). Referring to the spatial coordinate as x, the confining potential of the model system can be denoted by:

$$V(x) = -V_0 e^{-(\frac{x}{w})^2}. \tag{2.1}$$

Here, V_0 determines the depth and w the width of the confinement. To account for the interaction between the two electrons that are initially situated in this confining potential well, a softened Coulomb interaction is considered:

$$V_C(x_1, x_2) = \frac{1}{\sqrt{(x_1 - x_2)^2 + \delta^2}}. \tag{2.2}$$

Here, $x_{1,2}$ denote the spatial coordinates of the two electrons. By choosing δ different from zero, a finite width of the electronic wave function along the spatial dimensions, which are not included in the model, is taken into account in a phenomenological way [43, 44].

To jointly describe atomic and molecular systems as well as atom-like nanostructures that can be modeled by effective Hamiltonians using the effective mass approximation [37], an appropriate unit system is employed, which is termed in the following "effective atomic units". Essentially, this unit system is an extension of the well-known atomic units by allowing for an effective electron mass whose value does not necessarily coincide with the proper one and a dielectric constant that can be different from one (see the Appendix 7.0.1). Unless stated differently, all quantities are given in effective atomic units. Note that in SI-units, the values of the quantities considered are strongly system specific. Namely, for atoms and molecules, the unit system coincides with the well-known atomic units, i.e., for these systems one effective Hartree is 27.2 eV and an intensity of 1.0 in effective atomic units corresponds for these systems to $3.5 \times 10^{16} \frac{W}{cm^2}$. However, for example, for GaAs quantum dots, the effective electron mass is only 0.067 times the proper electron mass and the dielectric constant is 12.4, so that in these systems an effective Hartree is on the order of only $\sim$ 10 meV and an intensity of 1.0 corresponds there to only $\sim 2 \times 10^5 \ \frac{W}{cm^2}$ [38, 45].

For the considerations in the subsequent sections concerning the dynamics induced by a low-frequency laser field, it is necessary to characterize the model system in its low-energy regime. For this, it is expedient to approximate the model potential in the

vicinity of the potential minimum by a harmonic potential:

$$V(x) \approx \frac{1}{2}\Omega^2 x^2 - V_0. \tag{2.3}$$

Here, Ω denotes the oscillator frequency $\Omega = \frac{\sqrt{2V_0}}{w}$. The harmonic potential that is associated with the model potential in this way allows a convenient characterization of properties related to the ground state and the low-energy excited states. In particular, the harmonic approximation allows one to estimate the level spacing of the lowest bound states:

$$\Delta E \approx \Omega = \frac{\sqrt{2V_0}}{w}. \tag{2.4}$$

This introduces a characteristic energy scale for low-energy excitations. The harmonic approximation also provides a characteristic length scale l_0:

$$l_0 = \frac{1}{\sqrt{\Omega}} = \frac{\sqrt{w}}{\sqrt[4]{2V_0}}. \tag{2.5}$$

By means of these characteristic units (i.e., Ω and l_0), the field-free Hamiltonian in the harmonic approximation can be represented with dimensionless coordinates $\xi_{1,2} = \frac{x_{1,2}}{l_0}$ in the following way:

$$H \approx \Omega\left[-\frac{1}{2}\frac{\partial^2}{\partial\xi_1^2} - \frac{1}{2}\frac{\partial^2}{\partial\xi_2^2} + \frac{1}{2}\xi_1^2 + \frac{1}{2}\xi_2^2 + \frac{l_0}{\sqrt{(\xi_1-\xi_2)^2 + (\frac{\delta}{l_0})^2}}\right] - V_0 \tag{2.6}$$

In this representation, it becomes particularly transparent that with increasing characteristic length l_0, the strength of the electron-electron interactions increases monotonically with respect to the one-particle part of the Hamiltonian—i.e., with respect to $-\frac{1}{2}\frac{\partial^2}{\partial\xi_1^2} - \frac{1}{2}\frac{\partial^2}{\partial\xi_2^2} + \frac{1}{2}\xi_1^2 + \frac{1}{2}\xi_2^2$. It is important to note that for this reason, the impact of the electron-electron interaction depends on the spatial extension of the confinement. In fact, according to Eq. 2.6, one can expect that the importance of effects caused by the electron-electron interaction increases with increasing spatial extension (see also Ref. [46]).

Light-matter interaction

Strong-field tunnel ionization is typically induced by intense low-frequency laser fields whose wavelengths are much larger than the extent of the quantum system exposed to them. Therefore, the process is accurately described by the time-dependent Schrödinger

equation in dipole approximation:

$$i\frac{\partial}{\partial t}\Psi = H(t)\Psi. \tag{2.7}$$

Here, Ψ denotes the electronic wave function and $H(t)$ is the time-dependent Hamiltonian that includes the interaction of the quantum system with a classical, monochromatic and linearly polarized laser field. In length gauge, the Hamiltonian $H(t)$ including the interaction with the light field is then given by:

$$H_0 = -\frac{1}{2}\sum_{i=1}^{2}\frac{\partial^2}{\partial x_i^2} - V_0\sum_{i=1}^{2}e^{-(\frac{x_i}{w})^2} + \frac{1}{\sqrt{(x_1-x_2)^2+\delta^2}} \tag{2.8}$$

$$H(t) = \hat{H}_0 - \sum_{i=1}^{2}x_i E(t). \tag{2.9}$$

where H_0 denotes the Hamiltonian of the field-free system and $E(t)$ is the time-dependent electric field. In the following, an electric field with sinusoidal time dependence is considered:

$$E(t) = E_0\sin(\omega t). \tag{2.10}$$

Here, E_0 is the amplitude of the electric field and ω denotes the frequency. In the subsequent considerations also the period $T = \frac{2\pi}{\omega}$ of the light field will be considered.

Strong-field tunnel ionization occurs when atoms, molecules or solids are exposed to an intense low-frequency laser field, i.e., a field whose frequency is small compared to the excitation energy of the system exposed to it. It describes an ionization process in which electrons escape by tunneling through the effective potential barrier that is exhibited by the instantaneous potential $V(x_i,t)$ constituted by the confining potential and the potential associated with the instantaneous electric field:

$$V(x_i,t) = -V_0 e^{-(\frac{x_i}{w})^2} - E(t)x_i. \tag{2.11}$$

Characteristic for the process is that a significant part of the ionization can occur during a half-cycle of the laser field, namely, in the vicinity of the extrema of $E(t)$. An indicator for the tunnel ionization regime is the so-called Keldysh parameter [36] γ:

$$\gamma = \sqrt{\frac{I_p}{2U_p}}. \tag{2.12}$$

Here, I_p denotes the ionization potential, i.e., the minimum energy needed to promote an electron to a continuum orbital (in the situations considered, it is on the order of a few ΔE), and $U_p = \frac{E_0^2}{4\omega_0^2}$ is the ponderomotive energy, i.e., the cycle-averaged energy of a free electron in the laser field. For $\gamma \ll 1$, the ionization rate is given by a DC tunneling rate [36] characterizing the tunneling ionization process.

In the following considerations, the frequency ω is chosen as $2\pi \times 0.001$ so that the Keldysh parameter γ is smaller than 0.01 for the parameters considered (i.e., for $V_0 = 3$, $w \in [1, 5]$ $\omega = 2\pi \times 0.001$ and $E_0 = 0.3$). The parameter δ (cf. Eq. 2.2) is set to 0.5 effective atomic units.

Before presenting the numerical approach for a description of the ionization dynamics, a last remark concerns the electric field strength. It should be noted that for $|E(t)| \geq E_{crit}$ with

$$E_{crit} = \frac{V_0}{w}\sqrt{\frac{2}{e}}, \tag{2.13}$$

the instantaneous potential $V(t)$ does not possess a minimum and no potential barrier exists. In this situation, the ionization process cannot be understood by a tunneling process but by the escape of electrons via a classical trajectory. This situation is not considered in this work, i.e., the model parameters are chosen such that this situation does not occur. Relevant for the subsequent considerations, however, is the fact that E_{crit} decreases with increasing spatial extension of the system ($\sim \frac{1}{w}$). This indicates that the perturbation induced by the very same light field effectively increases with the system's spatial extension. Hence, an enlargement of the confinement width causes effectively an relative increase of the strength of both the light-matter interaction and as discussed before, the electron-electron interaction with respect to the confining potential. In the following sections, multi-electron dynamics that result from an interplay between these two interactions, i.e., electron-light and electron-electron interaction, are studied for various confining potential widths of the model system.

2.2 Numerical Treatment

To investigate the electron dynamics that are associated with the strong-field tunnel ionization of the model system considered, complementary numerical approaches and techniques were employed. These techniques concern the numerical solution of the time-dependent Schrödinger equation (TDSE), a numerical implementation of the time-dependent configuration interaction singles (TDCIS) approach and the analysis of the

wave functions—i.e., the wave function which solves the TDSE and the wave function obtained from the TDCIS approach. In this section, first, a few general aspects concerning the light-induced dynamics and the time-dependent wave functions as well as their theoretical analysis are discussed and second, the numerical approaches employed to solve the TDSE and to obtain the TDCIS wave function are presented.

Spin

Before going into the details concerning the numerical treatment, a few general considerations are in order. In this work, the situation is investigated in which the two-electron system is initially in the singlet ground state. It is important to note that a singlet two-electron wave function has the special property that it can be represented as a product of a spatial wave function $|\psi_{spatial}\rangle$ and a spin-singlet wave function $\frac{|\uparrow\downarrow\rangle - |\uparrow\downarrow\rangle}{\sqrt{2}}$ [47]:

$$|\psi\rangle = |\psi_{spatial}\rangle \times \frac{|\uparrow\downarrow\rangle - |\uparrow\downarrow\rangle}{\sqrt{2}}. \tag{2.14}$$

Since the time-dependent Hamiltonian given in Eq. 2.9 commutes with the total spin operator, considerations concerning the dynamics driven by a light-field can be restricted to the singlet subspace. In particular, this means that in the situation investigated, only the spatial wave function is time-dependent whereas the spin wave function remains constant. For this reason, the spin wave function will not be mentioned explicitly in the following. Only the spatial wave function will be considered.

Complex absorbing potential

Another aspect addressed concerns the fact that in the process investigated at least one electron becomes unbound and leaves the vicinity of potential well in which it was initially localized. In a numerical simulation of the process, freed electron(s) will inevitably reach the borders of a finite simulation box after a finite time (if a grid based approach is chosen) or cannot be represented by the finite basis set employed (if the wave function is expanded in terms of a finite set of basis functions). In any case, when the electronic wave function cannot be represented accurately anymore, observables obtained from the wave function are erroneous. These problems related to finite simulation boxes or finite basis sets can be reduced by the use of numerical techniques such as complex absorbing potentials or the (smooth) exterior scaling transformation [48, 49]. These techniques allow to accurately represent the wave function in the spatial region of interest while out-going wave packets, which leave the region, are effectively damped when having

spatial overlap with the complex absorbing potential or the region where the spatial coordinate is transformed. Therefore, these techniques prevent artificial reflections and allow the use of rather small simulation boxes which are only slightly larger than the region of interest.

In this work, a complex absorbing potential with the form of V_{CAP} was employed:

$$V_{CAP} = \begin{cases} -iC(||x| - x_0|)^3 & |x| > x_0 \\ 0 & else. \end{cases} \tag{2.15}$$

For the calculations presented below, C was chosen as 4×10^{-3} (The numerical convergence of the results with respect to C is demonstrated in the Appendix 7.0.2). x_0 was set to 15 where both the confining potential and the ground state wave function are only insignificantly different from 0 (i.e., for all model parameters considered ($w \leq 5$), the absolute value of confining potential is for x = 15 smaller than 0.001 and the value of the ground state density is decreased to $\lesssim 10^{-16}$).

Analysis of the time-dependent wave functions and ionization probability

A few remarks concerning the analysis of the strong-field tunnel ionization process are necessary. One should note that strong-field tunnel ionization occurs predominantly when the electric field of the laser is extremal and the potential barrier exhibited by the instantaneous potential is smallest. For this reason, the subsequent considerations are restricted to the dynamics during a (first) half-cycle of the light field. At the beginning of the half-cycle, the two electrons reside in the singlet ground state. To investigate the ionization process that is triggered when the light field is present, the electron dynamics within the potential well and its vicinity is considered. For this purpose, the restricted and renormalized wave function in Eq. 2.16 is studied:

$$\tilde{\Psi} = \frac{\Psi(x_1, x_2, t)|_{|x_{1,2}|<x_{max}}}{\sqrt{\int_{-x_{max}}^{x_{max}} \int_{-x_{max}}^{x_{max}} dx_1 dx_2 |\Psi(x_1, x_2, t)|^2}} \tag{2.16}$$

with

$$\Psi(x_1, x_2, t)|_{|x_{1,2}|<x_{max}} = \begin{cases} \Psi(x_1, x_2, t) & \text{if} \quad |x_{1,2}| < x_{max} \\ 0 & \text{else.} \end{cases} \tag{2.17}$$

Unless noted differently, x_{max} is chosen as 15 ($= x_0$). Before the two-electron system is exposed to the light field, both electrons are essentially situated in this area. However,

at later times, electron(s) are excited by the laser into the continuum and leave the spatial region. During the first half-cycle considered, electrons which tunneled through the potential barrier are only accelerated away from the confining potential minimum. This is reflected in the time-dependent norm:

$$||\Psi(x_1, x_2, t)|_{|x_{1,2}|<x_{max}}|| = \sqrt{\int_{-x_{max}}^{x_{max}} \int_{-x_{max}}^{x_{max}} dx_1 dx_2 |\Psi(x_1, x_2, t)|^2}, \tag{2.18}$$

which decreases monotonically (see Fig. 2.1). Note that it becomes stationary even

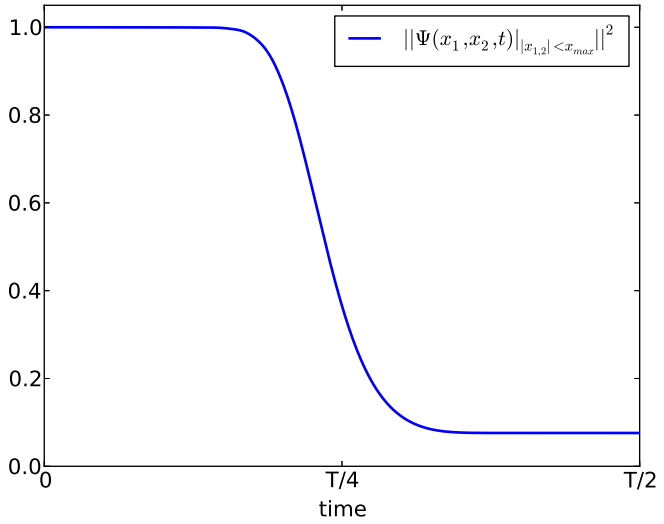

Figure 2.1: $||\Psi(x_1, x_2, t)|_{|x_{1,2}|<x_{max}}||^2$ (see Eq. 2.18) during the first half-cycle of the laser field for a confinement potential V (see Eq. 2.1) with $w = 5$. Here, $T = \frac{2\pi}{\omega}$ denotes the period of the considered light field; ω is the frequency of the light field (see Eq. 2.10).

before the end of the half-cycle indicating that the electron(s), which tunneled through the potential barrier, left the spatial region before the end of the half cycle. At the end of the half-cycle at t = T/2, the part of the wave function consisting of occupied continuum states has only an insignificant spatial overlap with the spatial region considered. This is reflected by the fact that, for all model parameter values used, the overlap of the renormalized restricted wave function and the field-free ground state is larger than 0.999. This allows one to numerically determine the ionization probability after the half-cycle

at $t = T/2$ by:

$$P_{ion}(T/2) \approx 1 - \int_{-x_{max}}^{x_{max}} \int_{-x_{max}}^{x_{max}} dx_1 dx_2 |\Psi(x_1, x_2, T/2)|^2. \tag{2.19}$$

General procedure for numerical time propagation

The last general aspect concerns the time-evolution with a time dependent Hamiltonian. In this work, this numerical issue was addressed in the following way: First, the time interval of interest was split into small time intervals Δt during which the Hamiltonian $H(t)$ is approximated by a time-independent operator H_τ:

$$H(t) \approx H(\tau + \Delta t/2) =: H_\tau \qquad \forall t \in [\tau, \tau + \Delta t] \tag{2.20}$$

Given an electronic state $|\psi_\tau\rangle = |\psi(t = \tau)\rangle$ at $t = \tau$, the time-evolved state during the small time interval $[\tau, \tau + \Delta t]$ can be determined (approximately) by application of the time-evolution operator $e^{-iH_\tau(t-\tau)}$:

$$|\psi(t)\rangle \approx e^{-iH_\tau(t-\tau)}|\psi_\tau\rangle \qquad \forall t \in [\tau, \tau + \Delta t]. \tag{2.21}$$

Clearly, Δt has to be chosen (much) smaller than the characteristic timescale associated with the model system $\sim \frac{1}{\Delta E}$ and the laser period T. The numerical convergence of the results presented in this chapter with respect to the length of the time interval Δt is demonstrated in the Appendix 7.0.2.

Time-dependent Schrödinger equation

In order to solve the TDSE numerically, in this work, a split operator technique [50] was employed. In this approach, the electronic state $|\psi\rangle$ is represented on a two-dimensional spatial grid $\psi(x_1, x_2) = \langle x_1, x_2|\psi\rangle$ and the time-evolution operator $e^{-iH_\tau(t-\tau)}$ is approximated by a product of exponential operators whose exponents depend either on the confining potential and the electron-electron interaction V_τ or the kinetic energy T:

$$e^{-iH_\tau(t-\tau)} \approx e^{-iT\frac{(t-\tau)}{2}} e^{-iV_\tau(t-\tau)} e^{-iT\frac{(t-\tau)}{2}} + \mathcal{O}((t-\tau)^3) \tag{2.22}$$

with

$$V_\tau = -V_0 \sum_{i=1}^{2} e^{-(\frac{x_i}{w})^2} - \sum_{i=1}^{2} x_i E(\tau + \Delta t/2) + \frac{1}{\sqrt{(x_1 - x_2)^2 + \delta^2}} \tag{2.23}$$

$$T = -\frac{1}{2}\frac{\partial^2}{\partial x_1^2} - \frac{1}{2}\frac{\partial^2}{\partial x_2^2}. \tag{2.24}$$

Since the kinetic energy and the potential operators do not commute, here, an error on the order of $\mathcal{O}(\Delta t^3)$ is made [50]. The convergence of the results with respect to the length of the time interval, is demonstrated in the Appendix 7.0.2.
Advantageously, in the spatial grid representation of the wave function, the potential and the electron-electron interaction are diagonal. This allows an efficient evaluation of $e^{-iV_\tau(t-\tau)}$:

$$\left[e^{-iV_\tau(t-\tau)}\psi\right](x_i, x_j) = e^{-iV(x_i,x_j)_\tau(t-\tau)}\psi(x_i, x_j). \tag{2.25}$$

Hence, the time complexity of the application of $e^{-iV_\tau(t-\tau)}$ is only $\mathcal{O}(N)$ where N is the total number of grid points. Thus, a very fast evaluation of $e^{-iV_\tau(t-\tau)}$ is possible. In order to evaluate $e^{\frac{-iT(t-\tau)}{2}}$ efficiently, ψ is transformed to momentum space by Fourier transformation. In particular, if the number of grid points is a power of two, this can be done very efficiently by fast Fourier transformation (FFT) with the time complexity $\mathcal{O}(Nlog(N))$. For the presented work, MATLAB's [51] implementation of the FFT was used. The application of $e^{\frac{-iT(t-\tau)}{2}}$ to the wave function represented in momentum space reduces to:

$$\left[e^{\frac{-iT(t-\tau)}{2}}\psi\right](k_i, k_j) = e^{-i(\frac{k_i^2}{2}+\frac{k_j^2}{2})\frac{(t-\tau}{2})}\tilde{\psi}(k_i, k_j) \tag{2.26}$$

where $\tilde{\psi}$ is the wave function represented on a grid in momentum space obtained from the FFT calculation. After application of $e^{-iT(t-\tau)}$ to $\tilde{\psi}$, the wave function, represented on the spatial grid, is obtained by employing the inverse FFT. Notably, the total time complexity of this algorithm that propagates the wave function from t to $t + \Delta t$ is only $\mathcal{O}(Nlog(N))$.

The ground state, which represents the initial state in which the system is prepared before its interaction with the light field, is obtained by imaginary time-evolution which is a commonly employed technique (see for instance [52]) based on the fact that propagation in imaginary time ensued by renormalization converges to the ground state. Notably, since the Hamiltonian H is symmetric with respect to the exchange of electron coordinates, the condition that the spatial wave function is symmetric with respect to the exchange of the electron coordinates so that the total wave function obeys Pauli's

exclusion principle, can be easily achieved by choosing a symmetric initial wave function for imaginary time evolution.

Time-dependent configuration interaction singles approach (TDCIS)

In order to demonstrate the impact of multi-electron dynamics on the tunnel ionization process, the solution of the time-dependent Schrödinger equation (TDSE), which describes the full dynamics in which both electrons actively participate, is compared with the time-dependent configuration interaction singles (TDCIS) approach [26–28]. TDCIS is an ab-initio approach in which the electronic wave function is restricted to the single-particle excitations with respect to the Hartree-Fock ground state determinant. Notably, TDCIS can be formulated as an effective one-electron theory [26]. In contrast to single active electron (SAE) approaches in which the electron-electron interaction is replaced by a potential, within the TDCIS approach the electron-electron interaction is taken into account rigorously—i.e., the exact many-body Hamiltonian is employed; the only approximation in TDCIS is the restriction of the configuration space. Importantly, this makes TDCIS superior to SAE approaches [26]. Hence, by representing an approach that is particularly suitable to describe accurately light-induced dynamics that involve essentially only a single electron, the comparison of the solution of the TDCIS equation of motion with the solution of the TDSE reveals multi-electron effects. In this chapter, a benchmark of TDCIS against the exact solution of the TDSE is employed to determine the impact of multi-electron effects on the ionization dynamics.

The two-electron spin-singlet TDCIS wave function is given by:

$$|\Psi\rangle = \alpha_0 |\Phi_0\rangle + \sum_{i>0} \alpha_0^i |\Phi_0^i\rangle \tag{2.27}$$

with the Hartree-Fock ground state determinant $|\Phi_0\rangle$ and the vacuum state $|0\rangle$:

$$|\Phi_0\rangle = c_{0\uparrow}^\dagger c_{0\downarrow}^\dagger |0\rangle \tag{2.28}$$

and

$$|\Phi_0^i\rangle = \frac{1}{\sqrt{2}}(c_{i\uparrow}^\dagger c_{0\uparrow} + c_{i\downarrow}^\dagger c_{0\downarrow}) |\Phi_0\rangle . \tag{2.29}$$

Here, $c_{0\uparrow}, c_{0\downarrow}$ denote annihilation operators of the spin orbitals which are occupied in the Hartree-Fock ground state determinant. $c_{i\uparrow}^\dagger, c_{i\downarrow}^\dagger$ denote creation operators of initially unoccupied orbitals (virtual orbitals). As mentioned above, a two-electron spin-singlet wave function can be represented as a product of a symmetric spatial and the anti-

symmetric spin wave function. The spatial part of the TDCIS singlet two-electron wave function is given by:

$$\Psi(x_1, x_2, t)_{TDCIS} = \sum_i \tilde{\alpha}_i(t)\big[\psi_0(x_1)\psi_i(x_2) + \psi_i(x_1)\psi_0(x_2)\big] \tag{2.30}$$

with

$$\tilde{\alpha}_i(t) = \begin{cases} \alpha_0(t)/2 & i = 0 \\ \alpha_0^i(t) & else \end{cases} \tag{2.31}$$

where ψ_i denote Hartree-Fock orbitals. ψ_0 denotes the spatial orbital that is doubly occupied in the Hartree-Fock ground state determinant. Note that in Eq. 2.30, it is particularly apparent that at all times, only one electron is active (i.e., only one electron can occupy an arbitrary orbital) while the other electron is forced to reside in the Hartree-Fock ground state orbital ψ_0.
To obtain the orbitals ψ_i, the Hartree-Fock equations have to be solved:

$$F\psi_i(x) = \epsilon_i\psi_i(x). \tag{2.32}$$

Here, ϵ_i denote the orbital energies and F is the closed-shell Fock operator of the two-electron model system:

$$F = -\frac{1}{2}\frac{\partial^2}{\partial x^2} + V(x) + \int \frac{|\phi_0(x_1)|^2}{\sqrt{(x_1 - x)^2 + \delta^2}} dx_1. \tag{2.33}$$

In order to determine Hartree-Fock orbitals ψ_i numerically, the Legendre pseudospectral method [49, 53] was employed. Within this method, functions $\phi(x)$ are approximated by an order N polynomial:

$$\phi(x) \approx \phi_N(x) = \sum_l^N a_l P_l(x) \tag{2.34}$$

where $P_l(x)$ are the Legendre polynomials. A pseudospectral method furthermore requires the approximation to be exact at the so-called collocation points x_i and represents $\phi_N(x)$ in terms of so-called cardinal functions $g_i(x)$

$$\phi_N(x) = \sum_{i=0}^N g_i(x)\phi(x_i) \tag{2.35}$$

which possess the property:

$$g_i(x_j) = \delta_{ij}. \tag{2.36}$$

The cardinal functions associated with the Legendre pseudospectral method are:

$$g_j(x) = \frac{-1}{N(N+1)P_N(x_j)} \frac{(1-x^2)P'_N(x)}{x - x_j} \tag{2.37}$$

and the collocation points x_i are the roots of the derivatives of the Legendre polynomials $P'_N(x)$ (see Ref. [53]).
The pseudospectral method requires the approximation to be exact at the collocation points so that by imposing the boundary conditions $\phi_0(x_0) = \phi_0(x_N) = 0$ and representing the Hartree-Fock orbitals in the form given in Eq. 2.35, the Hartree-Fock problem results in solving the equations:

$$\sum_{j=1}^{N-1} [\hat{F} g_j(x)|_{x=x_i} - \epsilon g_j(x)|_{x=x_i}] \phi_0(x_i) = 0. \tag{2.38}$$

These equations were solved self-consistently. Advantageously, $Fg_j(x)$ can be evaluated exactly with low computational effort, i.e., the second derivative of the cardinal functions can be determined analytically:

$$g''_j(x)|_{x=x_j} = \frac{-N(N+1)}{3(1-x_j)^2} \quad 1 \leq j \leq N-1 \tag{2.39}$$

$$g''_j(x)|_{x=x_i} = \frac{-2}{(x_i - x_j)^2} \quad 1 \leq i, j \leq N-1, i \neq j \tag{2.40}$$

and the potential V and also the Coulomb interaction term are diagonal in this representation:

$$V(x) g_j(x)|_{x=x_i} = \delta_{i,j} V(x_i) \tag{2.41}$$

$$\int \frac{|\phi_0(x_1)|^2}{\sqrt{(x_1 - x)^2 + \delta^2}} dx_1 g_j(x)|_{x=x_i} = \delta_{i,j} \int \frac{|\phi_0(x_1)|^2}{\sqrt{(x_1 - x_j)^2 + \delta^2}} dx_1. \tag{2.42}$$

For the calculations presented below, N was set to 400 (i.e., 400 cardinal functions were employed). The convergence of the calculations with respect to N is demonstrated in the Appendix 7.0.2.

The Hartree-Fock orbitals, which were obtained from solving the Eq. 2.38 numerically, were employed to construct the CIS subspace, i.e., the space spanned by the determinants

(see Eq. 2.27 and Eqs. 2.28,2.29):

$$\{|\Phi_0\rangle, |\Phi_0^i\rangle\} \quad i \in \{1, ..., N-1\} \tag{2.43}$$

The initial state within the TDCIS approach is the Hartree-Fock ground state, which represents the exact ground state of the field-free CIS Hamiltonian [49], i.e., the field-free Hamiltonian represented in the CIS subspace 2.43. The matrix elements are given by:

$$\langle\Phi_0|H|\Phi_0\rangle = E_{\mathrm{HF}} \quad \text{(Hartree Fock energy)} \tag{2.44}$$

$$\langle\Phi_0|H|\Phi_0^i\rangle = 0 \quad \text{(Brillouin theorem)} \tag{2.45}$$

$$\langle\Phi_0^i|H|\Phi_0^j\rangle = (\epsilon_0 + \epsilon_j)\delta_{ij} + \langle\Phi_0^i|V_C - V_{\mathrm{HF}}|\Phi_0^j\rangle \tag{2.46}$$

where $V_C - V_{\mathrm{HF}}$ denotes the residual electron-electron interaction representing the difference between bare electron-electron interaction V_C (see Eq. 2.2) and the Hartree-Fock mean field:

$$[V_C - V_{\mathrm{HF}}](x_1, x_2) = \frac{1}{\sqrt{(x_1 - x_2)^2 + \delta^2}} - \int \frac{|\psi_0(x_1)|^2}{\sqrt{(x_1 - x_2)^2 + \delta^2}} dx_1 - \int \frac{|\psi_0(x_2)|^2}{\sqrt{(x_1 - x_2)^2 + \delta^2}} dx_2. \tag{2.47}$$

The Hartree-Fock energy is given by:

$$E_{\mathrm{HF}} = 2\epsilon_0 - \int \frac{|\psi_0(x_1)|^2 |\psi_0(x_2)|^2}{\sqrt{(x_1 - x_2)^2 + \delta^2}} dx_1 dx_2 \tag{2.48}$$

ϵ_0 and ϵ_j represent the orbital energies (see Eq. 2.32). The one and two particle integrals needed to determine these matrix elements were obtained by numerical integration using the GSL library [54]. The time-evolved TDCIS wave function was obtained by iterative Lanczos reduction [55]. That means, that the time-evolution in time intervals $[t, t + \Delta t]$ during which the Hamiltonian was approximated by a time-independent operator, was restricted to a low-dimensional Krylov subspace:

$$\{\psi(t), H\psi(t), H^2\psi(t)...\} \tag{2.49}$$

(In the calculations presented, the dimension was set to 10. The convergence of the results with respect to the Krylov space dimension is demonstrated in the Appendix 7.0.2). After orthogonalization of the Krylov space basis by using the Gram-Schmidt algorithm, the time-evolution restricted to this subspace was determined numerically exactly based on full diagonalization of the complex Hamiltonian matrix with CAP using the Eigen

library [56].

2.3 Comparison of TDCIS and exact treatment

In this section, TDCIS is benchmarked against the solution of the TDSE. For this, the ionization probability, as defined in Eq. 2.19, was obtained at $T/2$, i.e., after the exposure of the system to a half cycle of the laser field, from both the solution of the TDSE as well as from the TDCIS wave function. These calculations were performed for confining potentials with a width parameter w in the range of 1 to 5. The result of these calculations is shown in Fig. 2.2. There, one can observe that the TDCIS approach reproduces very accurately the ionization probability obtained from the solution of the TDSE for $w < 2.5$. Hence, the TDCIS approach appears to be particularly suitable to describe the ionization dynamics of rather strongly confined systems. For more weakly confined systems, i.e., for $w > 2.5$, however, substantial deviations between the two approaches are observable. In fact, for the parameters considered, deviations up to 40 percent (i.e., for $w = 5$) are apparent. In order to understand the origin of these substantial deviations between the two approaches, it proved to be expedient to find an approximation to the exact TDSE wave function that has the so-called open-shell form [47]:

$$\Psi(x_1, x_2, t) \approx \phi_u(x_1, t)\phi_v(x_2, t) + \phi_v(x_1, t)\phi_u(x_2, t). \tag{2.50}$$

This (approximate) wave function describes one electron occupying a spatial orbital ϕ_u while the other electron populates a different orbital ϕ_v, which is not necessarily orthogonal or parallel to ϕ_u.

Note that the TDCIS wave function can be exactly represented in this form (see Eq. 2.51):

$$\Psi(x_1, x_2, t)_{TDCIS} = \psi_u(x_1, t)\psi_v(x_2, t) + \psi_v(x_1, t)\psi_u(x_2, t) \tag{2.51}$$

where:

$$\psi_u(t) = \psi_0 \tag{2.52}$$

and

$$\psi_v(t) = \sum_i \tilde{\alpha}_i(t)\psi_i. \tag{2.53}$$

Thus, such an approximation of the TDSE wave function (as long as it is reasonable) allows a transparent comparison of the wave functions obtained from both approaches.

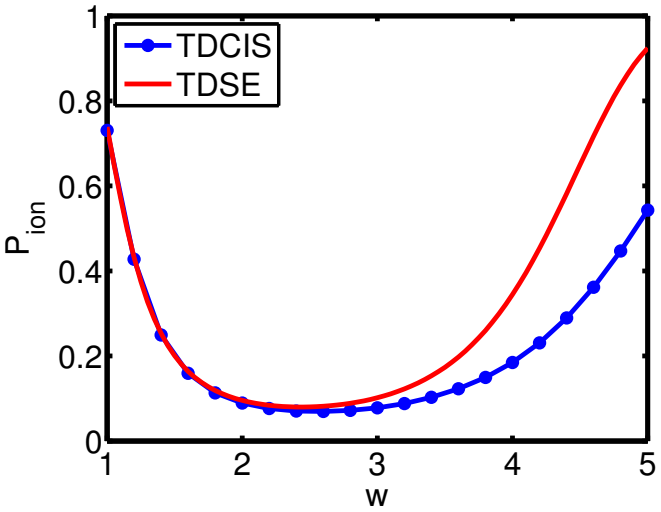

Figure 2.2: The ionization probability P_{ion} as defined in equation 2.19 after a half cycle of the laser field obtained by the solution of the TDSE (red curve) and by the TDCIS approach (blue curve with dots) in dependence on the width parameter w. All quantities in this figure are given in effective atomic units. For narrow confinement (i.e., for $w < 2.5$), the TDCIS approach reproduces very accurately the ionization probability obtained from the solution of the TDSE whereas for $w > 2.5$ substantial deviations are observable. This figure has been published in Ref. [20].

One way to obtain such an approximate open-shell wave function, is presented in the following. For this, the exact two-electron wave function is approximated in terms of configurations constructed from the two most occupied natural orbitals ϕ_i (see Eq. 2.54). Note that the natural orbitals, which are the eigenfunctions of the first order density matrix [57], constitute an orbital basis set that leads to the most rapidly converging expansion in configurations [58]. Due to this fact, this truncated configuration interaction expansion provides an excellent approximation of the exact wave function which involves only two (spatial) orbitals that can be populated by the electrons.

$$\Psi \approx \sum_{i,j=0}^{1} c_{ij}\phi_i(x_1)\phi_j(x_2) \Big/ \sqrt{\sum_{i,j=0}^{1} |c_{ij}|^2}. \tag{2.54}$$

In the situation considered, with good accuracy (deviations are smaller than 0.001), the coefficients

$$c_{00} = \int dx_1 dx_2 \phi_0^*(x_1)\phi_0^*(x_2)\Psi(x_1, x_2) \tag{2.55}$$

and

$$c_{11} = \int dx_1 dx_2 \phi_1^*(x_1)\phi_1^*(x_2)\Psi(x_1, x_2) \tag{2.56}$$

can be chosen real with alternating sign. Here, * denotes complex conjugation. Moreover, one should note that the coefficients c_{01} and c_{10} vanish exactly [59, 60]. Therefore, the expansion in terms of configurations constructed from the two most occupied natural orbitals can be represented in open-shell form. As described in Ref. [47], ϕ_u and ϕ_v can be chosen as:

$$\phi_u = (|c_{00}|^{\frac{1}{2}}\phi_0 + |c_{11}|^{\frac{1}{2}}\phi_1)/(4(|c_{00}|^2 + |c_{11}|^2))^{\frac{1}{4}} \tag{2.57}$$

$$\phi_v = (|c_{00}|^{\frac{1}{2}}\phi_0 - |c_{11}|^{\frac{1}{2}}\phi_1)/(4(|c_{00}|^2 + |c_{11}|^2))^{\frac{1}{4}}. \tag{2.58}$$

With this, for instance for $w = 5$, the expansion in configurations constructed from the two most occupied natural orbitals as well as the approximate wave function in open-shell form have an overlap of 0.967 with the solution of the TDSE. Hence, in this way, an excellent approximation of the solution of the TDSE in open-shell form can be obtained.

It turned out that for all situations considered, one of these two orbitals is localized in the potential well whereas the other one exhibits significant overlap with the tunneling barrier. Thus, the dominant ionization process investigated appears to be one where one electron resides in the potential well while the other tunnels through the barrier. In the following, the localized orbital will be referred to as ϕ_{loc} whereas the orbital that has significant overlap with the tunneling barrier will be termed ϕ_{tun}. Note that within the TDCIS approach, the localized orbital coincides with the Hartree-Fock ground state orbital. For consistency, it will be termed ψ_{loc} while the orbital that describes the tunneling electron will be named correspondingly ψ_{tun}.

It should be noted that these orbitals are only fixed up to a factor, i.e., a two-electron wave function in open-shell form is invariant under the transformation $\phi_{tun} \to \phi_{tun}/\alpha$, $\phi_{loc} \to \alpha\phi_{loc}$ where α is an arbitrary non-zero complex number. Therefore, to compare the two open-shell wave functions, the subsequent considerations are restricted to normalized orbitals (see Fig. 2.3).

For $w = 1$, TDCIS reproduces accurately the ionization probability obtained from the numerical solution of the TDSE. This indicates that TDCIS describes the ionization process accurately. This is also reflected in the comparison of the orbitals associated with the open-shell wave functions (see Fig. 2.3a). There, one can observe that although deviations between TDCIS and TDSE wave function are present, they predominantly concern the part of the orbitals within the confining potential well. Namely,

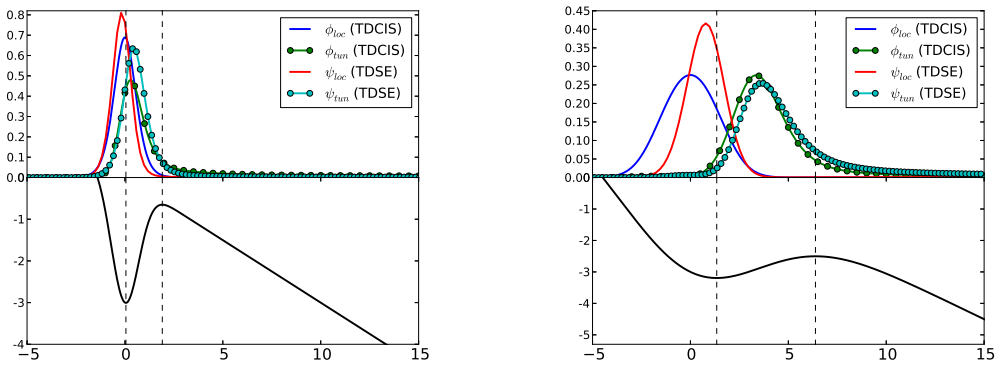

(a) $w = 1$ **(b)** $w = 5$

Figure 2.3: The normalized orbitals $\tilde{\phi}_{loc,tun} = \frac{\phi_{loc,tun}}{||\phi_{loc,tun}||}$ which constitute the (approximate) open-shell form of the exact wave function and the TDCIS wave function at $t = T/4$ for (a) $w = 1$,(b) $w = 5$. All quantities in this figure are given in effective atomic units (see the Appendix 7.0.1).

the localized orbital ϕ_{loc}(TDSE) is slightly shifted to the left with respect to the origin ($\langle x \rangle_{\phi_{loc}} = \frac{\int |\phi_{loc}|^2 x dx}{||\phi_{loc}||^2} = -0.258$) whereas within the TDCIS approach, the localized orbital (i.e. ψ_{loc}) coincides with the Hartree-Fock ground state orbital ψ_0 (see Eq. 2.52), which is centered at the origin ($\langle x \rangle_{\psi_{loc}} = \frac{\int |\psi_{loc}|^2 x dx}{||\psi_{loc}||^2} = 0$). Notably, these deviations occur predominantly for $x < 2$, i.e., within the potential well. This indicates that within the potential well, the two electrons avoid each other more effectively when they both are allowed to populate flexible orbitals. Importantly, within the tunneling barrier, i.e., in vicinity of $x \sim 2$, the density of the TDCIS orbital that describes the tunneling electron is similar to the density of the corresponding orbital obtained from the solution of the TDSE. This indicates that in this situation, TDCIS describes the ionization process reasonably.

For $w > 2.5$, however, the TDCIS approach is not able to reproduce accurately the ionization probability obtained from the solution of the TDSE. In the following, the situation is considered where $w = 5$, i.e., where the ionization probability obtained from TDCIS differs by 40 percent from that obtained from the solution of the TDSE. In this situation, significant deviations are present between the orbitals that constitute the open-shell wave functions. Namely, the localized orbital ϕ_{loc} (TDSE) is significantly shifted towards the local minimum of the instantaneous potential at $x = 1.344$,i.e.,$\langle x \rangle_{\phi_{loc}} = 0.862$, whereas within the TDCIS approach, as inherent to TDCIS, the localized orbital is still centered at the origin. Importantly, in contrast to the situation discussed before (i.e., for $w = 1$),

here, substantial deviations are also observable between the orbitals that describe the tunneling electron, i.e., ψ_{tun} (TDCIS) and ϕ_{tun} (TDSE). Importantly, deviations are present in the region where the tunneling barrier is located. Namely, the orbital ϕ_{tun} (TDSE) ($\langle x \rangle_{\phi_{tun}} = 4.829$) is shifted towards the potential barrier maximum at $x = 6.385$ with respect to ψ_{tun} (TDCIS) ($\langle x \rangle_{\psi_{tun}} = 4.203$). This indicates that the immobility of the localized electron within the TDCIS approach affects via the Coulomb interaction also the tunneling electron. That is, within the TDCIS approach, the tunneling electron seems to be less effectively pushed towards the tunneling barrier so that within the TDCIS approach, the effective tunneling barrier seen by the escaping electron appears to be larger than in the TDSE approach. This provides an explanation for the considerable deviations between the two approaches (TDSE and TDCIS) concerning the ionization probability. In particular, the underestimation of the ionization process by the TDCIS approach appears to be related to this effect (see Fig. 2.2).

2.4 Field-induced multi-electron motion

In the previous section, an approximation of the full wave function in open-shell form was considered to obtain insight into the light-induced dynamics. In this section, additional and complementary insight is provided by analysis of the full wave function. Concretely, the solution of the TDSE is analyzed with regard to collective electron motion and electron correlations.

To start with, a few general aspects concerning the light-induced dynamic are discussed. First, it should be noted that the dynamics within the confining potential well induced by the low-frequency light field considered are essentially quasi-adiabatic. This becomes apparent by the fact that for all model parameters considered, the level spacing of the confinement ΔE is much larger than the frequency of the light field - i.e. $\Delta E \geq 0.48 \gg \omega = 2\pi \times 0.001$.

Second, it is important to note that the light field couples to the center of mass of the electrons and can induce a collective electron motion. Note that the (quasi-adiabatic) motion of the electronic center of mass can be related to a shift of the confining potential minimum Δx which is given within the harmonic approximation by:

$$\Delta x = \frac{E(t) w^2}{2V_0}. \tag{2.59}$$

Note that this effect causes a shift of the density with respect to the origin (see Fig. 2.6).

This shift of the potential minimum results in the motion of both electrons which becomes noticeable in the open-shell form approximation (see equation 2.50) by the fact that the orbital ϕ_{loc}, which describes a localized electron, is not centered at the origin but is rather shifted towards the local minimum of the instantaneous potential (see Fig. 2.3). In this context, one should note that large deviations between the ionization probability obtained by TDCIS and that obtained form the solution of the TDSE occur when Δx is on the order of the Bohr radius or larger , i.e., $\Delta x \gtrsim 1 \mathrel{\widehat{=}} w \gtrsim 4.5$. This fact supports the explanation for the large deviations between the ionization probability obtained by TDCIS and the exact treatment as given in the previous section. Namely, as pointed out in the last section, within the TDCIS approach, the tunneling electron appears to be less effectively pushed towards the tunneling barrier which appears to be due to the immobility of the localized electron. This is a direct consequence of the inability of the TDCIS approach to describe a collective motion that involves both electrons.
Due to deviations of the confining potential from the harmonic potential, the light-field can also cause excitations of the relative motion [37]. Note that this can cause correlated electron dynamics. In order to quantify correlated electron dynamics induced by the light field, a (time-dependent) degree of correlation is attributed to the solution of the TDSE. In this chapter, correlations are considered that are reflected by the fact that the wave function cannot be represented as a single determinant. To quantify these kinds of correlations, the measure of correlations K as introduced in Ref. [61] is considered:

$$K = (\sum_i n_i^2)^{-1}. \tag{2.60}$$

Here, n_i denote the occupation numbers of the natural orbitals, i.e., the eigenvalues of the first order density matrix [57]. Note that K can be interpreted as an effective "number" of Slater determinants which are effectively necessary to represent the wave function (see Ref. [61]). Therefore, the absence of correlations is characterized by K equals one. Thus, electronic correlations manifest themselves by a value of K larger than one. Considering that $n_i > 0$ and $\sum_i n_i = 1$ (see Refs. [47, 57]), this can be concluded from equation 2.60. In order to determine K numerically, the occupation numbers of the natural orbitals were obtained by diagonalization of the first order density matrix (see Ref.[47]) represented on a spatial grid.
In Fig. 2.4, K is shown in dependence of the width parameter of the confining potential w for two situations, i.e., for the singlet ground state (blue, dotted curve) and for the two-electron wave function at $t = T/4$ (red curve). As can be seen in Fig. 2.4, for rather strongly confined systems ($w \approx 1$), the measure of correlations K for the singlet ground

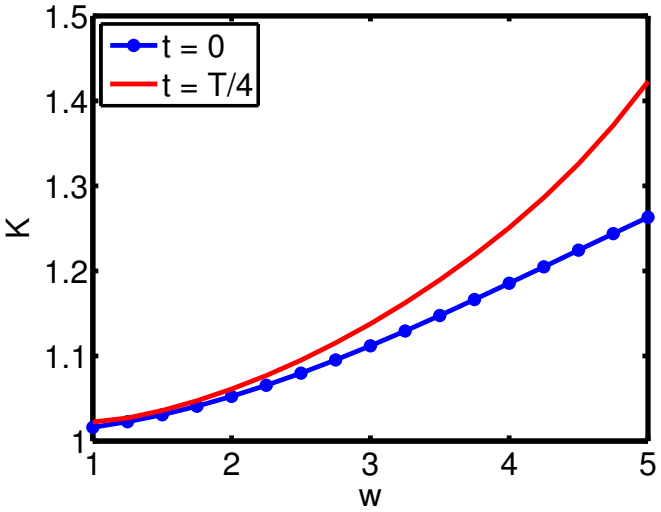

Figure 2.4: The measure of correlations K as defined in Eq. 2.60 in dependence of the width parameter w for the singlet ground state (blue curve with dots) and at the time when the electric field of the laser is strongest (t = T/4) (red curve). All quantities in this figure are given in effective atomic units (see the Appendix 7.0.1). Since the relative strength of the Coulomb interaction increases with increasing width of the confining potential, the measure of correlations present in the ground state increases correspondingly (see blue curve with dots). While for rather strongly confined systems (here, for $w \approx 1$), the measure of correlations remains constant, for more weakly confined systems, in presence of the light field, the amount of correlations is significantly increased in comparison to the ground state. This figure has been published in Ref. [20].

state is nearly one indicating an accurate description by the Hartree-Fock determinant (for $w = 1$ one finds indeed that mostly only one natural orbital is populated in the ground state with an occupation of 0.992). However, K increases monotonically with the confining potential width. This is related to a feature indicated in Eq. 2.6. Namely, the confinement energy and the Coulomb interaction scale differently with respect to the characteristic confinement length l_0. As discussed before, the relative strength of the Coulomb interaction increases monotonically with the width of the confinement potential causing an increasing prominence of Coulomb correlations that are manifested in a correspondingly increasing population of more than one natural orbital (see Fig. 2.5). For $w = 5$, one finds that in the ground state, a second natural orbital is significantly populated with an occupation of 0.107. Notably, if one considers the two-electron wave function at $t = T/4$, i.e., when the electric field of the laser is maximum, one observes a significant enhancement of correlations even with respect to the ground state correlations. For instance for $w = 5$, the occupation of the second most occupied natural

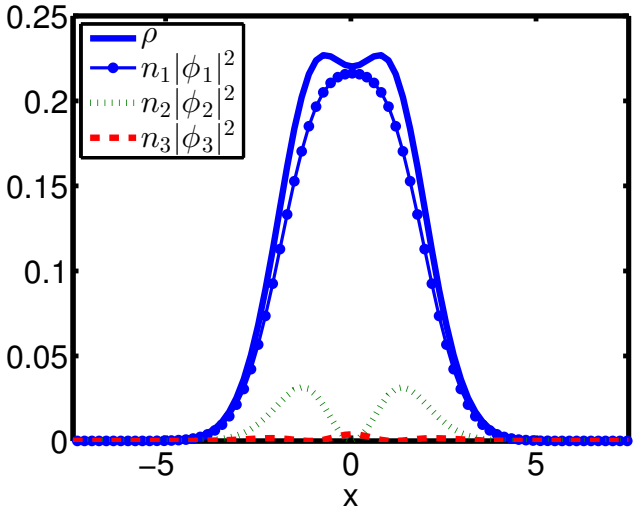

Figure 2.5: The probability density ρ of the singlet ground state and the densities of the first three most occupied natural orbitals ϕ_1, ϕ_2 and ϕ_3 weighted by their occupation numbers (n_1,n_2 and n_3) for a relatively wide confining potential (w = 5). All quantities in this figure are given in effective atomic units (see the Appendix 7.0.1). Due to a strong Coulomb interaction with respect to the confinement energy, more than one natural orbital is significantly occupied in the ground state. This figure has been published in Ref. [20].

orbital increases from 0.107 ($t = 0$) to 0.142 ($t = T/4$). Furthermore, a third natural orbital becomes noticeably populated with an occupation of ≈ 0.028 ($t = T/4$) whereas its ground state occupation is only 0.009 ($t = 0$) (see Fig. 2.6). Note that the occupation of a third natural orbital is not included in the open-shell form approximation (see Eq. 2.50) and thus represents an additional deviation between TDCIS wave function and exact wave function that adds to those discussed in the previous section. The degree of correlations at $t = T/4$ is independent of the laser frequency for frequencies smaller than $2\pi \times 0.0025$ (see Fig. 2.7) so that the enhancement of K during the exposure to the laser appears to be an adiabatic effect. The most occupied natural orbitals are localized within the well of the instantaneous potential. Hence, this light-induced enhancement of K appears to reflect a (quasi-)adiabatic rearrangement of the electrons within the confining potential well that is strongly deformed by the light-field. Here, the enhancement of K indicates an enhanced effective strength of the electron-electron interaction which appears to be the result of a light-induced broadening of the potential well. Note that according to Eq. 2.59 and respectively Eq. 2.13, an increase of the width of the confining potential is accompanied with both an increased light-induced shift of

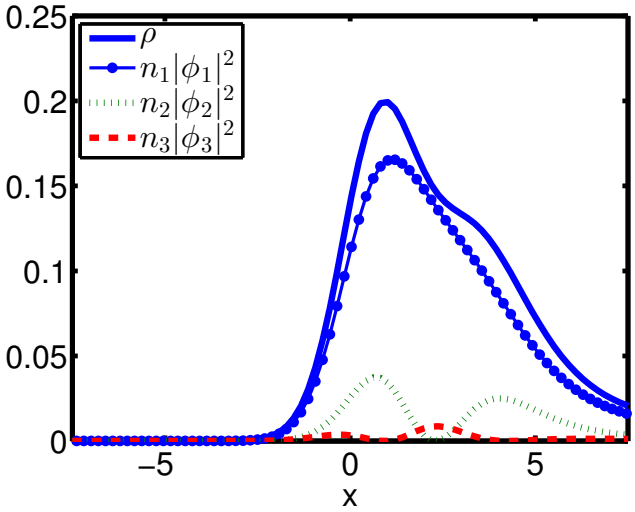

Figure 2.6: The probability density ρ of the two electron state at the time when the electric field of the laser is strongest (t = T/4) and the densities of the first three most occupied natural orbitals ϕ_1, ϕ_2 and ϕ_3 weighted by their occupation numbers for a relatively wide confining potential ($w = 5$). All quantities in this figure are given in effective atomic units. In comparison to the ground state (see Fig. 2.5), the occupation of the second and the third most occupied natural orbital is increased. This figure has been published in Ref. [20].

the potential minimum and, as indicated by a decreasing critical field strength E_{crit}, by an increased light-induced distortion of the potential well. This provides an explanation of the increasing prominence of both collective and correlated electron dynamics with increasing spatial extension of the confining potential.

2.5 Conclusions

To conclude, the strong-field tunnel ionization of a correlated two-electron quantum system was investigated with regard to multi-electron dynamics. For this, the TDCIS approach, which restricts the dynamics to a single actively participating electron, was benchmarked against the solution of the TDSE, which describes the dynamics of both electrons. The comparison of these two approaches revealed that light-induced multi-electron dynamics affect the ionization probability—i.e., the key observable associated with the process. Complementarily, the solution of the TDSE was analyzed with regard to a collective electron motion and electron correlations. With this, it was demonstrated that the multi-electron effects observed are not only due to ground state correlations but also due to a collective and correlated electron motion induced by the light field.

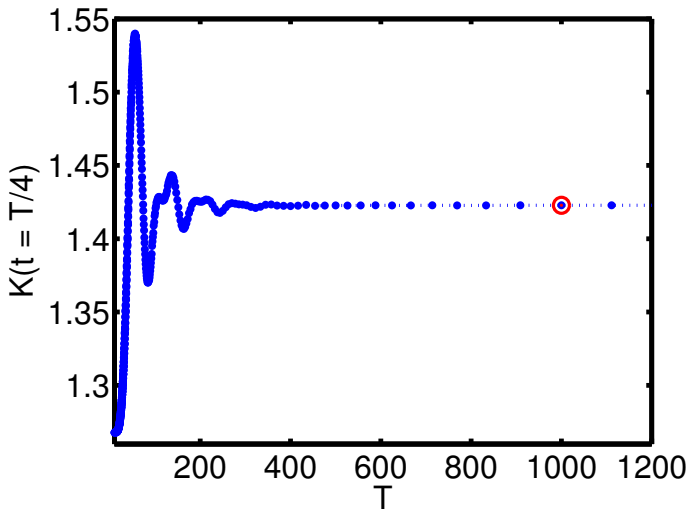

Figure 2.7: The degree of correlations K (see Eq. 2.60) at $t = T/4$ for $w = 5$ in dependence on the laser period T. All quantities in this figure are given in effective atomic units (see the Appendix 7.0.1). Note that $w = 5$ corresponds for the model parameters considered to a level spacing between the lowest one-particle bound states $\Delta E = 0.48$. Hence, $\Delta E \gg \omega = 2\pi \times \frac{1}{T}$ so that the dynamics investigated are essentially quasi-adiabatic. This can be also seen in this figure: Non-adiabatic excitations within the potential well manifest themselves by a frequency dependence of K for $T < 400$, i.e., for frequencies larger than $2\pi \times 0.0025$. Thus, for the considered laser frequency ($2\pi \times 0.001$ - see the big red marker) non-adiabatic effects are irrelevant. This figure has been published in Ref. [20].

Remarkably, this study also shows that quasi-adiabatic driving by an intense light-field can significantly enhance the correlations between the electrons while they are exposed to the field. Importantly, it was observed that these light-induced multi-electron dynamics become more important the larger the spatial extent of the system is. Hence, in general, the quasi-adiabatic multi-electron dynamics described, which have to be distinguished from non-adiabatic multi-electron effects [62], can be expected to be more prominent the larger the molecular system or nanostructure is that is exposed to a strong low-frequency field. Thus, these findings are relevant for the theoretical modeling and the understanding of strong-field ionization of a wide range of physically, chemically and biologically relevant systems.

This page is intentionally left blank.

3 Double hole migration following ionization and attosecond transient absorption spectroscopy

Parts of the results and the computational methods presented in this chapter have been published in Ref. [63].

Introduction

Charge rearrangement upon photo ionization is ubiquitous in molecular systems [1, 13, 64–69] and the observation as well as the understanding of the processes involved is one of the central goals of ultrafast science. In this context, of particular interest are correlation-driven processes representing extremely fast electronic charge transfer mechanisms that can take place even prior to the onset of a significant nuclear motion. These processes are caused by electron correlation and orbital relaxation and they have been found to give rise to complex and rich many-body electron dynamics [1, 10–13, 67, 70]. A vast number of these processes is associated with the excitation of an electron to Rydberg or to continuum orbitals thereby causing charge rearrangement. A prominent example is for instance a molecular Auger decay following inner-shell ionization where the refilling of an inner-shell vacancy is accompanied by the emission of a secondary electron; similar processes can also follow inner-valence ionization, in this situation, however, the electron is often excited to Rydberg orbitals instead of being emitted into the continuum. Either way, the emerging valence vacancies can be distributed throughout the entire molecule. As a result, even when an ionization process induces positive charge locally, correlation-driven processes can cause subsequently its delocalization throughout the entire molecular system. With currently emerging attosecond techniques [16], the observation and investigation of these processes as well as their manipulation in real-time is anticipated for the next future. Strikingly, this might pave the way towards novel pathways for controlling chemical reactions [2]. To date, however, their experimental observation in real-time is still one of the central outstanding issues of attosecond physics.

In this chapter, it is demonstrated how these kind of processes could potentially be traced in time and space by attosecond transient absorption spectroscopy (ATAS). For this purpose, the time-resolved absorption cross section is determined and it is demonstrated how observables related to correlation-driven processes are reflected in it.

This chapter is structured as follows: First, the notion of correlation-driven processes is introduced in detail. Second, the numerical approach employed for the description of the correlation-driven electron dynamics investigated is presented. On this basis, aspects concerning the real-time dynamics of correlation-driven processes are discussed by means of illustrative examples and it is demonstrated how they are reflected in the ATA spectra.

3.1 Correlation-driven charge migration

The ionization of molecules by spectrally broad light pulses can initiate coherent electron dynamics in molecular ions [3]. Concerning the nature of the dynamics triggered by such a pulse, it is important to note that for closed-shell molecules—i.e., the vast majority of stable molecules—ground state correlations typically are of minor importance. The removal of an electron from such an uncorrelated system by a light pulse will prepare—since the interaction with light is represented by an one-particle operator—a superposition of 1p1h (one-particle one-hole) configurations. These are states that result from the promotion of an electron that initially occupies a Hartree-Fock orbital in the Hartree-Fock ground state determinant to an orbital that is not occupied (i.e., a so-called virtual orbital) such as $c_i^\dagger c_a|\Phi_0\rangle$ where $c_i^\dagger$ denotes a creation operator that creates an electron in a virtual orbital and c_a denotes an annihilation operator that annihilates an electron from an orbital occupied in the Hartree-Fock ground state $|\Phi_0\rangle$. If the emitted electron is not entangled with the ion [71], the cationic state prepared is a superposition of 1h configurations, i.e., a state that results from the annihilation of an electron from the Hartree-Fock ground state determinant such as $c_a|\Phi_0\rangle$. The concrete superposition of 1h configurations prepared depends on the details of the ionization process, i.e., on the transition matrix elements to the continuum states as well as on the pulse parameters.

In the absence of electron correlation and orbital relaxation, these 1h configurations would be stationary states. In fact, those 1h configurations, which are obtained by the annihilation of an electron from an outer-valence orbital, are usually excellent approximations to exact cationic eigenstates. Hence, a preparation of one of these states would not be followed by significant charge dynamics. When after the ionization several cationic states of this kind are populated coherently, dynamics are initiated that essen-

tially involve only a single particle, i.e., a single hole. Only in the inner-valence shell, this quasi-particle picture usually breaks down, i.e., the residual electron-electron interaction, which represents the difference of the bare Coulomb interaction and the Hartree-Fock mean-field, couples those 1h configurations that are obtained by the annihilation of an electron from an inner-valence shell orbital significantly to the 2h1p configurations. These are states which result from the annihilation of an electron from a Hartree-Fock orbital from the Hartree-Fock determinant and the promotion of an electron to an orbital that is not populated in the Hartree-Fock determinant. As a consequence, inner-valence ionization can trigger correlated electron dynamics that essentially involve more than a single particle, i.e., effectively it can involve two electron holes and an electron.

3.2 Numerical approach

In the following, the numerical approach is presented which was employed for the description of correlation-driven electron dynamics discussed in this chapter. Unless stated differently, atomic units are employed.

Initial state

Ionization by broadband attosecond pulses can prepare ions in a superposition of 1h configurations whereby the actual state prepared depends in general on the pulse parameters. The considerations presented in this chapter, however, aim at aspects concerning correlation-driven charge migration which are not specific to a certain preparing attosecond pulse but which are more generally relevant. This means in particular that the ionization process itself is not considered; concretely, the dynamics following the preparation of a specific 1h configuration is investigated. Since the Schrödinger equation is a linear equation, the processes discussed still operate when this specific 1h configuration is part of a superposition of 1h configurations prepared by an actual attosecond pulse.

Valence electron dynamics - Numerical Treatment

In this work, aspects concerning purely electronic processes are discussed that predominantly occur prior to the onset of a significant nuclear motion. Therefore, in the calculations concerning these dynamics, the nuclei are kept fixed at their equilibrium positions.

The starting point for the numerical description of the valence electron dynamics in the ion is the representation of the electronic wave function of the ion in terms of a

multi-reference configuration interaction expansion:

$$|\psi(t)\rangle = \sum_i \alpha_i(t) c_i |\Phi_0\rangle + \sum_a \sum_{i<j} \alpha^a_{i,j}(t) c^\dagger_a c_i c_j |\Phi_0\rangle ... \tag{3.1}$$

where the 1h configurations $c_i|\Phi_0\rangle$ are employed as reference states. Whereas the initial state considered is an element of the subspace of 1h configurations, the non-vanishing residual electron-electron interaction can cause the promotion of electrons to virtual orbitals. As indicated in Eq. 3.1, these kind of correlation-driven processes can be considered by systematically taking into account higher excitations classes such as the 2h1p configurations configurations $c^\dagger_a c_j c_k |\Phi_0\rangle$, the 3h2p configurations and so on (indicated in Eq. 3.1 by ...) until one ends up with a fully correlated description of the electron dynamics (full-CI).

The subsequent considerations are restricted to effects that are associated with the promotion of a single electron to the virtual (Hartree-Fock) orbitals. That means, the multi-reference expansion Eq. 3.1 is truncated after the 2h1p configurations so that the time-dependent electronic wave function of the ion is expanded in terms of the 1h configurations and the 2h1p configurations.

$$|\psi(t)\rangle \approx \sum_i \alpha_i(t) c_i |\Phi_0\rangle + \sum_a \sum_{i<j} \alpha^a_{i,j}(t) c^\dagger_a c_i c_j |\Phi_0\rangle. \tag{3.2}$$

Note that for low ionization energies, processes that involve the promotion of a single electron to initially unoccupied orbitals are most prominent. The coupling of the 1h configurations to the higher configuration classes (such as the 2h1p configurations, the 3h2p configurations etc) becomes essential when the 1h configurations and higher order configurations (in particular the 2h1p configurations and the 3h2p configurations which can be directly coupled by the residual electron-electron interaction to 1h configurations) are close in energy, i.e., when they are associated with similar expectation values of the ionic Hamiltonian. Usually, when considering 1h configurations with increasing energy expectation value, first 2h1p configurations become energetically close to 1h configurations reflecting the fact that the promotion of an electron from an initially occupied orbital to the virtual orbitals requires a finite energy which is in closed-shell molecules, as those considered in this work, typically on the order of a few eV.

In order to obtain approximations to the exact wave function in the form of the wave function given in Eq. 3.2, the initial state was propagated within the subspace spanned by the 1h configurations and the 2h1p configurations, i.e., the time-evolved state was

determined by:

$$|\psi(t)\rangle = e^{-iHt}|\psi(t=0)\rangle \tag{3.3}$$

where H denotes the Hamiltonian matrix restricted to the subspace spanned by the 1h configurations and the 2h1p configurations. When the initial state is represented in terms of the eigenvectors $|I\rangle$ of H as denoted in Eq. 3.4

$$|\psi(t=0)\rangle = \sum_I \alpha_I |I\rangle, \tag{3.4}$$

the time-evolved state can be obtained by:

$$|\psi(t)\rangle = \sum_I \alpha_I e^{-iE_I t}|I\rangle. \tag{3.5}$$

Here, the coefficients α_I are the expansion coefficients of the initial state expanded in cationic eigenstates $|I\rangle$ and E_I are the corresponding energies. In the situations considered, the subspace dimension is at maximum 20000 so that cationic eigenstates can be obtained by full diagonalization of the Hamiltonian matrix using LAPACK [72]. The Hartree-Fock orbitals, the one-particle integrals of the kinetic energy and, the effective core potentials, which are needed for the calculation of the many-body Hamiltonian matrix elements, were taken from the quantum chemistry software MOLCAS [73]; the Coulomb matrix elements were obtained from the LIBINT library [74]. The molecular geometries were determined by MOLCAS on the Hartree-Fock self-consistent field (SCF) wave function level. Details concerning the orbital basis sets employed are given in Appendix 8.0.3. In the following section, the numerical approach is presented which was employed to determine the time-resolved absorption cross section from time-dependent wave functions that were obtained from the multi-reference configuration interaction singles approach presented in this section.

Time-resolved attosecond transient absorption cross section

Among those techniques that have been proposed for monitoring ultrafast electron dynamics [75–80], attosecond transient absorption spectroscopy (ATAS) [17, 81–83] stands out since it combines high spectral and high temporal resolution. ATAS is based on the transmission of a spectrally broadband attosecond probe pulse with central photon energies suitable for the excitation of an electron from an inner shell to the valence shell. After the transmission through the sample under investigation, the pulse is spectrally dispersed and analyzed. This allows one to monitor the valence electron dynamics with

both high temporal and high spectral resolution. So far, it has already been successfully applied to the electron dynamics in atoms [17, 81, 84–87] as well as to the dynamics in solid state systems [88, 89]. When applied to molecules, strong atomic localization of the inner shell orbitals and element specific inner-shell orbital energies make atomic resolution possible [80, 90]. The theoretical ATA spectra presented in this work were obtained by following the procedure given in Ref. [91] in the short-pulse approximation (i.e., the probe pulse is assumed to be a delta pulse). Assuming unaligned molecules, the orientation-averaged absorption cross section is determined.

According to Ref. [91], for molecules that are oriented, the attosecond transient absorption cross section can be obtained in the short-pulse approximation and by using Beer's law, which represents a good approximation as long as the pulse duration is smaller than the relevant dynamical timescales associated with the populated ionic eigenstates, by:

$$\begin{aligned}\sigma_Z(\omega,t) = \frac{4\pi\omega}{c}\mathrm{Im}\sum_{I,I'}\alpha_I^* e^{iE_I t}\alpha_{I'}e^{-iE_{I'}t} \\ \times\sum_F \langle I|\hat{Z}|F\rangle\langle F|\hat{Z}|I'\rangle \\ \times\Big(\frac{1}{\tilde{E}_F - E_I - \omega} + \frac{1}{\tilde{E}_F^* - E_I' + \omega}\Big)\end{aligned} \tag{3.6}$$

where $\hat{Z}$ is the component of the electric dipole operator along the laser polarization; $|I\rangle$ denote the cationic eigenstates that are populated in the cationic wave packet from which the ATA spectrum is obtained, α_I are the expansion coefficients and E_I are the corresponding energies. $|F\rangle$ denote the final states that can be reached by the absorption of a photon from the probe pulse. To account for a finite life time of inner-shell vacancies, the energies are allowed to be complex. $\tilde{E}_F^*$ denotes here the complex conjugate of the final state energy $\tilde{E}_F$.

In the situation where the molecules are completely unaligned (in this work, all considerations are restricted to this situation), the cross section can be obtained by averaging

over all possible orientations with respect to the laser polarization:

$$\begin{aligned}\sigma(\omega,t) = \frac{\omega}{c}\mathrm{Im}\int_0^{\pi}\int_0^{2\pi} d\phi d\theta \sin(\theta) \\ \sum_{I,I'} \alpha_I^* e^{iE_I t}\alpha_{I'} e^{-iE_{I'}t} \\ \times \sum_F \langle I|\hat{e}_r(\theta,\phi)\vec{R}|F\rangle\langle F|\hat{e}_r(\theta,\phi)\vec{R}|I'\rangle \\ \times\Big(\frac{1}{\tilde{E}_F - E_I - \omega} + \frac{1}{\tilde{E}_F^* - E_I' + \omega}\Big) \\ = \frac{\sigma_X(\omega,t)+\sigma_Y(\omega,t)+\sigma_Z(\omega,t)}{3}\end{aligned} \tag{3.7}$$

Here, $\hat{e}_r(\theta,\phi)$ is the radial unit vector and $\vec{R}$ is the electric dipol operator. $\sigma_X, \sigma_Y, \sigma_Z$ are the cross sections, according to Eq. 3.6, obtained for three orthogonal polarization directions and a spatially fixed molecule.

The considerations in this work concerning ATAS are focused on those features in the ATA spectra which arise due to the promotion of inner-shell electrons to vacant molecular orbitals that are populated in the Hartree-Fock determinant, i.e., those features that arise due to the presence of electron holes. These features reflect electron dynamics most prominently, i.e., in particular, more prominently than those that are associated with the promotion of inner-shell electrons to virtual orbitals (see Ref. [80, 90] and see also Fig. 3.1). This is due to the fact that the virtual orbitals are typically more delocalized than molecular orbitals that are populated in the Hartree-Fock ground state so that dipole matrix elements that mediate the transition of strongly localized inner-shell electrons to these rather delocalized virtual orbitals are smaller than those to more localized molecular orbitals that are occupied in the Hartree-Fock determinant. In this context, it is important to note that transitions involving initially occupied molecular orbitals are, for the molecules considered, spectrally well separated from those that involve virtual orbitals. This allows one to differentiate between them (see Fig. 3.1). Here, spectral regions are considered where features appear in the absorption cross section that are due to the presence of electron holes. To include the final states relevant in these spectral regions, the subspaces are constructed as described in the previous section including configurations in which one hole is in an inner-shell orbital. It should be noted, however, that in general and not considered in this work, information concerning the electron in the virtual orbitals could potentially be obtained by considering the features associated

with transitions that involve the promotion of an inner-shell electron to the virtual orbitals.

The inner-shell vacancies that are relevant for the subsequent considerations (i.e., iodine-4d, bromine-3d and bromine-3p vacancies) decay within a few femtoseconds (see for instance Ref. [92, 93]). For this reason, a finite life time $\frac{1}{\Gamma}$ is assigned to the final states which enters Eq. 3.6 in form of complex final state energies $\tilde{E}_F = E_F - \frac{i\Gamma}{2}$. In the situations considered, the decay width of the inner-shell vacancies is assumed to be on the order of the atomic ones, i.e., $\Gamma \sim 100$ meV. For the discussion in this work, this appears to be reasonable whereas for a direct comparison with experimental data accurate values might be employed.

To reduce the computational cost, the sum over the final states $|F\rangle$ in Eq. 3.6 was restricted to those states that are actually relevant in the spectral region considered, i.e., those states $|F\rangle$ for which the condition $\omega_{min} < |\tilde{E}_F - E_I| < \omega_{max}$ (ω_{min} and ω_{max} denote the minimum photon energy and the maximum photon energy, respectively) is fulfilled for all populated cationic eigenstates $|I\rangle$. Furthermore, final states $|F\rangle$ for which the transition weights $P_{I\rightarrow F}$ for all populated cationic eigenstates $|I\rangle$ fall below 10^{-8}(in atomic units) are found to be irrelavant for the features considered and therefore, they were not included in the calculations performed to obtain the spectra presented.

$$P_{I\rightarrow F} = |\alpha_I|^2(|\langle I|\hat{X}|F\rangle|^2 + |\langle I|\hat{Y}|F\rangle|^2 + |\langle I|\hat{Z}|F\rangle|^2) \tag{3.8}$$

Here, $\hat{X}$,$\hat{Y}$ and $\hat{Z}$ denote three orthogonal components of the dipole operator.

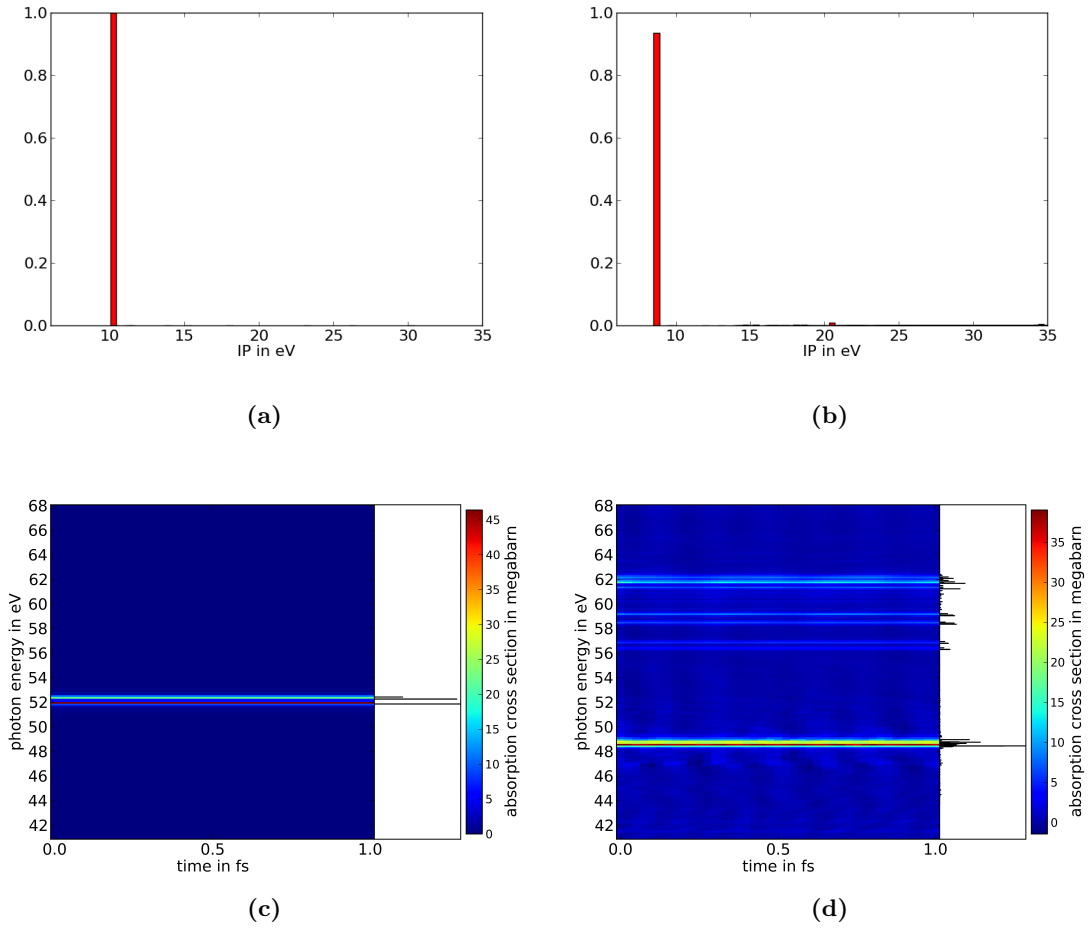

Figure 3.1: The spectral decomposition of the HOMO (highest occupied molecular orbital) 1h configuration of CH_2BrI (a) and b)) and the time-resolved absorption cross section (c) and d)) for the situation when the HOMO 1h configuration is prepared at $t = 0$. Black bars at the right side of each panel in c) and d) reflect the weight of the transitions (see Eq. 3.8) involved. In a) and c) only the 1h subspace is employed for the calculation. In this case, the HOMO 1h configuration is an eigenvector of the respective Hamiltonian matrix. Since the 2h1p configurations are excluded, transitions induced by the probe pulse to the virtual orbitals are not taken into account. As a result, only a single time-independent feature is observable. b) and d) The space spanned by the 1h and the 2h1p configurations is employed for the calculation. The HOMO 1h configuration only slightly couples to the 2h1p configurations so that it can be still well represented by a single eigenstate. As a result, the ATA spectrum is still dominated by a single essentially time-independent feature at photon energies on the order of 48 eV. A few new lines at photon energies on the order of 56 eV or larger arise which can be attributed to transitions involving the promotion of an inner-shell electron to the virtual orbitals. Note, these lines are well separated by approximately 8 eV from the feature related to the presence of the hole in the HOMO. Moreover, they are significantly less intense.

Two-hole density matrix

Focusing on the features in the absorption cross section which are due to the presence of electron holes, the correlation-driven charge migration discussed in this chapter is characterized in terms of the dynamics of the electron holes and a spectating electron that populates virtual orbitals. This characterization is particularly suitably since it allows one to directly relate observables obtained from this characterization to features in the absorption cross section.

In general, the electron in the virtual orbitals can be entangled with the electrons that reside in initially occupied Hartree-Fock orbitals. Therefore, their state has to be described by a density matrix. This reduced density matrix ρ^{2h} can be obtained from the full, time-dependent wave function $|\psi(t)\rangle$ by tracing over the virtual orbitals in the following way:

$$\rho^{2h}_{ij,kl} = \sum_m \langle \Phi^m_{i,j} | \psi(t) \rangle \langle \psi(t) | \Phi^m_{k,l} \rangle \tag{3.9}$$

$$|\Phi^a_{i,j}\rangle = c^\dagger_a c_i c_j |\Phi_0\rangle. \tag{3.10}$$

By rewriting this expression in terms of two-hole configurations which represent those states where two electrons in Hartree-Fock orbitals are annihilated from the Hartree-Fock determinant

$$|i,j\rangle = c_i c_j |\Phi_0\rangle, \tag{3.11}$$

it becomes particularly apparent that the charge dynamics associated with the electrons that occupy orbitals that are also occupied in the Hartree-Fock determinant (i.e. those electrons that do not populate virtual orbitals) and which are described by this time-dependent density matrix, can be understood in terms of the dynamics involving two electron holes.

$$\rho^{2h}_{ij,kl} = \sum_m \langle i,j | c_m | \psi(t) \rangle \langle \psi(t) | c^\dagger_m | k,l \rangle \tag{3.12}$$

Therefore, the density matrix given in Eq. 3.9 and Eq. 3.12 will be referred to as reduced two-hole density matrix.

To describe the state of the electron in the virtual orbitals, one can define analogously the reduced particle density matrix:

$$\rho^{1p}_{m,n} = \sum_{i<j} \langle \Phi^m_{i,j} | \psi(t) \rangle \langle \psi(t) | \Phi^n_{i,j} \rangle. \tag{3.13}$$

In the following, observables are discussed which were used to characterize the charge flow associated with the correlation-driven processes investigated.

Orbital populations

Insight into the electron dynamics that are associated with correlation-driven processes can be obtained by analysis of the populations of Hartree-Fock orbitals. These orbitals are eigenvectors of the Fock operator and the associated orbital energies, i.e., the corresponding eigenvalues of the Fock operator provide an ordering. This allows one to obtain insight into trends concerning the energies (i.e., in terms of a mean-field picture) of the Hartree-Fock particles (i.e., holes as well as the electron that occupies virtual orbitals) involved in the dynamics.

For this purpose, the hole-populations p_i^h are determined from the full time-dependent wave function by:

$$p_i^h(t) = \langle \Psi(t) | c_{i,\uparrow} c_{i,\uparrow}^\dagger + c_{i,\downarrow} c_{i,\downarrow}^\dagger | \Psi(t) \rangle \quad 0 \leq i < N/2 \tag{3.14}$$

where N is the number of electrons in the neutral molecule.

Complementary insight concerning the electron in the virtual orbitals can be obtained from the populations of virtual orbitals. Note, however, these virtual orbitals and their energies are typically strongly basis set dependent [94] so that they have to be considered with caution. Their populations can be obtained from the reduced particle density matrix:

$$p_i^p(t) = \rho_{i\uparrow,i\uparrow}^{1p} + \rho_{i\downarrow,i\downarrow}^{1p} \quad i \geq N/2 \tag{3.15}$$

where $\rho_{i\uparrow,i\uparrow}^{1p}$ and $\rho_{j\uparrow,j\uparrow}^{1p}$ denote the diagonal matrix elements of the particle density matrix represented in the set of virtual Hartree-Fock spin orbitals.

Partial charge

To characterize the time-dependent charge distributions and the associated charge flow, the atoms constituting the molecules considered were attributed with a charge expectation value. In this work, this was done by so-called Löwdin partial charges [95, 96]. For this purpose, orthogonal atomic orbitals were determined by Löwdin's symmetric orthogonalization. That means, from the initial non-orthogonal molecular atom-centered Gaussian orbital basis set $\{\phi_i\}$, Löwdin orbitals were obtained by a linear transforma-

tion:

$$\phi_k^{\text{Löwdin}} = \sum_i S_{k,i}^{-\frac{1}{2}} \phi_i \tag{3.16}$$

where $S_{k,i}$ denotes the overlap matrix $S_{k,i} = \int d^3r \phi_k^* \phi_i$. These Löwdin orbitals possess the property that, in a least-square sense, they exhibit the minimum deviation from the original non-orthogonal orbital basis while being orthonormal; therefore, they are still predominantly localized at the nuclei and can be attributed to the individual atoms constituting the molecule. From these orbitals, counter operators can be defined that count the number of electrons that occupy these orthonormal atomic orbitals:

$$n_i = a_{\uparrow i}^\dagger a_{\uparrow i} + a_{\downarrow i}^\dagger a_{\downarrow i} \tag{3.17}$$

where $a_{\uparrow i}$ denotes an annihilation operator that annihilates an electron from an atomic spin orbital obtained from Löwdin's symmetric orthogonalization; $a_{\uparrow i}^\dagger$ denotes a corresponding creation operator. With this, for a given electronic state, an average atomic partial charge can be attributed to an atom A by:

$$Q_A = Z_A - \sum_i \langle n_i \rangle \tag{3.18}$$

where the sum is over all atomic Löwdin orbitals that belong to the atom A; Z_A denotes the nuclear charge of the atom A. $\langle n_i \rangle$ denotes the expectation value of the counter operator n_i in the electronic state.

In this chapter, a particular focus lies on the dynamics that occur once an electron is promoted to the virtual orbitals. To characterize the charge distribution that is associated with the spatial distribution of the two holes that are present in this situation, charge expectation values were obtained from the two-hole density matrix:

$$Q_A^{2h} = Z_A - \sum_i \text{Tr}[\rho^{2h} n_i] \tag{3.19}$$

Here, Tr denotes the trace of an operator. To distinguish the partial charge obtained from the reduced two-hole density matrix from the partial charge that is obtained from the full wave function and importantly, to distinguish it from hole charge that is associated with the population of 1h configurations, the partial charge obtained in this way will be referred to as two-hole charge. The charge obtained from the reduced particle density matrix by:

$$Q_A^p = \sum_i \text{Tr}[\rho^p n_i] \tag{3.20}$$

will be referred to as particle charge. Note that by this definition, the presence of the particle at the atom A is indicated by a positive value of Q_A^p.

Density

In order to resolve the charge flow in more detail with spatial resolution, the electron density was determined by:

$$\rho(\vec{r_0}) = \langle(\delta(\vec{r} - \vec{r_0})\rangle \tag{3.21}$$

It should be noted that the evaluation of the electron density (Eq. 3.21) has to be efficient, since for a good spatial resolution, this quantity has to be evaluated many times (the densities presented required ~ 10000 evaluations per plot). In order to evaluate the expectation value 3.21 for an arbitrary wave function efficiently, the natural orbitals and their occupation numbers of this wave function were determined. With them, the evaluation reduces to the evaluation of the natural orbitals (see Ref. [97])

$$\langle\Psi|\delta(\vec{r} - \vec{r_0})|\Psi\rangle = \sum_i n_i |\phi_i(\vec{r_0})|^2 \tag{3.22}$$

where $\phi_i(\vec{r_0})$ denote the natural orbitals of the wave function Ψ and n_i are the corresponding occupation numbers. Note that this relation is not only true for single determinants but for general (correlated) wave functions. Note, this allows one to evaluate the density efficiently since the evaluation of orbitals $\phi_i(\vec{r_0})$, i.e., one-particle wave functions, is computationally unproblematic.

To visualize the spatial distribution of the two holes, the difference between the Hartree-Fock ground state density and the electron density obtained from the reduced two-hole density matrix is considered:

$$\rho_{2h}(\vec{r_0}) = \mathrm{Tr}[\rho^{2h}\delta(\vec{r} - \vec{r_0})] - \langle\Phi_0|\delta(\vec{r} - \vec{r_0})|\Phi_0\rangle \tag{3.23}$$

where $|\Phi_0\rangle$ denotes the Hartree-Fock ground state. Note that with this definition, the presence of holes is indicated by a negative value of $\rho_{2h}(\vec{r_0})$ in accordance with the lack electrons with respect to the Hartree-Fock ground state. In the following, this difference density will be referred to as two-hole density. To determine the expectation value $\mathrm{Tr}[\rho^{2h}\delta(\vec{r} - \vec{r_0})]$, the density matrix ρ^{2h} was diagonalized:

$$\rho_{2h} = \sum_K p_K |K\rangle\langle K|. \tag{3.24}$$

where p_K are the eigenvalues of ρ^{2h} and $|K\rangle$ are the corresponding eigenstates. With the relation given in Eq. 3.22, one finds:

$$\mathrm{Tr}[\rho^{2h}\delta(\vec{r}-\vec{r_0})] = \sum_{K,i} p_K n_i^K |\phi_i^K(\vec{r_0})|^2 \tag{3.25}$$

where n_i^K denote the occupation numbers of the natural orbitals ϕ_i^K of $|K\rangle$.

von Neumann entropy

The coupling of the electron in the virtual orbitals to the electron holes by the residual electron-electron interaction affects the hole dynamics. In particular, this coupling can induce entanglement between electron holes and the electron that populates virtual orbitals, i.e., the particle. To quantify this entanglement, the von Neumann entropy which represents an entanglement measure (see for instance Ref. [98])), is determined:

$$S(\rho^{2h}) = -\mathrm{Tr}[\rho^{2h}_{norm}\ln\rho^{2h}_{norm}] \tag{3.26}$$

where ρ^{2h}_{norm} denotes the normalized two-hole density matrix

$$\rho^{2h}_{norm} = \frac{\rho^{2h}}{\mathrm{Tr}\rho^{2h}} \tag{3.27}$$

If the state of the two electron holes is a pure state which is characterized by $\rho^{2h}_{norm} = (\rho^{2h}_{norm})^2$, the entropy vanishes. Entanglement between the holes and the particle is indicated by a non-vanishing von Neumann entropy.

3.3 Correlation-driven charge migration in CH_2BrI

In the following, aspects concerning the real-time dynamics of correlation-driven charge migration following inner-valence ionization are discussed and it is shown, how they are reflected in the ATA spectra. As a specific example, correlation-driven charge migration that follows the preparation of a bromine-4s vacancy in CH_2BrI is considered:

$$|\Phi(t=0)\rangle = \frac{c_{Br_{4s}}|\Phi_0\rangle}{||c_{Br_{4s}}|\Phi_0\rangle||}. \tag{3.28}$$

Here, $c_{Br_{4s}}$ denotes an annihilation operator that annihilates an electron from a bromine-4s spin orbital which was obtained from an unrestricted Hartree-Fock (UHF) calculation of the bromine atom using MOLCAS [73]. $|\Phi_0\rangle$ denotes the Hartree-Fock ground state

of CH_2BrI.

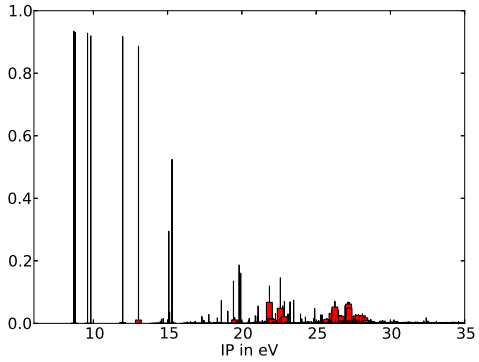

Figure 3.2: The 1h-weights (black bars) of the cationic eigenstates of CH_2BrI (see Eq. 3.29) and the spectral decomposition of the initial state considered (i.e., the bromine-4s 1h configuration; see Eq. 3.28) (red bars). IP represents the ionization energy which is here approximated by the difference of the cationic energies and the Hartree-Fock ground state energy. The bromine-4s 1h configuration strongly couples to the 2h1p configurations. This is indicated by the fact that its spectral decomposition consists of many cationic eigenstates with a low 1h-weight (≤ 0.2).

This initial state was chosen for two reasons. First, as discussed in the following, this initial atomic 1h configuration strongly couples to the 2h1p configurations so that correlation driven processes prevail the dynamics ensuing its preparation. Second, the strong (atomic) localization of the initial vacancy allows one to transparently identify valence electron migration between distinct atoms. This allows to illustrate in a transparent way how ATAS can be used to trace correlation-driven charge transfer processes in time and space. It should also be noted that due to strong atomic localization of inner-shell orbitals, similar situations actually commonly occur after inner-shell ionization so that this kind of situation is of particular importance.

In Fig. 3.2 the spectral decomposition of the initial state as well as the 1h-weight $P^{1h}[I]$ (see Eq. 3.29) of the cationic eigenstates is shown. The 1h-weight represents a quantity that quantifies the population of 1h configurations in a cationic wave function:

$$P^{1h}[\Psi] = \sum_i |\langle \Psi | c_i | \Phi_0 \rangle|^2. \tag{3.29}$$

Here, Ψ denotes a wave function whose 1h weight is determined. With this, it becomes apparent that the state $c_{Br_{4s}}|\Phi_0\rangle$ is a superposition of very many cationic eigenstates

which have a low 1h-weight (i.e., $P^{1h}[I] < 0.2$). This indicates a strong coupling of the initial atomic 1h state $c_{Br_{4s}}|\Phi_0\rangle$ to the 2h1p configurations. At $t = 0$, these contributions of the 2h1p configurations interfere destructively so that the initial state is an element of the subspace spanned by the 1h configurations. Due to different energies of the populated cationic eigenstates, the corresponding components of the prepared wave packet associated with the populated ionic eigenstates evolve differently in time; i.e., they accumulate different phases (see Eq. 3.5). This cancels the initial destructive interference of the 2h1p components of the cationic eigenstates so that at finite times, a finite 2h1p component emerges; correspondingly, an electron is promoted to the virtual orbitals.

When representing the bromine-4s orbital in terms of CH_2BrI Hartree-Fock orbitals, one finds that this expansion is governed by two orbitals, i.e., the HOMO-9 (HOMO = highest occupied molecular orbital) and the HOMO-8:

$$|\psi_{Br_{4s}}\rangle \approx 0.78 \times |\text{HOMO-9}\rangle - 0.57 \times |\text{HOMO-8}\rangle \tag{3.30}$$

Note that this is also reflected in the spectral decomposition shown in Fig. 3.2 in form of two distinct accumulations of many cationic eigenstates at ionization energies centered at $\sim$ 22 eV and at $\sim$ 27 eV, respectively, corresponding approximately (i.e., up to a few eV) to the absolute values of the associated orbital energies, i.e., 26 eV (HOMO-8) and, respectively, 30 eV (HOMO-9). This reflects the fact that according to Koopmans' theorem [99], Hartree-Fock 1h configurations are approximate ionic eigenstates and the associated ionization energies are given by the absolute value of the orbital energy of the orbital that is populated by the respective hole. However, in the situation considered, Koopmans' theorem is not a particularly good approximation which is indicated by the fact that, as indicated in Fig. 3.2, each of these two Hartree-Fock 1h configurations represents a superposition of many cationic eigenstates. As discussed in Ref. [100] for a single Hartree-Fock inner-valence 1h configuration, in such a situation, the associated population dynamics are decay-like. That means, the population of the initial 1h-configuration decreases 'quasi-exponentially' (see Ref. [100]) on a timescale that is related to the inverse of the width of the associated distribution of populated cationic eigenstates. In the particular situation considered, the widths of the two distinct distributions of cationic eigenstates are both on the order of a few eV ($\sim 1 - 2$ eV). Hence, the excitation dynamics associated with the 'quasi-decays' of the two populated Hartree-Fock 1h configurations can be expected to take place on the attosecond timescale (< 1 fs). In fact, as shown in Fig. 3.3, the excitation of the electron occurs within less than

1 femtosecond, i.e., the time-dependent 2h1p-weight $P^{2h1p}[\Psi(t)]$, which can be defined analogously to the 1h-weight (see Eq. 3.31), increases from 0 to ~ 0.9 within only a single femtosecond.

$$P^{2h1p}[\Psi] = \sum_{a,i<j} |\langle\Psi|c_a^\dagger c_i c_j|\Phi_0\rangle|^2, \tag{3.31}$$

Note that here, $P^{2h1p}[\Psi] = 1 - P^{1h}[\Psi]$ since in the numerical approach employed, the

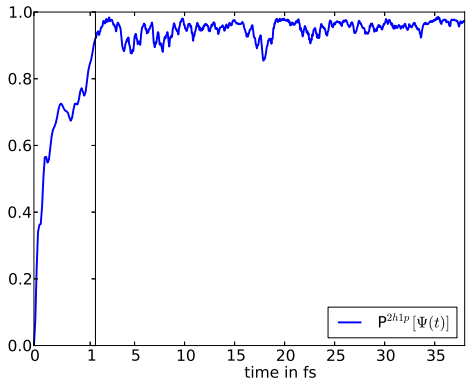

Figure 3.3: The time-dependent 2h1p-weight (see Eq. 3.31) after the prompt removal of a bromine-4s electron from the CH_2BrI molecule. Within only one femtosecond, an electron is promoted to the virtual orbitals. Note that different timescales are used in the plot to resolve the excitation dynamics during the first femtosecond after the prompt electron removal.

dynamics are (artificially) restricted to the space spanned by the 1h configurations and the 2h1p configurations. Besides small fluctuations, the 2h1p-weight remains essentially time-independent after the promotion of an electron to the virtual orbitals within the first femtosecond.

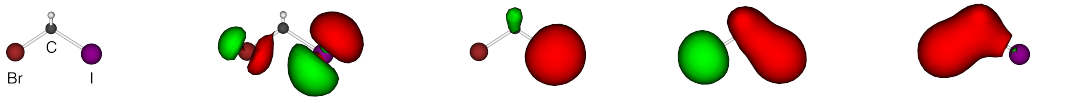

(a) CH_2BrI **(b)** HOMO **(c)** HOMO-1 **(d)** HOMO-8 **(e)** HOMO-9

Figure 3.4: The isosurfaces of Hartree-Fock orbitals that are prominently involved in the dynamics following the prompt removal of a bromine-4s electron from the CH_2BrI molecule. The isosurfaces were determined by the gv program from the MOLCAS quantum chemistry software [73].

Correlation-driven charge dynamics

In the following, the charge dynamics that follow the prompt removal of a bromine 4s electron from the CH_2BrI molecule due to correlation-driven processes are discussed. For this purpose, the charge dynamics associated solely with the 2h1p component of the time-dependent wave function are considered. The dynamics described by it are characterized in terms of a density matrix for the two holes and one for the electron that populates virtual orbitals. As observable in the two-hole density i.e., the difference of the densities obtained from the Hartree-Fock determinant and the two-hole density matrix (see Eq. 3.23), shown in Fig. 3.5, during the excitation, two-hole charge arises initially predominantly at the bromine atom and its vicinity where also the initial vacancy is located. This effect can be related to dominant intra-atomic Coulomb matrix elements (i.e., the matrix elements of the residual electron-electron interaction in an atom centered orbital basis that mediate the coupling of the initial atomic 1h configuration to the 2h1p configurations and which involve solely atomic bromine orbitals). Subsequently, however, the two-hole charge delocalizes throughout the entire molecule so that it finally reaches the iodine atom. Notably, this transfer of hole charge occurs on a significantly longer timescale ($\sim$ 15 femtoseconds) than the excitation ($\sim$ 1 femtosecond)—see Fig. 3.6.

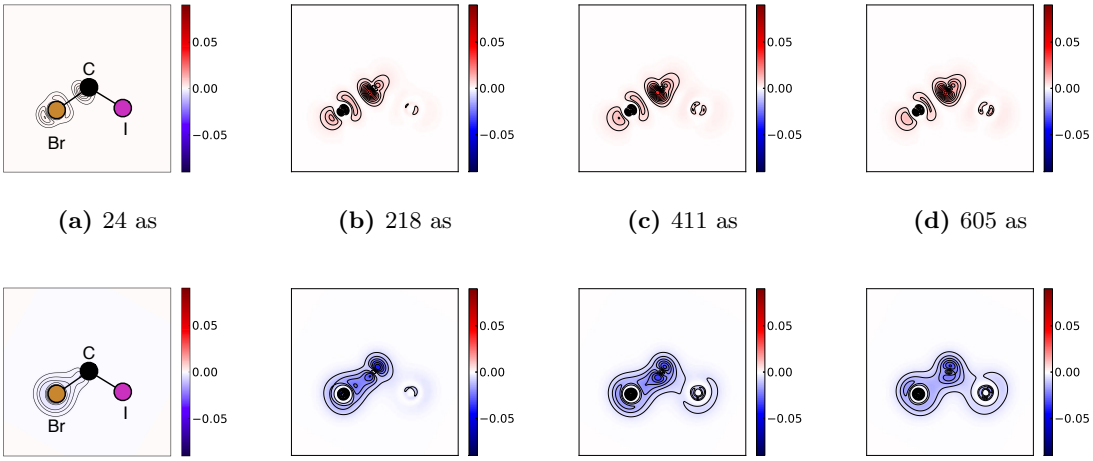

(a) 24 as **(b)** 218 as **(c)** 411 as **(d)** 605 as

(e) 24 as **(f)** 218 as **(g)** 411 as **(h)** 605 as

Figure 3.5: Upper row (a - d): the particle density following the sudden removal of a bromine-4s electron from CH_2BrI shown in the plane spanned by the bromine atom, the carbon atom and the iodine atom. Lower row (e - h): two-hole density for the same situation. Both, particle charge as well as two-hole charge arise locally at the bromine atom and its vicinity. This initial local creation is followed by a delocalization of both particle charge and two-hole charge which is essentially completed only after $\sim$ 15 fs.

The two-hole densities shown in Fig. 3.5, indicate that the transfer of two-hole charge takes place in form of a migration along the halogen-carbon bonds from the bromine atom via the carbon atom to the iodine atom. In particular, in Fig. 3.5f, one can observe that p-like orbitals of the carbon atom involved in the halogen-carbon bonds appear to mediate the transfer. As indicated in the time-resolved densities, the migration along the iodine carbon bond takes place within a few hundred attoseconds. Hence, the comparably long timescale ($\sim$ 15 femtoseconds) observed for the transfer of hole charge to the iodine atom appears to be due to a slow transfer through the carbon atom reflecting a weak coupling of these two carbon p orbitals involved in the two halogen-carbon bonds.

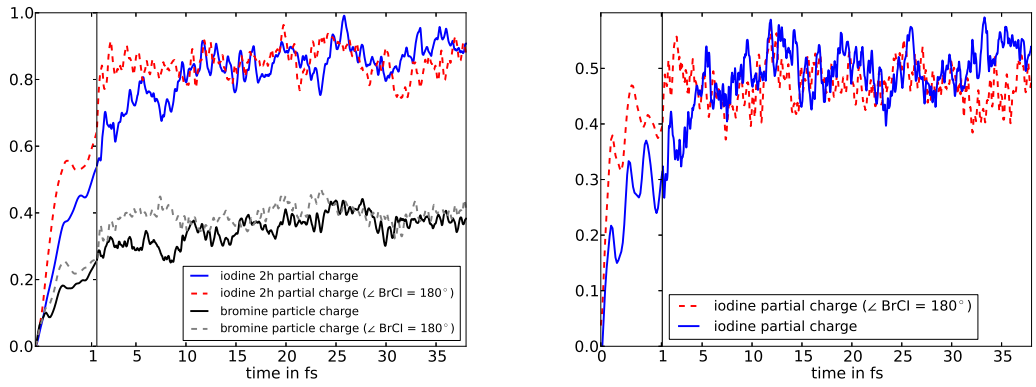

(a) **(b)**

Figure 3.6: a) The time-dependent iodine two-hole charge. The blue curve shows the time-dependent two-hole charge of the iodine atom in CH_2BrI after the sudden removal of an electron from a bromine-4s orbital. The red, dashed curve was obtained for an artificially altered molecular geometry in which the bond angle between the bromine-carbon and carbon-iodine bonds was set to 180° (see text). b) The total iodine partial charge obtained from the time-dependent wave function. Since more two-hole charge is transferred to the iodine atom than particle charge, the trends observed in the time-dependent iodine two-hole charge are also reflected in the full iodine partial charge. Note that to resolve the dynamics during the fast excitation ($\sim$ 1 femtosecond), two distinct timescales are employed.

To support this interpretation, an additional calculation was performed where the molecular geometry was (artificially) altered. Concretely, the bonding angle between bromine-carbon bond and carbon-iodine bond was set to 180° (the geometry used for this calculation is given in the Appendix 8.0.1). As indicated in the two-hole density, in this geometry, the transfer of hole charge is mediated by a single p-like orbital of the carbon atom having overlap with both the bromine-carbon bond as well as the carbon-iodine bond (see Fig. 3.7). In this situation, charge can migrate from the bromine atom through the carbon atom to the iodine atom via a single orbital and as a result, the transfer of positive charge is faster (see the red dashed curve in Fig. 3.6), i.e., in this situation, already after 2 femtoseconds as much (hole) charge is transferred to the iodine atom as for the equilibrium geometry after $\sim$ 15 femtoseconds.

It should be noted that these considerations concerning the hole-charge also apply to the dynamics of the electron in the virtual orbitals. That means, also the particle is created predominantly locally at the bromine atom and its vicinity and as for the hole charge, the carbon atom appears to be the bottleneck for the transfer of particle charge

to the iodine atom. However, the effects are not as pronounced since not as much particle charge is transferred to the iodine atom as hole charge (i.e., after 15 femtoseconds, the particle charge increased from 0 to only 0.4 whereas the increase of hole charge is on the order of 0.8). In the following section, it is demonstrated that the hole dynamics described, i.e., the initial fast refilling of the initial vacancy as well as the comparably slow transfer of two-hole charge to the iodine atom, can perfectly be traced by attosecond transient absorption spectroscopy.

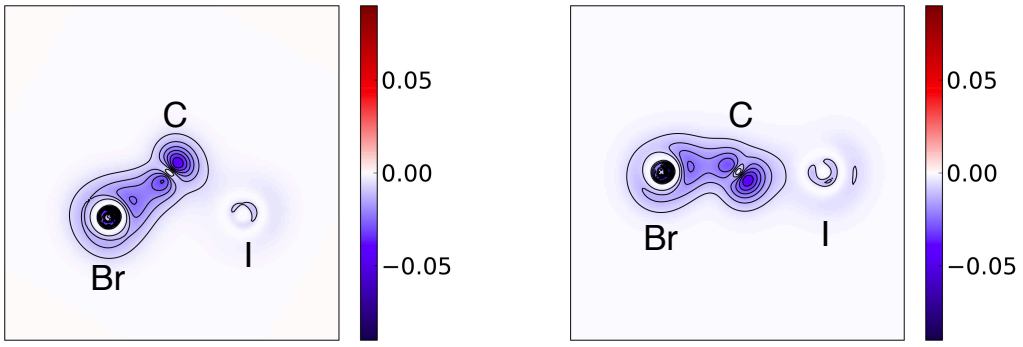

(a) **(b)**

Figure 3.7: The two-hole density at 218 attoseconds after the sudden removal of a bromine-4s electron from CH_2BrI shown in the plane spanned by the bromine atom, the carbon atom and the iodine atom. a) For CH_2BrI in its equilibrium geometry b) in the situation where the iodine-carbon carbon-bromine bonding angle is artificially set to 180°

.

Time-resolved absorption cross section

Attosecond transient absorption spectroscopy (ATAS) is based on the transmission of a spectrally broadband attosecond probe pulse with central photon energies suitable for the excitation of an electron from an inner shell to the valence shell. Strong localization of inner-shell orbitals can provide atomic spatial resolution. In the situation considered, this feature can be exploited to monitor the filling of the initial bromine-4s vacancy by considering the absorption cross section at photon energies in the range of 170 to 190 eV. There, transitions from the bromine-3p-type inner-shell to the valence shell are possible, i.e., in particular, transitions that involve the promotion of a bromine-3p electron to the HOMO-8 and the HOMO-9 which have significant overlap with the bromine 4s orbital

(see Fig. 3.8).

As a result, the cross section in this spectral region is particularly sensitive to the presence of vacancies in these two Hartree-Fock orbitals. In fact, the two features observable in the cross section at 180 eV and 185 eV, respectively, reflect the fact that the initial atomic 1h configuration is a superposition of two Hartree-Fock configurations that strongly couple to the 2h1p configurations. As the two accumulations of ionic eigenstates observable in the spectral decomposition (see Fig. 3.2) centered at ionization potentials on the order of 22 eV and 27 eV respectively, the two features in the cross section consist correspondingly of many transitions (see the right panel in Fig. 3.9a) centered at photon energies that are also separated by ~ 5 eV.

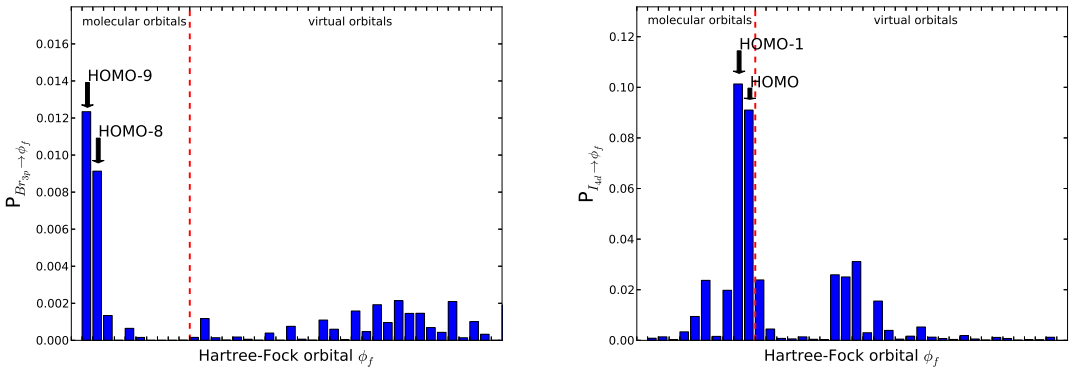

Figure 3.8: The one-particle dipole transition weights $\mathrm{P}_{\text{inner shell}\to\phi_f} = \sum_{i,f} |\langle\phi_i|x|\phi_f\rangle|^2 + |\langle\phi_i|y|\phi_f\rangle|^2 + |\langle\phi_i|z|\phi_f\rangle|^2$ associated with a) transitions from the bromine-3p type inner-shell orbitals (ϕ_i in the formula) to the valence shell orbitals ϕ_f. b) transitions from the iodine-4d type inner-shell orbitals (ϕ_i in the formula) to the valence shell orbitals ϕ_f. (Here, x,y,z denote the three components of the dipole operator). Note that the dipole transition weights are ordered by the orbital energy associated with the valence-shell Hartree-Fock orbitals ϕ_f. The red, dashed, vertical line separates those orbitals that are occupied in the Hartree-Fock determinant (left side) from the virtual orbitals (right side). The most relevant transitions involve orbitals ϕ_f that are occupied in the Hartree-Fock determinant.

Notably, when integrating the cross section from 170 to 190 eV, one obtains a quantity that it is directly proportional to the survival probability of the initial bromine-4s 1h-configuration $|\langle\Psi(t=0)|\Psi(t)\rangle|^2$ (see Fig. 3.9). This finding indicates that the integrated cross section is essentially exclusively determined by intra-atomic transitions that involve

the promotion of an electron from the atomic bromine 3p orbitals to the bromine 4s orbital.

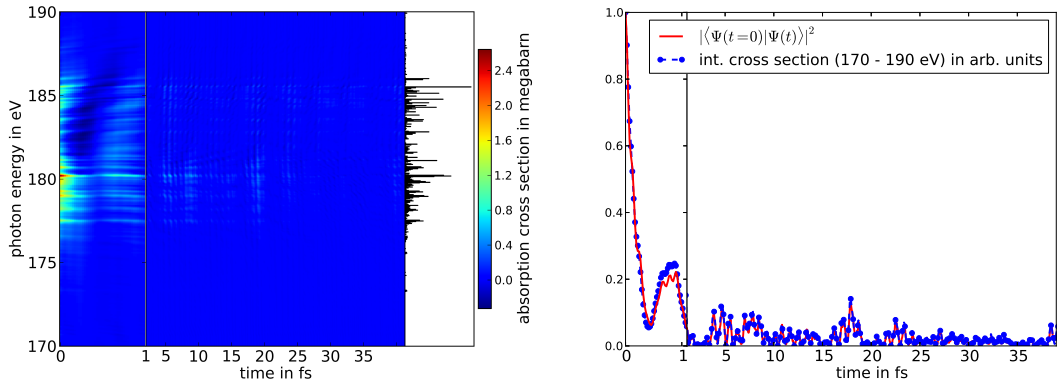

(a) **(b)**

Figure 3.9: a) The time-resolved absorption cross section for photon energies in the range of 170 - 190 eV for the situation where a bromine-4s electron is promptly removed from the CH_2BrI molecule. In this spectral region transitions from the bromine-3p inner-shell to the valence shell are relevant. Therefore the cross section in this region reflects dynamics at the bromine atom. The features at $\sim$ 180 eV and $\sim$ 185 eV reflect the repopulation of the HOMO-9 and the HOMO-8, respectively, that essentially constitute bromine-4s vacancy (see text). Black bars at the right side of each panel reflect the weight of the transitions (see Eq. 3.8) involved. b) The projection of the time-evolved state onto the initial bromine-4s 1h configuration (red curve) and the cross section integrated from 170 -190 eV (blue dots). The integrated cross section directly reflects the refilling of the bromine-4s vacancy. Note the different timescales employed to resolve the excitation dynamics that take place within the first femtosecond.

Also the transfer of two-hole charge to the iodine atom is imprinted in a feature in the absorption cross section; namely at photon energies in the range of 48 - 54 eV. There, transitions from the iodine 4d orbitals to the valence shell are possible. In particular, transitions that involve the promotion of an iodine 4d electron to an iodine 5p orbital can be induced by photons with photon energies in that range. Noting that in particular the HOMO and the HOMO-1 have large overlap with atomic iodine 5p orbitals (see Fig. 3.4), this allows to probe the transfer of two-hole charge to the iodine atom involving outer-valence orbitals. In this spectral region these transitions to the vacant p orbitals result in a complicated structure in the cross section (see Fig. 3.10) indicating rather involved electron dynamics. In this context, it should be noted that in an experiment,

this structure will expectably be subject to vibrational broadening [101]. However, the feature might still provide information concerning the absence or presence of hole charge at the iodine atom. In particular, the integration of the cross section over this feature from 48 - 54 eV yields a quantity that is directly proportional to the two-hole iodine partial charge, i.e., the iodine partial charge obtained from the two-hole density matrix, perfectly witnessing the arrival of hole charge at the iodine atom on the femtosecond timescale ($\sim 10 - 15$ femtoseconds) (see Fig. 3.10).

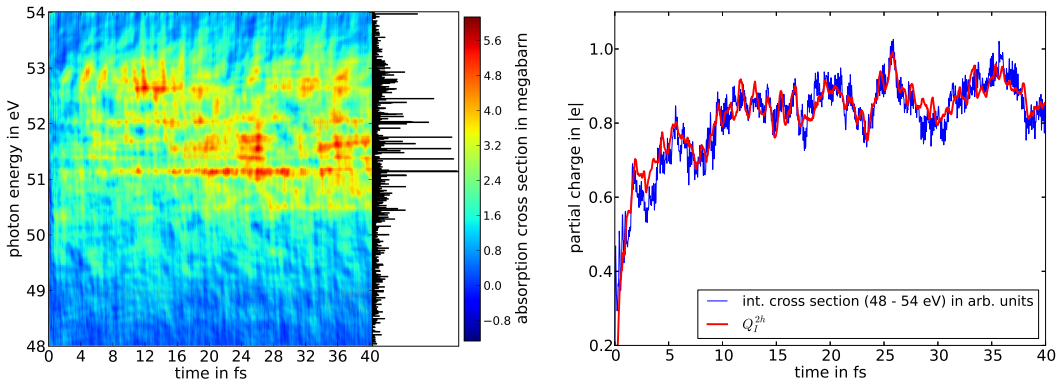

Figure 3.10: a) The time-resolved absorption cross section for 48 - 54 eV where transitions from the iodine-4p inner-shell to the valence shell are possible. The cross section in this region reflects valence electron dynamics at the iodine atom. b) The time resolved absorption cross section integrated from 48 - 54 eV and the iodine two-hole charge Q_I^{2h} (i.e., the iodine partial charge obtained from the reduced two-hole density matrix). The integrated cross section can be directly related to the iodine two-hole charge.

3.4 Coherent hole dynamics initiated by correlation-driven processes

Concluding this chapter, additional aspects concerning correlation-driven processes are discussed, which in the form presented, apparently have not yet been considered in the literature. Namely, it is pointed out that correlation-driven processes can initiate coherent hole dynamics which, in contrast to hole migration initiated by outer-valence ionization, involve two electron holes. The considerations presented in the previous section suggest that the associated potentially diverse double-hole dynamics might be evidenced experimentally by ATAS.

The nessecary condition for the existence of coherent double-hole dynamics is that the holes and the particle are not entangled with each other. In this context, it is important to note that 1h configurations couple predominantly to 2h1p configurations that are energetically close to them, i.e., 2h1p configurations that have a similar energy expectation value (as might be easily verified when considering the first order corrections with respect to residual electron-electron interaction as perturbation). Clearly, this energy constraint limits the 2h1p configurations that can essentially become populated and thereby may enforce entanglement between holes and the particle. However, this energy constraint is not strict as indicated by the finite widths of the spectral decompositions of inner-valence 1h configurations which can be on the order of a few eV (see for instance Fig. 3.2). A second potential source for entanglement is the non-vanishing residual electron-electron interaction which not only couples the 1h configurations to the 2h1p configurations but also the 2h1p configurations to each other representing a coupling of the electron holes to the particle. Therefore, it can give rise to a time-dependent degree of entanglement between particle and holes. In the following, it is demonstrated by means of an example that correlation-driven processes can at least transiently initiate significant coherent double-hole dynamics.

For this, the subsequent considerations concern correlation-driven processes ensuing inner-valence ionization in a situation where they govern the electron dynamics in the ion—i.e., a situation which is similar to that considered in the previous section. Specifically, the dynamics following the preparation of a bromine-4s vacancy in the C_6H_5Br molecule are considered. These dynamics are very similar to those described before in CH_2BrI. As for the situation discussed in the previous section concerning CH_2BrI, correlation driven processes cause the excitation of an electron to initially unoccupied orbitals within less than one femtosecond (see Fig. 3.11) and, as in CH_2BrI, the two-hole charge associated with the two holes that arise in the course of the excitation delocalizes throughout the entire molecule (see Fig. 3.12). In C_6H_5Br, however, this initial delocalization is followed by an oscillatory time-dependence of the two-hole charge distribution (see Fig. 3.12 and Fig. 3.14). That is, within the phenyl group (C_6H_5), hole charge oscillations occur with a period of $\sim$ 1.7 femtoseconds (see Fig. 3.12). On a longer timescale, after $\sim$ 2.5 femtoseconds, these charge oscillations are suppressed.

In the following, it is shown by means of a simple model that these initial charge oscillations can be interpreted in terms of coherent hole dynamics. Concretely, it is shown that they exhibit the characteristics of a single particle wave packet. To demonstrate this, a simple model system is considered consisting of a single particle whose motion is restricted to a circle with radius ρ_0. The coordinate system is chosen as shown in the

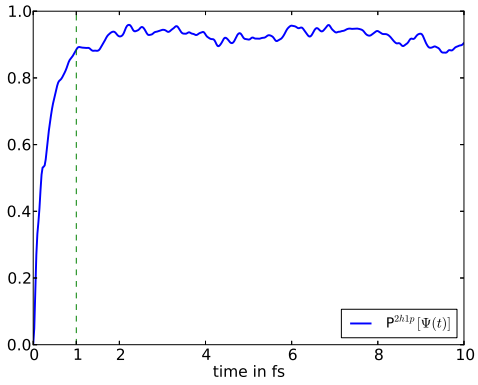

Figure 3.11: a) The time-dependent 2h1p weight after the sudden removal of a bromine-4s electron from the C_6H_5Br molecule. After the preparation of the initial bromine-4s vacancy, within less than a single femtosecond, an electron is promoted to initially unoccupied orbitals.

sketch in Fig. 3.13. Locations on the circle are attributed to the locations of the carbon atoms in the phenyl group. For instance, the location of the carbon atom (named C_0 in the sketch shown in Fig. 3.13), to which the bromine atom is attached, corresponds to $\phi = 0$ and the location of the carbon atom C_1 corresponds to $\phi = \frac{\pi}{3}$ (see Fig. 3.13). The locations of other carbon atoms are assigned analogously to locations on the circle (i.e., $C_2 \mathrel{\widehat{=}} \phi = \frac{2\pi}{3}$, $C_3 \mathrel{\widehat{=}} \phi = \pi$, etc.).

To compare the model with the *ab-initio* calculation, the density $|\Phi_{Model}(\phi, t)|^2$ obtained from the model wavefunction was integrated over specific regions on the ring. In this way, charges are defined that can be compared with partial charges obtained from the *ab-initio* calculation. For this purpose, the density of the model wave function was integrated over the intervals $[\phi_i - \frac{\pi}{6}, \phi_i + \frac{\pi}{6}]$:

$$Q^{Model}(\phi_i) = \int_{\phi_i - \frac{\pi}{6}}^{\phi_i + \frac{\pi}{6}} \rho_0 d\phi |\Psi_{Model}|^2 \tag{3.32}$$

where ϕ_i denote the angles associated with carbon atoms in the phenyl group. Here, these charges obtained from the model wave function are used to model the joint partial charges of the carbon atoms and the atom attached to them (i.e., a hydrogen atom or the bromine atom, respectively).

In order to describe the quantum mechanical motion of a particle in the ring, the

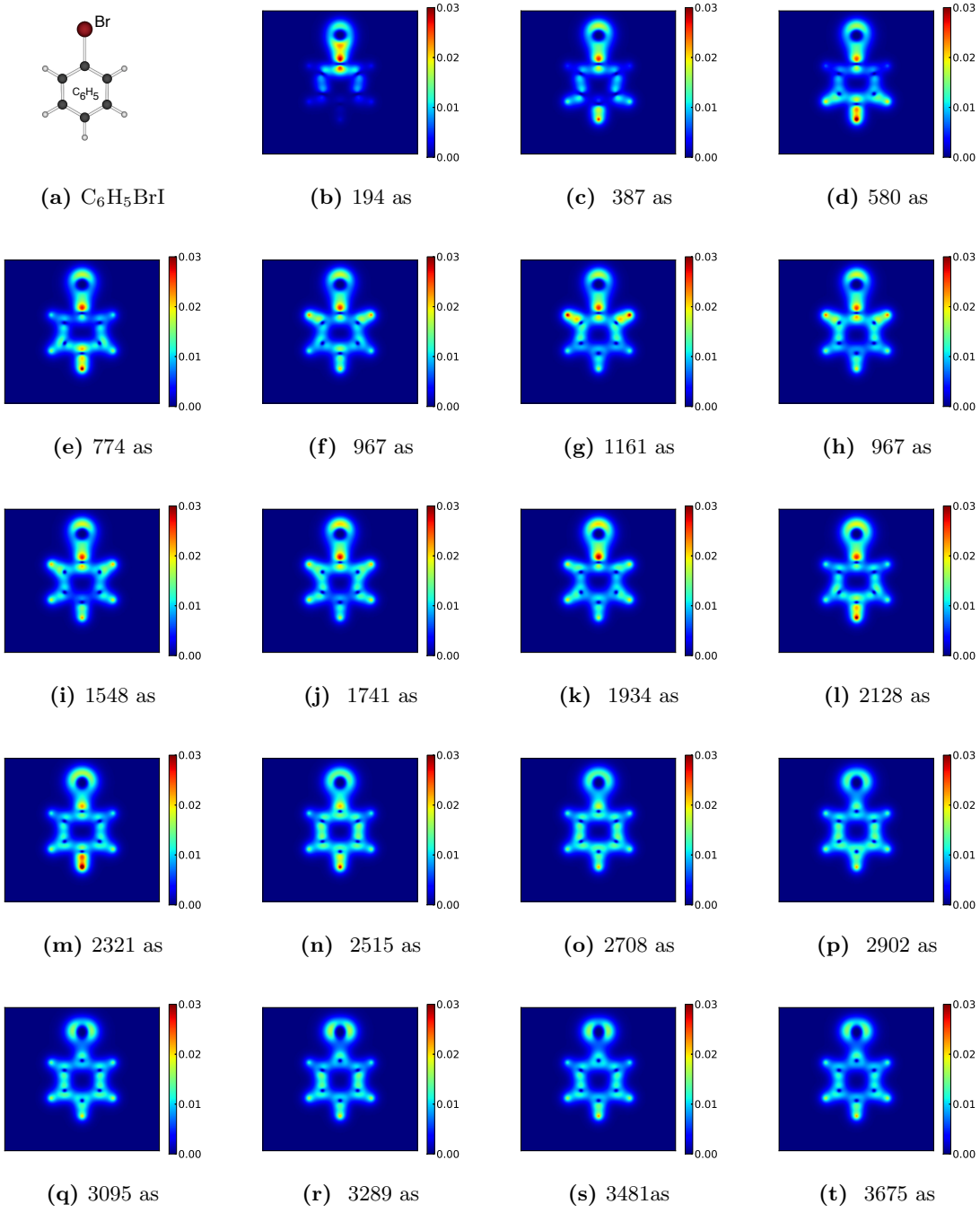

(a) C_6H_5BrI **(b)** 194 as **(c)** 387 as **(d)** 580 as

(e) 774 as **(f)** 967 as **(g)** 1161 as **(h)** 967 as

(i) 1548 as **(j)** 1741 as **(k)** 1934 as **(l)** 2128 as

(m) 2321 as **(n)** 2515 as **(o)** 2708 as **(p)** 2902 as

(q) 3095 as **(r)** 3289 as **(s)** 3481as **(t)** 3675 as

Figure 3.12: The time-dependent two-hole density of C_6H_5Br evaluated in the plane spanned by the constituting atoms after the prompt removal of a bromine-4s electron. After delocalization, the hole charge distribution exhibits charge oscillations within the phenyl group.

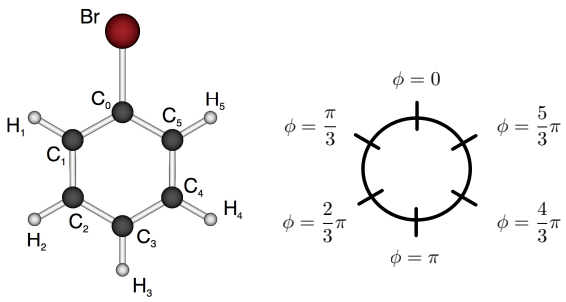

Figure 3.13: The C_6H_5Br molecule and a sketch of the coordinate system employed for the simple model of C_6H_5Br.

time-dependent Schrödinger equation has to be solved:

$$i\frac{\partial}{\partial t}\Phi_{Model}(\phi) = \frac{-1}{2\rho^2{}_0}\frac{\partial^2}{\partial\phi^2}\Phi_{Model}(\phi). \tag{3.33}$$

Here, $\Phi_{Model}(\phi)$ denotes a 2π periodic function. As a first step, one may determine the stationary states of the model Hamiltonian, which can be obtained in an analogous manner as described in many textbooks for a 'particle in a box' (see for instance Ref.[102]) but by imposing periodic boundary conditions. They are given by:

$$\xi_M(\phi) = \begin{cases} \frac{1}{\sqrt{2\pi\rho_0}} & M = 0 \\ \frac{1}{\sqrt{\pi\rho_0}}\cos(M\phi) & M \neq 0 \\ \frac{1}{\sqrt{\pi\rho_0}}\sin(M\phi) & M \neq 0 \end{cases} \tag{3.34}$$

with associated energies:

$$E_M = \frac{M^2}{2\rho_0^2}. \tag{3.35}$$

With this, a general time-dependent wave packet that describes the motion of the particle in the ring is given by:

$$\Psi_{Model}(\phi, t) = \sum_M c_M \xi_M(\phi) e^{-iE_M t} \tag{3.36}$$

The first significant hole charge accumulation occurs at $t_0 \sim 580$ attoseconds at the carbon atom C_3 and the hydrogen atom H_3 (see the sketch in Fig. 3.12) which corresponds to the region in the vicinity of $\phi = \pi$ in the model. This represents a constraint to the

model wave function given in Eq. 3.36. To fulfill this constraint, phenomenologically, the coefficients in Eq. 3.36 were chosen such that at $t = t_0 = 580$ attoseconds, the wave packet represents a Gaussian function centered at $\phi = \pi$:

$$\Phi_{Model}(\phi, t = 580\text{as}) = \frac{e^{-\frac{(\phi-\pi)^2}{2\sigma^2}}}{\pi^{\frac{1}{4}}\sqrt{\rho_0\sigma\text{Erf}[\frac{\pi}{\sigma}]}} \tag{3.37}$$

where Erf denotes the error function $\text{Erf[x]} = \frac{2}{\sqrt{\pi}}\int_0^x e^{-x^2}$. As it is indicated in the two-hole density shown in Fig. 3.12, the accumulation of two-hole charge at 580 attoseconds is essentially localized between the carbon atoms C_2 and C_4. To model this, σ was chosen to $\frac{\pi}{3}$ (i.e., equals the width of the region that is attributed in the model to a carbon atom in the phenyl group and the atom attached to it). This choice yields a wave packet that is predominantly localized in the vicinity of $\phi = \pi$ between $\phi = \frac{2\pi}{3}$ and $\phi = \frac{4\pi}{3}$. The coefficients are:

$$c_i = e^{iE_M t_0}\int_0^2 \pi\rho_0 d\phi \xi_M^*(\phi) e^{-\frac{(\phi-\pi)^2}{2\sigma^2}} \tag{3.38}$$

with this, the wave function is given by:

$$\Phi_{Model}(\phi, t) \approx c_0 + c_1\cos(\phi)e^{-i\frac{t}{2\rho_0^2}} + c_2\cos(2\phi)e^{-i\frac{2t}{\rho_0^2}} + \mathcal{O}(0.01) \tag{3.39}$$

where $c_0 = 0.77, c_1 = -0.63 \times e^{i\frac{t_0}{2\rho_0^2}}$ and $c_2 = 0.12 \times e^{i\frac{2t_0}{\rho_0^2}}$. Notably, when choosing ρ_0 to 2.4 au, which corresponds approximately to half the distance of two opposing carbon atoms in the phenyl group, this simple wave function reproduces the oscillatory charge dynamics obtained from the *ab initio* calculation. For instance, it exhibits a charge accumulation in the vicinity of $\phi = 0$ at $t = t_0$ (by construction) and at $t = \frac{2\pi}{E_1} + t_0 = 4\pi\rho_0^2 + t_0 \approx 2.3$ fs. The dynamics described by this model are also in accordance with the charge oscillations at other atoms in the phenyl group (see Fig. 3.14).In Fig. 3.14, the sum of the two-hole charge of the carbon atoms C_i and the atom attached (i.e., $Q_{C_i}^{2h} + Q_{H_i}^{2h}$ and $Q_{C_0}^{2h} + Q_{Br}^{2h}$, respectively) and the corresponding charges $Q^{Model}(\phi_i)$ obtained from the model calculation are shown. The initial charge oscillations are—despite the simplicity of the model—very well reproduced when the charges obtained from the model are scaled by 0.2 and when an offset is added to them. This suggests that correlation-driven processes launch with a probability of approximately 0.2 a single hole wave packet in the phenyl group. For times larger than 2.3 femtoseconds, the hole charge oscillations are absent. The fact that this suppression is accompanied with a significant increase of

the von Neumann entropy (see Fig. 3.16a) as well as the completion of a relaxation-like hole population dynamics (see Fig. 3.15a) within the first 3 femtoseconds suggests that the coupling to the spectating electron in the virtual orbitals causes decoherence and relaxation of the holes preventing persisting coherent hole motion.

It is important to note that although in the particular situation considered, the hole dynamics described appear to be governed by the motion of a single hole, these dynamics have to be distinguished from the motion of a single hole initiated by outer-valence ionization resulting from the coherent superposition of multiple 1h configurations. The hole charge dynamics discussed here originate from the 2h1p component of the wave function. Besides the fact that they can in general involve two holes, they can concern orbitals which are not directly affected by the ionization process. That means, orbitals can be involved in the hole dynamics from which the ionization process did not necessarily remove an electron. It should be noted that these aspects discussed not only apply to charge migration following inner-valence ionization but they might also be relevant for charge rearrangement in the course of a molecular Auger decay. For instance, situations that are very similar to those considered might be realized by prompt bromine 3p ionization. Bromine 3p-type vacancies in the molecules considered are strongly localized at the bromine atom and moreover, they decay via secondary electron emission essentially within one femtosecond via a Coster-Kronig decay [92, 103]—i.e., similar to the situation considered where within the same timespan, the initial bromine-4s vacancy is filled accompanied with the excitation of an electron to initially unoccupied orbitals. The energy uncertainty associated with the bromine 3p Coster-Kronig life time, which is on the order of 1 eV [92], makes a potential coherent population of dicationic eigenstates with a corresponding (or smaller) energy separation possible. As discussed in Chapter 5 where these considerations presented here are supplemented, this kind of coherent electron dynamics following secondary electron emission can be expected to commonly occur in polyatomic molecules. In this context, one aspect must not be overlooked. Namely, in the situation considered, the residual electron-electron interaction was found to rapidly cause entanglement between holes and the particle and giving rise to a relaxation of the holes. This appears to rapidly suppress the oscillatory coherent hole dynamics launched in the course of the promotion of an electron to the virtual orbitals. In contrast, in the context of electronic decay processes associated with secondary electron emission, an interesting situation can arise in which the secondary electron quickly leaves the vicinity of the molecule so that the coupling between it and the holes effectively vanish. In such a situation, potentially rich coherent electron (hole) dynamics in the arising dication can be initiated which is only limited by the onsetting nuclear motion.

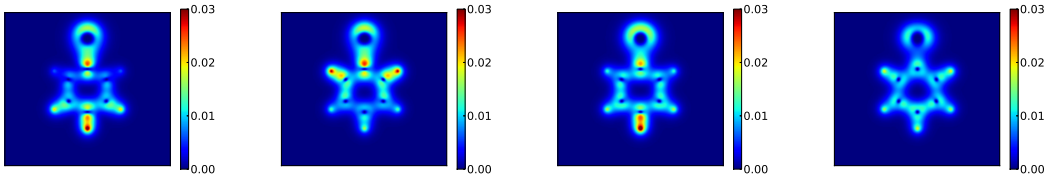

(a) 580 as **(b)** 1161 as **(c)** 2321 as **(d)** 5610 as

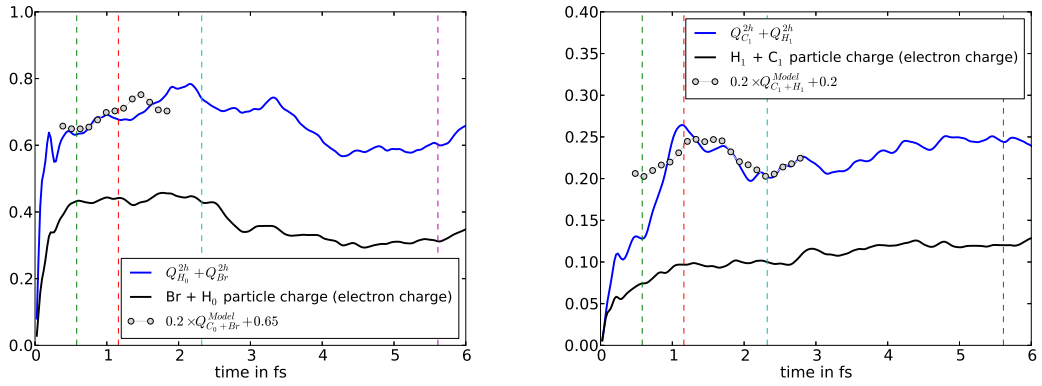

(e) **(f)**

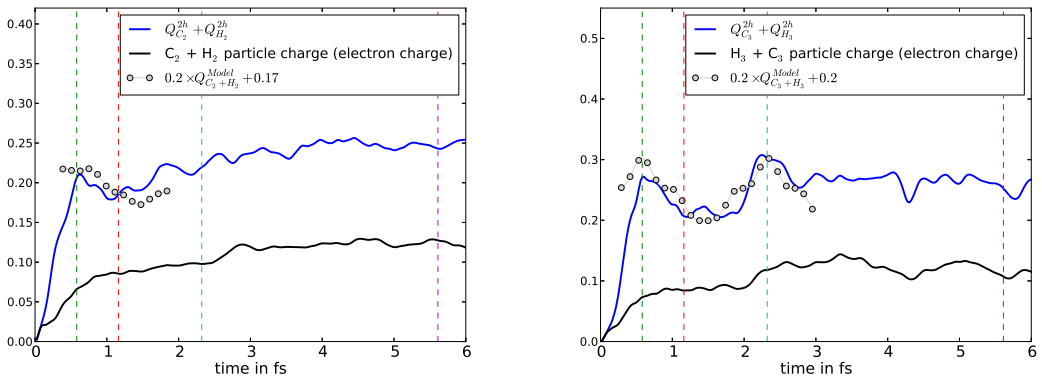

(g) **(h)**

Figure 3.14: a - d) The two-hole density after the prompt removal of a bromine-4s electron from the C_6H_5Br molecule. e - h) Time-dependent partial charges. The sum of the two-hole charges attributed to the carbon atoms and the hydrogen atoms (and respectively the bromine atom) that are attached to them. The hole dynamics that follow the initial delocalization of the two-hole charge exhibits charge oscillations (see the density in Figs. 3.14a, 3.14b, 3.14c, 3.14d—the corresponding times are indicated in the plots by dashed vertical lines) within the phenyl group. In addition, also the charges determined from the model are shown (see Eq. 3.39) (dotted curve).

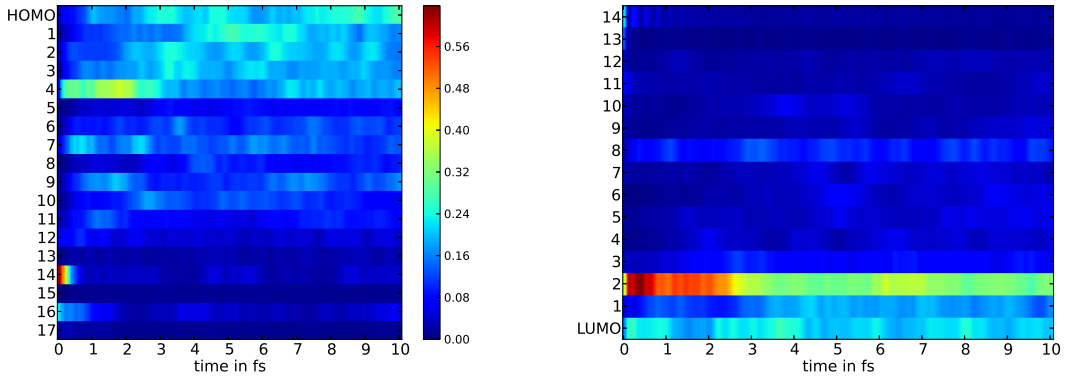

(a) **(b)**

Figure 3.15: The orbital populations of Hartree-Fock orbitals after the prompt removal of a bromine-4s electron from the C_6H_5Br molecule. a) The time-dependent hole populations. The numbers at the left refer to molecular orbitals—1 refers to HOMO-1, 2 refers to HOMO-2 and so on. The hole populations indicate a relaxation-like hole dynamics that are essentially completed after $\sim$3 femtoseconds, i.e., initially significantly depopulated inner-valence orbitals which constitute the bromine-4s orbital such as the HOMO-14 orbital are repopulated by an electron whereas outer-valence orbitals such as the HOMO, HOMO-1 and the HOMO-2 etc. become depopulated. Note that the repopulation of the inner-valence orbitals (HOMO-14) and the depopulation of the outer-valence orbitals (HOMO,HOMO-1 and HOMO-2) occur on different timescales and transiently, orbitals with intermediate orbital energies such as the HOMO-4 become depopulated. b) The time-dependent populations of the virtual orbitals. The numbers at the left refer to virtual orbitals—1 refers to LUMO+1, 2 refers to LUMO+2 and so on. Intially, predominantly, virtual orbitals with low orbital energy are populated. However, in accordance with the relaxation-like dynamics exhibited by the electron holes essentially during the first three femtoseconds, virtual orbitals with higher orbital energy become populated indicating a transfer of energy from the holes to the particle.

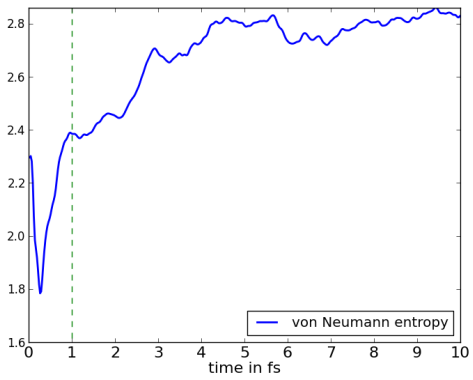

(a)

Figure 3.16: The time-dependent von Neumann entropy obtained from the normalized two-hole density matrix $\rho^{\sim 2h} = \rho^{2h}/\mathrm{Tr}\rho^{2h}$ characterizes the entanglement between holes and the electron in the virtual orbitals. The initial decrease of the von Neumann entropy during the first few hundred attoseconds is discussed in the Appendix 8.0.2. Within the following first $\sim$3 femtoseconds, however, the von Neumann entropy increases significantly indicating an increase of the entanglement between the holes and the particle due to their coupling by the residual electron-electron interaction.

3.5 Conclusions

In this chapter, it was illustrated how ATAS could be used to monitor correlation-driven charge rearrangement. When it is possible to exploit element specific core-to-valence transitions, the associated hole dynamics can be traced with atomic spatial resolution. Notably, by making use of specific intra-atomic dipole transitions, it can be possible to distinguish between the dynamics involving inner-valence from those that involve outer-valence orbitals which makes ATAS particularly suitably to trace correlation-driven processes. In this context, a characterization of correlation-driven dynamics in terms of the motion of electron holes and a spectating electron was found to be advantageous since it results in predictions that can be directly validated by ATAS. By means of this characterization, it was also pointed out that correlation-driven processes can initiate coherent hole dynamics—in contrast to outer-valence single ionization, these correlation-driven hole dynamics can involve two electron holes. Based on the considerations presented, this kind of double-hole migration in polyatomic molecules can be expected to potentially also follow electronic decay processes associated with secondary electron emission. Additional aspects concerning coherent electron dynamics following secondary electron

emission and ensuing double ionization in general are discussed in Chapter 4 and Chapter 5.

4 Correlation-driven charge migration following double ionization

This chapter is based on Ref. [63].

Introduction

Intense light-fields can induce a number of processes in molecules that can cause multiple ionization such as sequential and non-sequential multiple photo ionization as well as inner-valence or inner-shell ionization ensued by secondary electron emission. Whereas the real-time dynamics following (prompt) single ionization has been extensively investigated theoretically [1, 10–14], considerations concerning the real-time dynamics of electronic charge redistribution following multiple ionization appear still outstanding.

In this chapter, the concept of correlation-driven charge migration—as introduced in the seminal paper [1] by Cederbaum and coworkers in 1999 for single ionization—is extended to double ionization and it is demonstrated that in doubly ionized molecules, correlation-driven processes are of particular prominence. That is, by consideration of charge migration following prompt double ionization of a polyatomic molecule (C_2H_4BrI), it is demonstrated that exceptionally rich dynamics solely driven by the residual electron-electron interaction occur even in the situation when the electrons are emitted from outer-valence orbitals. This finding is relevant for the dynamics in molecules induced by light pulses that cause sequential or non-sequential double ionization, but as indicated in the considerations presented in Chapter 3, it may also concern charge rearrangement in the course of secondary electron emission following inner-valence or inner-shell ionization that can potentially initiate coherent electron dynamics in the arising dication as well. Hence, the findings presented in this chapter are relevant for a multitude of fundamental processes that are crucial for charge redistribution in molecular systems [64–66] but whose real-time dynamics remain largely unexplored—both theoretically and experimentally. To complement the considerations concerning attosecond transient absorption spectroscopy (ATAS) applied to correlated electron dynamics presented in the previous chapter, the time-resolved absorption cross section is determined for the

situations considered and the detailedness with which correlation-driven hole dynamics can be monitored by ATAS is highlighted.

Correlation-driven processes following double ionization

In this chapter, the concept of correlation-driven charge migration is extended to the charge dynamics that follow double ionization. With this, it is demonstrated that in comparison to single ionization, double ionization appears to be much more likely to initiate correlation-driven processes, i.e., processes that are solely due to the non-vanishing residual electron-electron interaction which represents the difference of the bare electron-electron interaction to the mean field potential associated with the Hartree-Fock ground state. To demonstrate this, the field-free time evolution of two-hole configurations are considered, i.e., states that result from the annihilation of two electrons from Hartree-Fock orbitals from the Hartree-Fock ground state. The electron dynamics that follow the preparation of such a state are solely due to the residual electron-electron interaction. It is important to note that since the Schrödinger equation is a linear equation, the mechanisms described are still operating when an ionization process (e.g. two-photon absorption or secondary electron emission associated with a molecular Auger decay) prepares a superposition of 2h configurations. For this reason, the conclusions drawn from the calculations presented are not exclusively valid for the initial states considered, but they apply to coherent electron dynamics following double ionization in general.

Charge migration following ionization can be triggered by short ionizing light pulses which prepare the ion in a coherent superposition of several electronic states. As discussed in the previous chapter, for outer-valence single ionization, the electronic states that can be populated, are usually well described by one-hole (1h) configurations [12, 13, 100, 104–106], i.e., states that result from the annihilation of an electron that initially occupies a Hartree-Fock orbital from the Hartree-Fock ground state. The electron dynamics that occur due to the population of several of theses states involves effectively only a single particle (i.e., a single hole). Only inner-valence single ionization typically initiates dynamics that involve more than a single particle due to significant coupling of inner-valence 1h-configurations by the residual electron-electron interaction to 2h1p configurations. The situation is fundamentally different for double ionization. Namely, in contrast to 1h configurations, the residual electron-electron interaction couples 2h configurations directly. That is, the off-diagonal Hamiltonian matrix elements of 2h configurations $\langle\Phi_0|c_i^\dagger c_j^\dagger H c_k c_l|\Phi_0\rangle$ are given by Coulomb integrals that can be identified

as the repulsive Coulomb interaction of two electron holes:

$$\langle\Phi_0|c_i^\dagger c_j^\dagger H c_k c_l|\Phi_0\rangle = V_{lkij} - V_{klij}. \tag{4.1}$$

Here, V_{ijkl} denote the Coulomb integrals:

$$V_{ijkl} = \delta_{\sigma_i\sigma_k}\delta_{\sigma_j\sigma_l} \times \int \phi_i(\vec{r_1})\phi_j(\vec{r_2})\frac{1}{|\vec{r_1}-\vec{r_2}|}\phi_k(\vec{r_1})\phi_l(\vec{r_2})d\vec{r_1}d\vec{r_2} \tag{4.2}$$

where σ denote the spin projection quantum numbers and the ϕ spatial Hartree-Fock orbitals.

Additional processes that also give rise to dynamics are based on the promotion of electrons to initially unoccupied orbitals. For low ionization energies, this is predominantly due to the coupling of the 2h configurations to the three-hole-one-particle (3h1p) configurations.

4.1 Numerical approach

To provide a transparent picture of the diverse dynamics that are driven by the residual electron-electron interaction, two kinds of calculations are performed—one concerning the dynamics that are solely driven by the hole-hole repulsion and one which includes additional particle-hole excitations. For the former, the time-dependent electronic wave function is expanded in terms of 2h configurations:

$$|\psi(t)\rangle = \sum_{i<j}\alpha_{i,j}(t)c_i c_j|\Phi_0\rangle. \tag{4.3}$$

Here, c_i, c_j denote annihilation operators of Hartree-Fock spin orbitals and $|\Phi_0\rangle$ denotes the Hartree-Fock ground state of the neutral closed-shell molecule considered. For the latter, the wave function is expanded in terms of the 2h configurations and the 3h1p configurations:

$$|\psi(t)\rangle = \sum_{i<j}\alpha_{i,j}(t)c_i c_j|\Phi_0\rangle + \sum_a\sum_{i<j<k}\alpha^a_{i,j,k}(t)c_a^+ c_i c_j c_k|\Phi_0\rangle. \tag{4.4}$$

As in Chapter 3, effective core potentials and associated basis sets from [107] (iodine), [108](carbon) and respectively [109](bromine) were employed. For the hydrogen atoms 6-31G basis sets were used. The molecular geometries are determined by MOLCAS on the Hartree-Fock SCF wave function level.

The propagation in time is performed with the exact Hamiltonian restricted to the respective configuration space. That means, analogous to the proceeding described in Chapter 3, the Hamiltonian represented in the subspace spanned by the 2h configurations and the subspace spanned by the 2h and the 3h1p configurations, respectively. The field-free time-evolution within the respective subspace is performed by diagonalization of the corresponding Hamiltonian matrix. That means, the time-evolved state in the respective approximation is obtained by:

$$|\psi(t)\rangle = \sum_I \alpha_I e^{-iE_I t}|I\rangle \tag{4.5}$$

where $|I\rangle$ denote the eigenvectors of the Hamiltonian matrix and $\alpha_I = \langle I|\psi(t=0)\rangle$ are the coefficients of the initial state represented in the eigenbasis of the respective Hamiltonian matrix. From these time-dependent wave functions, the theoretical ATA spectra were obtained analogously to the procedure described in the previous chapter. The convergence with respect to the number of virtual orbitals employed in the calculations is demonstrated in Appendix 9.

4.2 A specific example: C_2H_4BrI

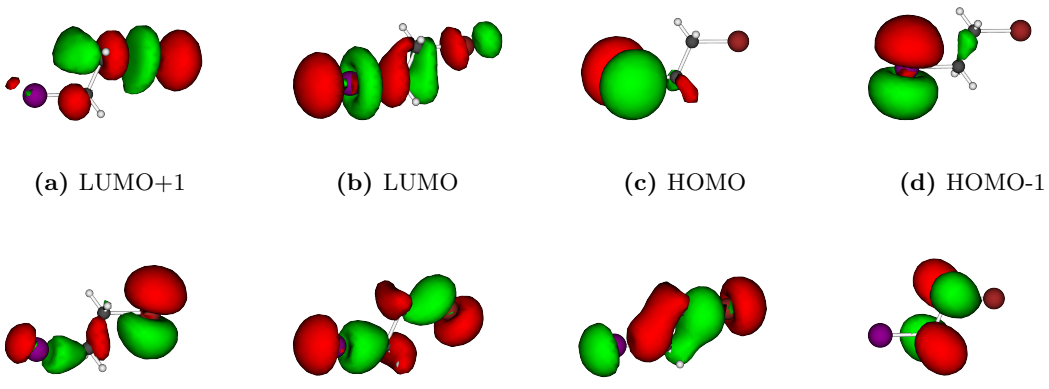

(a) LUMO+1 **(b)** LUMO **(c)** HOMO **(d)** HOMO-1

(e) HOMO-2 **(f)** HOMO-4 **(g)** HOMO-5 **(h)** HOMO-6

Figure 4.1: The isosurfaces of the molecular orbitals most prominently involved in the valence electron dynamics considered in this chapter. They were determined by the gv program from the MOLCAS quantum chemistry software [73]. This figure has been published in Ref. [63].

As a specific example, the C_2H_4BrI molecule is considered and the electron dynamics in two representative situations are discussed that can occur after double ionization. Namely, first, the situation where both electrons are emitted from outer valence orbitals and second, the situation where both electrons are removed from more strongly bound, inner-valence orbitals. For both situations, the ATA spectra are determined and the fingerprint in the spectra of the respective electron dynamics is discussed. Concerning the ATA spectra, one should note that the iodine-4d to valence transitions and the bromine-3d to valence transitions are energetically well separated. For this reason, ATAS provides for this molecule (as well as for CH_2BrI which was considered in the previous chapter) insight into the valence electron dynamics with (some) atomic spatial resolution, i.e., the dynamics that occur locally at the iodine and bromine atoms, respectively, can be resolved. In the ATA spectra presented in the following, features that occur at photon energies in the region from 46 to 67 eV involve only final states that are associated with the promotion of an electron from an iodine-4d-type orbital to the valence shell. As in Ref. [110] where a similar molecule is subject to core-to-valence spectroscopy, this spectral region is referred to as 'iodine window'. Correspondingly, the region of 67 - 80 eV is referred to as 'bromine window'; there, only transitions to final states are relevant that are associated with the promotion of an electron from the bromine-3d-type inner-shell to the valence shell.

Outer-valence ionization

First, electronic wave packets are considered that were produced via *outer-valence* double ionization. Specifically, the situation is considered where two electrons are suddenly removed from the HOMO. In the calculations artificially restricted to the two-hole configuration subspace, the resulting dynamics are governed by the coherent superposition of two dicationic eigenstates:

$$|\Psi_{2h}(t)\rangle = 0.74 \times e^{-iE_1 t}|\Psi_1\rangle + 0.57 \times e^{-iE_2 t}|\Psi_2\rangle... \tag{4.6}$$

with $E_1 - E_2 = 1.58$ eV. Both states are essentially superpositions of two spin-adapted singlet 2h configurations:

$$|\Psi_1\rangle = 0.74 \times |\mathrm{HOMO}, \mathrm{HOMO}\rangle + 0.51 \times |\mathrm{HOMO}, \mathrm{HOMO}-6\rangle... \tag{4.7}$$

$$|\Psi_2\rangle = 0.57 \times |\mathrm{HOMO}, \mathrm{HOMO}\rangle - 0.69 \times |\mathrm{HOMO}, \mathrm{HOMO}-6\rangle... \tag{4.8}$$

Hence, the dynamics are associated with oscillatory hole populations of the HOMO and the HOMO-6. Since the HOMO is primarily localized at the iodine atom whereas the HOMO-6 is mostly localized at the C_2H_4 group (see Fig. 4.1), the dynamics correspond to an oscillation of a hole between the iodine atom and the C_2H_4 group with a period of ~ 2.6 fs. This charge oscillation driven by the hole-hole interaction is reflected in the time-resolved absorption cross section in the iodine window (see Fig. 4.2a).

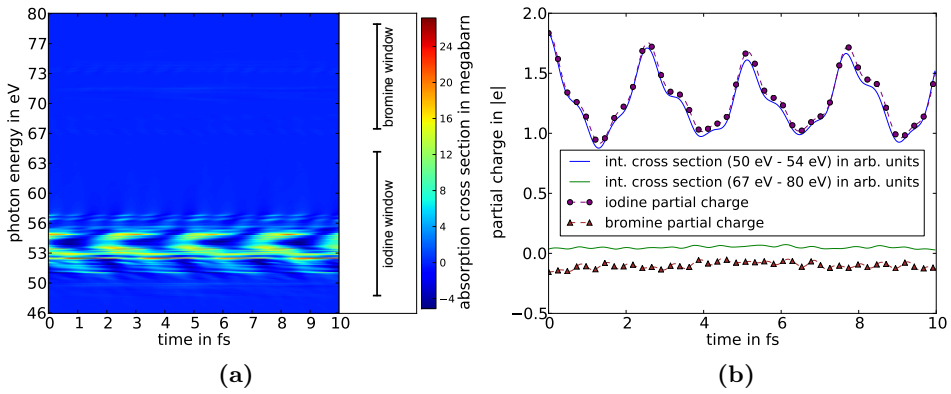

Figure 4.2: Dynamics driven by the hole-hole repulsion when two electrons are suddenly removed from the HOMO. a) the time-resolved absorption cross section b) the time-dependent partial charges obtained by Löwdin population analysis [96] in units of the elementary positive charge and the cross section integrated over selected spectral regions perfectly reflecting the charge dynamics (see text). This figure has been published in Ref. [63].

As demonstrated in the previous chapter, the dynamics associated with vacancies can be extremely well monitored by ATAS. In the approximation considered where the dynamics involve only vacancies, the integration of the cross section over the iodine window ($\sim$ 46 - 67 eV) yields a quantity that is perfectly proportional to the partial charge of the iodine atom (see Fig. 4.2b).

In the bromine window ($\sim$ 67 - 80 eV) no signal is observable. This reflects the fact that the charge dynamics are restricted to the iodine atom and the C_2H_4 group.

When including particle-hole excitations in the calculation, it becomes apparent that already in this situation, particle-hole excitations are relevant although the electrons are removed from the outer-valence shell. That is, a situation is considered where these kind of processes are usually assumed to be of minor importance [12, 13, 100, 104–106]. Here, particle-hole excitations cause prominent additional features in the time resolved absorption cross section. Besides the dominant feature at $\sim$ 53 eV which is already

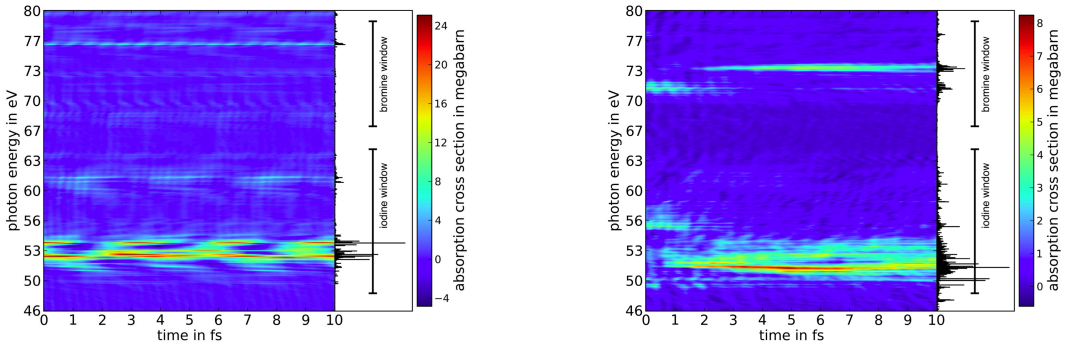

Figure 4.3: The time-resolved absorption cross section in megabarn for the situation where a) two electrons are suddenly removed from the HOMO and b) two electrons are suddenly removed from the HOMO-5. Particle-hole excitations are taken into account. Black bars at the right side of each panel reflect the weight of the transitions involved. This figure has been published in Ref. [63].

present when the calculations are restricted to the 2h subspace, at $\sim$ 61 eV and $\sim$ 77 eV new features arise (see Fig. 4.3a). The feature at 61 eV is within the iodine window ($\sim$ 46 - 67 eV) and therefore can be related to charge dynamics at the iodine atom. As the feature at $\sim$ 53 eV, it is a result of the coherent population of the two most populated states. However, in contrast to the feature at $\sim$ 53 eV where the final states involved have a significant 2h weight ($\geq$ 0.6), in the feature at $\sim$ 61 eV, final states are involved with a large 3h1p weight ($\geq$ 0.9). Actually, the feature at 61 eV can be related to charge dynamics that originate solely from the 3h1p part of the coherent population of the two most populated dicationic eigenstates and it is found to witness indirectly the excitation of an electron to initially unoccupied orbitals. Fig. 4.4b shows the time-dependent iodine difference charges

$$\Delta Q(t) = Q(t) - Q(0) \tag{4.9}$$

obtained separately from the 2h part and the 3h1p part of the coherent superposition of the two most populated dicationic eigenstates (see Fig. 4.4a). Here, Q denotes the iodine partial charge obtained by Löwdin population analysis (see Chapter 3). The charge oscillations that can be attributed in this way to the 2h part and the 3h1p part exhibit a phase shift of π as do the features at 53 eV and 61 eV. When considering the 3h1p configurations which are populated in the two eigenstates that are predominantly involved in the dynamics, one observes that in both states with comparably large weight

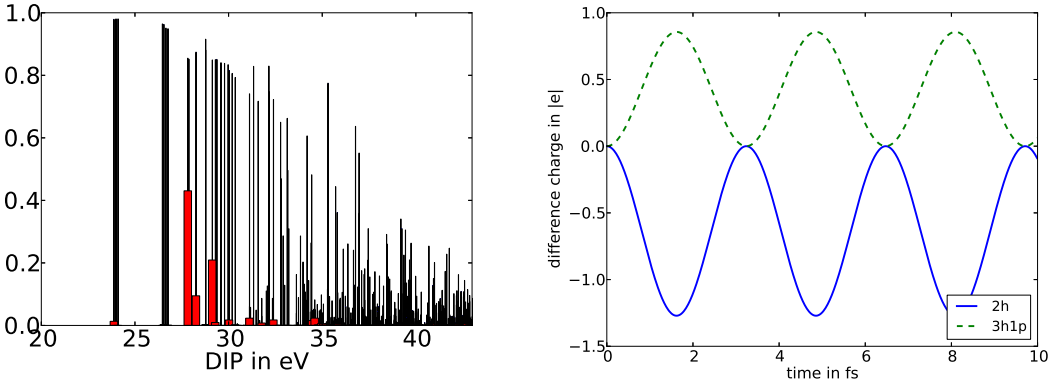

(a) **(b)**

Figure 4.4: a) The spectral decomposition (red bars) of the state prepared by removal of two electrons from the HOMO. Black bars represent the two-hole weight (which can be analogously defined to the one-hole weight (see Chapter 3)) of the dicationic singlet eigenstates. Predominantly two dicationic eigenstates are populated. Although, these two states have a dominant two-hole character (i.e., their two-hole weight is $\sim 0.8 - 0.9$), particle-hole excitations are non-negligible and cause prominent features in the ATA spectra (see Fig. 4.3). b) The time-dependent difference partial charge (see equation 4.9) obtained from the 3h1p-part and, respectively, the 2h part of coherent superposition of the two dicationic eigenstates that are predominantly populated after the sudden removal of two electrons from the HOMO (see a)). The charge oscillations that can be related to the population of 3h1p configurations are reflected in the time-resolved absorption cross section. This figure has been published in Ref. [63].

($\sim$ 0.5 of the total 3h1p weight), 3h1p configurations are populated where two holes still populate the HOMO orbital. Hence, the feature at 61 eV appears to monitor two electron holes that reside at the iodine while an electron is promoted to the virtual orbitals.

The feature in the bromine window at $\sim$ 77 eV can be related to a coherent superposition of the most populated state with a double ionization potential (DIP) of 27.7 eV and a group of dicationic states with dominant 3h1p character with 2h weight smaller than 0.1 and DIPs on the order of $\sim$ 34.5 eV. The associated energy difference of 6.7 eV is manifested in the oscillation of the cross section with a period of $\sim$ 610 as. Hence, this signal at 77 eV is caused by the charge dynamics that occur locally at the bromine atom resulting from particle-hole excitations.

Inner-valence ionization

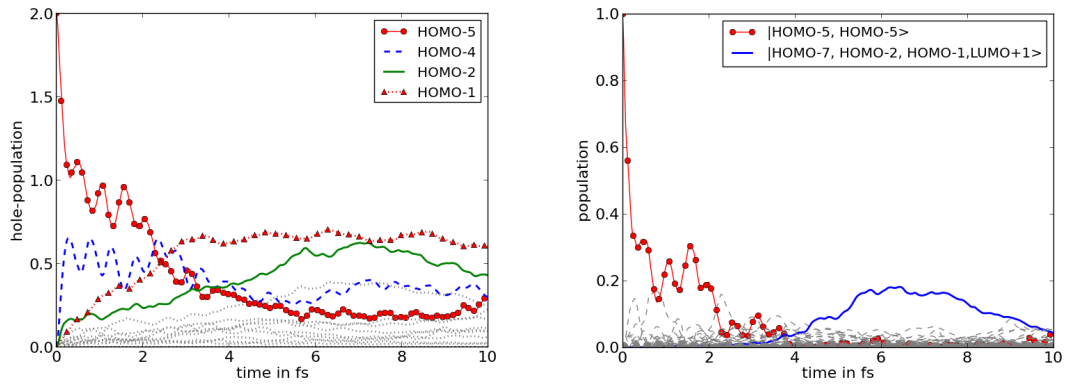

(a) **(b)**

Figure 4.5: The dynamics following the preparation of the 2h configuration that is obtained by the annihilation of two electrons that initially occupy the HOMO-5 orbital from the Hartree-Fock ground state. a) The time-dependent hole populations. b) The time-dependent populations of the 2h and the 3h1p configurations. After the depopulation of the initial two-hole configuration $|\mathrm{HOMO}-5, \mathrm{HOMO}-5\rangle$, one spin-adapted 3h1p configuration is predominantly (at least transiently) populated: $|\mathrm{HOMO}-7, \mathrm{HOMO}-2, \mathrm{HOMO}-1, \mathrm{LUMO}+1\rangle$. The depopulation of the HOMO-1 and the HOMO-2 indicates relaxation-like hole dynamics. This figure has been published in Ref. [63].

When electrons are ionized from *inner-valence* orbitals, particle-hole excitations dominate the subsequent electron dynamics in the ionic system. For single ionization, this situation has been termed 'break-down of the molecular orbital picture of ionization' [111, 112] which is characterized by the population of many ionic eigenstates with a low 1h weight. In the following, an analogous situation is considered for double ionization (see for instance Ref. [113]; see also Chapter 3) realized by a sudden removal of two electrons from the HOMO-5. The spectral decomposition of this state is shown in Fig. 4.6 where it can be observed that many dicationic eigenstates are populated that have a low 2h weight. The hole population dynamics (see Fig. 4.5 and Fig. 4.7) that follow the preparation exhibit a repopulation of the HOMO-5 by an electron, an according depopulation of the HOMO-1 and HOMO-2 on a few-fs timescale ($\sim$ 5 fs) and a very fast depopulation of the HOMO-4 within only 300 as. Note that, as in the situation considered in Chapter 3, the hole dynamics exhibit relaxation-like character (see Fig. 4.5). This indicates that, as in the situation considered in Chapter 3, the promotion of an electron to the virtual orbitals allows for an relaxation of hole charge on the iodine

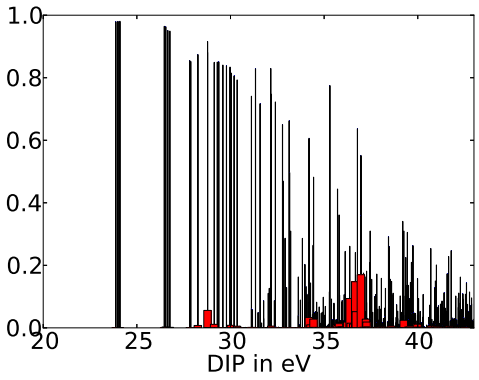

Figure 4.6: The spectral decomposition (red bars) of the state prepared by removal of two electrons from the HOMO-5. Black bars represent the two-hole weight (which can be analogously defined as the one-hole weight (see Chapter 3)). Very many dicationic eigenstates are populated that have a low two-hole weight. This figure has been published in Ref. [63].

atom and the bromine atom and thereby also cause spatial separation of the holes involved (the HOMO-1 is localized at the iodine atom whereas the HOMO-2 is localized at the bromine atom). Notably, these hole dynamics can be observed in the time-resolved absorption cross section with great detail (see Fig. 4.3b). The HOMO-5 is delocalized throughout the whole molecule (see Fig. 4.1) so that its depopulation can be observed at photon energies in both the iodine window at $\sim$ 56 eV and the bromine window at $\sim$ 72 eV. It turns out that the cross section integrated from 55 to 60 eV and from 70 to 72 eV, respectively, shows a similar trend as the hole population of the HOMO-5. However, as shown in Fig. 4.7 excellent agreement is obtained in both cases with the sum of the hole populations of the HOMO-5 and the HOMO-4 and not solely the hole population of the HOMO-5. This can be attributed to the very similar character of these two orbitals. That is, both orbitals are completely delocalized throughout the whole molecule so that both orbitals have large overlap with both the bromine and the iodine atom. In contrast, the HOMO-1 and the HOMO-2 can be distinguished since the HOMO-1 is predominantly localized at the iodine atom whereas the HOMO-2 is localized at the bromine atom. Their populations are correlated with the features in the ATA spectrum at $\sim$ 52 eV and at $\sim$ 73 eV, respectively. The very prominent population of the HOMO-1 is proportional to the absorption cross section integrated over the very prominent feature at 50 to 54 eV whereas the population of the HOMO-2 is proportional to the cross section integrated from 72 to 75 eV (see Fig. 4.7).

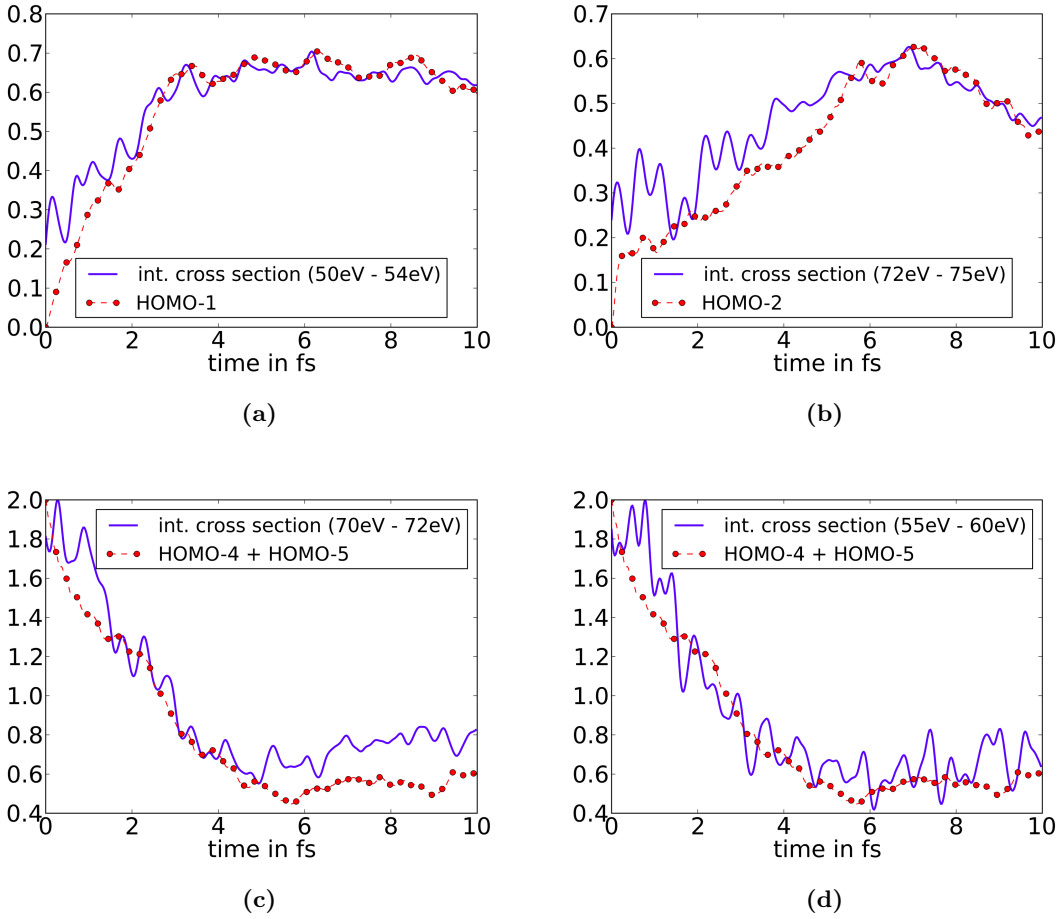

Figure 4.7: The time-resolved absorption cross section in arbitrary units (see Fig. 4.3) integrated over selected spectral regions and time-dependent hole populations for the situation where two electrons are suddenly removed from the HOMO-5. The time-dependent hole populations are reflected in the piecewise integrated absorption cross section (see text). This figure has been published in Ref. [63].

Remarkably, while the complicated substructure of the feature at $\sim$ 50 - 54 eV reflects the involvement of many dicationic eigenstates and correspondingly involved electron dynamics, the hole dynamics can simply be extracted from the ATA spectra. Notably, features associated with the emission of radiation (i.e., features where the absorption cross section is negative) known from atomic ATA spectra [91] are missing. This appears to be related to the involvement of very many transitions with only slightly different transition energies. The overlap of these many lifetime-broadened transition lines apparently causes a primarily positive cross section.

4.3 Conclusions

To conclude, it was demonstrated that in contrast to single ionization, in doubly ionized molecules, correlation-driven charge migration is particularly prominent so that rich and correlated electron dynamics are likely to follow even when electrons are emitted from outer-valence orbitals. Not only is this finding relevant for charge transfer processes following sequential or non-sequential double ionization induced by short light pulses but it also concerns charge redistribution that follows inner-shell ionization ensued by secondary electron emission. Namely, as suggested by the considerations presented in Chapter 3, a molecular Auger decay may initiate (partially) coherent electron dynamics in the dication. With the results presented in this chapter, one can expect that these electron dynamics, which follow secondary electron emission, are likely to be strongly correlated. Hence, the findings presented in this chapter are relevant for a multitude of fundamental processes whose real-time dynamics remain largely unexplored.

In addition, the time-resolved transient absorption cross section was determined for the situations discussed which allowed to complement the findings concerning ATAS presented in Chapter 3. In particular, the detailedness with which hole dynamics can potentially be monitored by using ATAS was highlighted. In this context, it was shown that features in the cross section can be directly related to observables such as hole populations providing detailed insight into the hole dynamics. Moreover, it was found that dynamics associated with the population of different excitation classes can cause distinct, spectrally well separated features in the ATA spectra allowing to differentiate between them. Compared to other more natural approaches to resolve electron dynamics with spatial resolution such as time-resolved X-ray scattering [114, 115] or electron diffraction [116], the ATA spectra allow easy and intuitive access to the electron hole dynamics with great detail. Hence, the findings concerning ATAS presented in this and the previous chapter and the fact that ATAS is already feasible [17, 117], highlight ATAS

as one of the most promising techniques for monitoring correlated electron dynamics in complex molecular systems.

This page is intentionally left blank.

5 Ultrafast charge redistribution in small iodine containing molecules

This chapter is based on Ref. [4].

Introduction

Interatomic charge redistribution in molecules accompanying secondary electron emission is a fundamental process that can follow inner-shell ionization. The resulting charge distribution triggers nuclear motion that often results in fragmentation [64–66, 118, 119] and hence, crucially determines the molecule's evolution. In contrast to the previous two chapters where the real-time dynamics of ultrafast electronic charge transfer processes were investigated, in this chapter, the focus lies on the emerging charge distributions and the nuclear motion they trigger. In particular, the theoretical considerations presented concern a recent XUV(extreme ultraviolet)-pump XUV-probe experiment [4] performed at the free electron laser FLASH in Hamburg [120, 121].

Due to strong atomic localization of inner-shell orbitals and element-specific orbital energies, XUV photoionization often induces localized vacancies. However, correlation-driven processes can cause a redistribution of the induced positive charge among the constituents of the molecule. Since the ionization potentials of inner shells are usually above the double-ionization threshold, these processes can mediate the decay of the induced inner-shell vacancy by secondary electron emission [93]. Strictly speaking, in this situation, correlation-driven processes cause both additional ionization and—with respect to isolated ions—a transfer of positive charge from the atomic site where the photoinduced vacancy is located to its molecular environment. Exposed to intense XUV radiation as provided by free electron lasers (FELs), atoms and molecules often sequentially absorb more than a single photon [64–66, 118, 119]. In this situation, interatomic charge redistribution of the light induced positive charges can be limited by atomic separation due to nuclear motion triggered by preceding ionization processes.

To date, this process has already been observed to follow inner-shell photoionization of small polyatomic molecules such as I_2,CH_3I, CH_3F, CH_3SeH and C_2H_5SeH [64–66,

118, 119]. The maximum spatial distance between two fragments, for which the process was observed, has been found to be well estimated by the so-called classical over-the-barrier model [64, 66]. Whereas these experiments mentioned focused on evidencing interatomic charge redistribution [64, 65, 118] and the investigation of the range [64, 66] the process operates in, the experiment considered in this chapter indicated a strong molecule specificity of the process. The theoretical considerations presented in this chapter suggest two mechanisms that can be responsible for this experimental result.

5.1 Experiment

The experiment [4] that is subject of the following theoretical considerations was based on the ionization of gaseous CH_2I_2 and CH_3I molecules by time-delayed femtosecond pulses with pulse lengths on the order of 100 $\pm$ 30 femtoseconds and 80 $\pm$ 30 femtoseconds, respectively. The photon energies were on the order of $\sim$ 83 eV, i.e., in the vicinity of the iodine-4d giant resonance so that predominantly electrons from the iodine-4d type inner-shell were emitted (the iodine-4d photoionization cross section at $\sim$ 83 eV is at least one order of magnitude larger than any other atomic photoionization cross section of other iodine shells or the other constituents of the molecules, i.e., the carbon atom and the hydrogen atoms [122]). With this, vacancies were created which are predominantly localized at the iodine atom(s). These iodine-4d vacancies, however, predominantly decay via electron emission [92]. The charge distributions that arise after the decay set the stage for a (potential) fragmentation dynamics. By choosing the photon density such that expectably at most two photons were absorbed after the interaction of the molecules with both pulses [4], the absorption of the second photon was effectively used to probe the stage of the fragmentation initiated by a first iodine-4d photoionization. For this, the delay of the two pulses was varied between 0 to 400 femtoseconds which allowed to influence the (average) timespan between two photo absorptions (see Fig. 5.1). If the second photon is absorbed when the fragments are in close vicinity to each other so that the induced positive charges are distributed among them, the iodine charge state distribution tends to be shifted to lower charge states with respect to a situation where the induced positive charges remain solely on a single isolated iodine fragment. In the experiment, the highest charge state found by ion-time-of-flight spectroscopy was the I^{3+} charge state—therefore, charge redistribution can only cause a decrease of the I^{3+} signal. This predestines the I^{3+} signal as indicator for interatomic charge redistribution. In Fig. 5.1, the I^{3+} signal is shown. As can be observed, it is reduced for both molecules CH_3I and CH_2I_2 for vanishing delay ($t = 0$) with respect to large delays ($t = 300$

fs). This indicates an enhanced probability for charge redistribution at $t = 0$. When

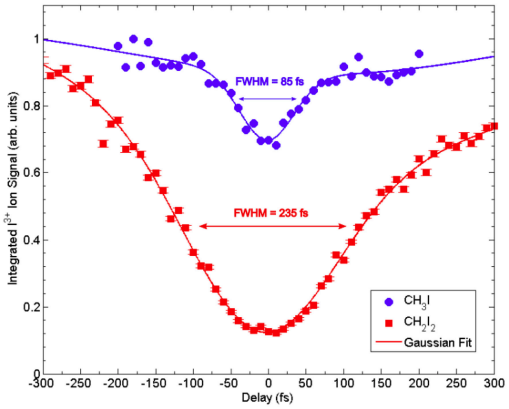

(a)

Figure 5.1: The delay-dependent I^{3+} ion yield measured in the experiment [4] normalized to its value at a delay of 400 femtoseconds. By courtesy of Karolin Mertins and Michael Martins. This figure has been published in Ref. [4].

comparing the delay-dependent I^{3+} signals, a striking difference between the two signals is observable (see Fig. 5.1). Most prominent, the reduction of the I^{3+} ion yield at $t = 0$ observed for CH_2I_2 is signifcantly larger than for CH_3I —for CH_2I_2, the I^{3+} signal decreases to less than 0.2 of its value at 400 femtoseconds, i.e., by more than 80 percent, whereas for CH_3I, the signal is reduced by only 30 percent. This finding suggests that in CH_2I_2, positive charge is more effectively transferred from the iodine atoms to their respective molecular environment than in CH_3I (For the sake of clarity: the molecular enviroment of an iodine atom in CH_2I_2 contains the other iodine atom).

5.2 Theoretical considerations

In the context of the experiment described, in this section, aspects concerning the interatomic charge redistribution following iodine-4d ionization of CH_2I_2 and CH_3I molecules are discussed.

First, the charge distributions which arise after a molecular Auger decay of iodine-4d-type vacancies in CH_2I_2 and CH_3I are investigated and second, the spatial separation of the nuclei triggered by these initial charge distributions is estimated by means of a classical Coulomb explosion model. On basis of these considerations, two mechanisms are identified that determine the amount of positive charge which is transferred from the iodine atoms to their respective molecular environment following the (sequential)

ionization by multiple XUV photons.

Charge distributions following iodine-4d inner-shell ionization

The photoinduced iodine-4d type vacancies predominantly decay via secondary electron emission within a few femtoseconds (see Ref. [92]) leaving the molecule doubly ionized. To determine the populations of the dicationic eigenstates after the molecule has undergone secondary electron emission, a two-hole population analysis was performed (see Ref. [123]). In Ref. [123], it was found that due to the dominance of intra-atomic (Coulomb) transition matrix elements (i.e., those Coulomb matrix elements that mediate an atomic Auger decay), the transition probabilities p_Ψ to dicationic eigenstates Ψ can be reasonably approximated to be proportional to the iodine two-hole populations:

$$p_\Psi \sim \sum_{i<j} | \langle \psi_{ij} | \Psi \rangle |^2 \tag{5.1}$$

Here, $|\psi_{ij}\rangle$ denotes a two-hole state $c_{\phi_i} c_{\phi_j} |\Phi_0\rangle$ where c_{ϕ_i} and c_{ϕ_j} are annihilation operators that annihilate electrons from atomic iodine spin orbitals ϕ_i and ϕ_j obtained from Löwdin's symmetric orthogonalization (see Chapter 3). $|\Phi_0\rangle$ denotes the Hartree-Fock ground state. The dicationic eigenstates were obtained from the multi-reference configuration interaction singles approach presented in the previous chapter, i.e., the dicationic eigenstates were determined by full diagonalization of the Hamiltonian represented in the space spanned by the 2h configurations and the 3h1p configurations. Note that on a similar level of theory, reasonable Auger spectra were obtained for BF_3 [123].

For the iodine atoms and the carbon atom, effective core potentials and associated valence basis sets from Ref. [124] were employed and for the hydrogen atoms 6-31G basis sets were used. The molecular geometries were obtained by MOLCAS on the Hartree-Fock SCF wavefunction level.

In order to get insight into the charge distributions associated with the populated dicationic eigenstates, the partial charges of the iodine atoms in the molecules were determined by Löwdin population analysis, i.e., for each dicationic eigenstate, the iodine partial charge was obtained as described in Chapter 3. Both, partial charges and I^{2+} two-hole populations are shown in Fig. 5.2 for ionization energies up to 60 eV. (Note, due to energy conservation essentially only dicationic states with an double ionization potential that is smaller or equal to the iodine-4d ionization potential at ~ 60 eV (estimated on the level of Koopmans' theorem) can be populated after the secondary electron emission). For this relevant part of the dicationic spectrum below ~ 60 eV, it is

clearly visible that the iodine partial charges of the dicationic eigenstates of CH_3I are shifted, compared to CH_2I_2, to higher charges. Noting that the onsetting nuclear motion expectably suppresses possible initial electronic coherences (see the disscussion in the following subsection), the charge distributions arising after the secondary electron emission may be approximated by incoherently averaging over the populated dicationic eigenstates. Choosing the weights proportional to the iodine two-hole populations, the average iodine partial charge obtained for CH_2I_2 is $\sim |e|$ for each of the two iodine atoms and $1.4|e|$ for the single iodine atom in CH_3I. Note that the induced positive charge is distributed in both molecules predominantly on the iodine atom(s)—i.e., in CH_2I_2 on the two iodine atoms and in CH_3I, respectively, the single iodine atom. For CH_2I_2, this effect is not only due to the preferable population of dicationic states with large two-hole populations but also due to the population of 3h1p configurations. That is, the average partial charges obtained are significantly smaller when the 3h1p configurations are excluded—i.e., for CH_2I_2, without the 3h1p configurations, the average partial charges would be $0.9|e|$ instead of $|e|$. This indicates that the excitation of an electron to initially unoccupied orbitals effectively enables a 'relaxation' of the positive charge on the iodine atoms which have the lowest atomic ionization potential in the molecules considered and fosters spatial separation of the induced positive charges. Notably, already in these initial charge distributions that arise prior to the fragmentation, a clear trend is visible—in CH_2I_2, less positive charge remains on each of the iodine atoms than on the single iodine atom in CH_3I.

Timescale for interatomic charge distribution

In this section, aspects concerning the real-time dynamics of the charge rearrangement in the course of decay of the photoinduced iodine-4d inner-shell vacancies via secondary electron emission are discussed which are supplemental to the considerations presented in Chapter 3. As demonstrated in Chapter 3, even in such small polyatomic molecules such as CH_2BrI, interatomic charge transfer by correlation-driven processes can take place on a different timescale than the associated excitation of an electron to initially unoccupied orbitals. In the context of a molecular Auger decay, this means that the timescale on which interatomic charge rearrangement occurs and the core hole Auger lifetime can be different. The iodine-4d inner-shell Auger life time is on the order of a few femtoseconds (see Ref. [92]). In this subsection, the second relevant timescale for charge redistribution is estimated which is related to the timescale on which postive valence charge can delocalize throughout the dication. Clearly, the timescale on

which this delocalization can take place is related to the energy differences between dicationic eigenstates that are significantly populated. As can be seen in Fig. 5.2, these relevant energy differences are in the range of sub-eV to several eV corresponding to femtosecond to attosecond timescales. However, not every coherent superposition of two of these populated dicationic eigenstates is associated with interatomic transfer of charge. Therefore, to estimate the timescale associated with the delocalization of the positive charge, dynamical calculations were performed. Considering the dominance of intra-atomic Coulomb matrix elements that mediate the decay of the iodine-4d vacancies, the time evolution of atomic iodine two-hole configurations $|\psi_{ij}\rangle$ were determined:

$$|\psi_{ij}\rangle = c_{\phi_i} c_{\phi_j} |\Phi_0\rangle \tag{5.2}$$

where c_{ϕ_i} and c_{ϕ_j} are annihilation operators that annihilate electrons from atomic iodine spin valence orbitals ϕ_i and ϕ_j obtained from Löwdin's symmetric orthogonalization. As in Chapter 4, these states were propagated with the exact Hamiltonian represented in the space spanned by the two-hole and the three-hole-one-particle configurations.

$$|\psi_{ij}(t)\rangle = e^{-iHt} |\psi_{ij}\rangle. \tag{5.3}$$

It is important to note that in general, a molecular Auger decay will not prepare the dication in such a perfectly pure state as considered here since the finite linewidth of the inner-shell vacancy enforces (some) entanglement between the Auger electron and the dication. Namely, for a fixed kinetic energy of the Auger electron, the dicationic state is essentially determined to be within a region of the dicationic spectrum whose width is essentially on the order of the linewidth. Significant coherences can therefore only occur between dicationic eigenstates whose energy separation is smaller than the linewidth. The situation considered here would correspond to an infinitely large inner-shell linewidth or correspondingly, to an infinitely short inner-shell lifetime. It is therefore important to note that the calculations presented here are used to estimate the timescale on which positive charge can delocalize—not to model the exact dicationic state prepared by secondary electron emission.

From these time-dependent calculations, time-dependent partial charges were determined. Instead of considering the time-evolution of all possible (and very many) iodine two-hole states individually, an averaged partial charge of all possible atomic two-hole configurations is considered (see Eq. 5.5 and Fig. 5.3). To account for the fact that secondary electron emission can only populate dicationic eigenstates with vacancies in

orbitals that were initially occupied in the ground state (which is here approximated by the Hartree-Fock ground state), the time-dependent two-hole states were weighted by the joint population of the two associated atomic orbitals ϕ_i and ϕ_j in the Hartree-Fock ground state $\langle\Phi_0|n_{\phi_i}n_{\phi_j}|\Phi_0\rangle$. Noting that the norm squared of the states $|\psi_{ij}\rangle$ is given by:

$$||\psi_{ij}||^2 = \langle\psi_{ij}|\psi_{ij}\rangle = \langle\Phi_0|c^\dagger_{\phi_j}c^\dagger_{\phi_i}c_{\phi_i}c_{\phi_j}|\Phi_0\rangle = \langle\Phi_0|n_{\phi_i}n_{\phi_j}|\Phi_0\rangle, \tag{5.4}$$

this can be achieved by determining the time-dependent average partial charge in the following way:

$$Q_I(t) = Z_I - \frac{\sum_{ij}\langle\psi_{ij}(t)|n_{\phi_i}|\psi_{ij}(t)\rangle}{\sum_{kl}||\psi_{kl}||^2}. \tag{5.5}$$

Here, the factor $\frac{1}{\sum_{kl}||\psi_{kl}||^2}$ ensures normalization; n_{ϕ_i} and n_{ϕ_j} denote counter operators that count the number of electrons occupying the atomic orbitals ϕ_i and ϕ_j, respectively. In Fig. 5.3, $Q_I(t)$ is shown for CH_2I_2 and CH_3I. Notably, in both molecules CH_2I_2 and CH_3I, a large amount of the initially localized positive charge is redistributed within only a few hundred attoseconds. A complete charge equalization of the iodine atoms in CH_2I_2, however, is only reached after $\sim$ 15 fs. Notably, this timescale relates to a coherent population of dicationic eigenstates that are energetically separated by an energy difference in the sub-eV regime, i.e., on the order or even smaller than typical inner-shell linewidths—for instance the iodine 4d linewidth which is on the order of $\sim$ 100 meV (see Ref. [93]). Note, this indicates that secondary electron emission that follows the preparation of an iodine-4d-type inner-shell vacancy can indeed potentially prepare the dication in a (partially) coherent superposition of dicationic states. Strikingly, the fact that this potential for coherent electron dynamics following inner-shell ionization is found for a small polyatomic molecule such as CH_2I_2 indicates that coherent electron dynamics following secondary electron emission might be a common phenomenon—particularly in larger systems with a correspondingly higher density of states, it can be expected to commonly occur. Clearly, as discussed in Chapter 3, the coupling of the dication to the Auger electron by the residual electron-electron interaction can potentially reduce these electronic coherences in the dication.

Concerning the experiment, one should note that as demonstrated in the following, significant atomic separation occurs in both CH_2I_2 and CH_3I on a longer timescale (a few tens of femtoseconds), so that the electronic charge redistribution that follows a first iodine-4d photoionization can be assumed to be essentially instantaneous with respect to significant nuclear motion. The onsetting nuclear motion expectably suppresses these possible initial electronic coherences in the dication on long timescales (a few tens of

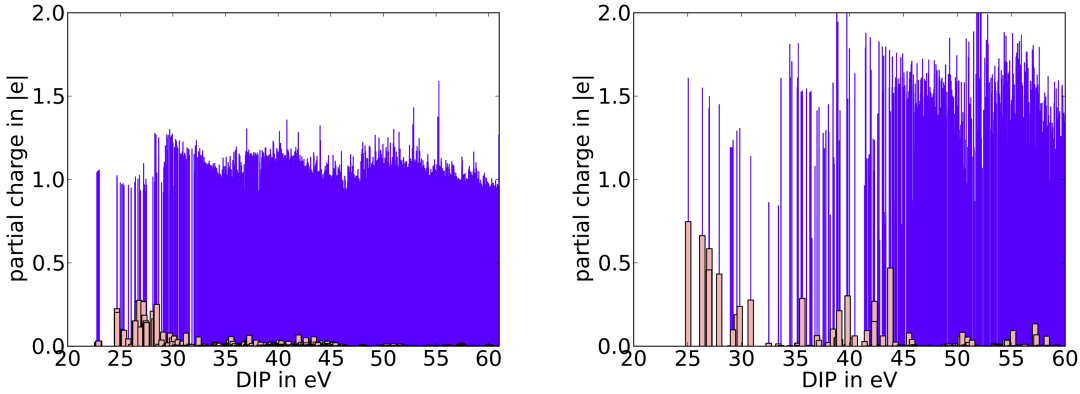

(a) CH_2I_2 **(b)** CH_3I

Figure 5.2: The iodine partial charges (thin, blue sticks) for the dicationic eigenstates and the I^{2+} two-hole populations (thick, rose sticks). DIP denotes the double ionization potential of the dicationic eigenstates which is here approximated by the difference of the energy associated with dicationic eigenstates and the Hartree-Fock ground state energy. It is clearly visible that the iodine partial charges of the dicationic eigenstates of CH_3I are shifted, compared to CH_2I_2, to higher charges. This figure has been published in Ref. [4].

femtoseconds) giving rise to charge distributions as those determined in the previous subsection which were obtained by incoherently averaging over the populated dicationic eigenstates.

Over-the-barrier model and Coulomb explosion model

The charge distributions which arise after iodine-4d ionization of CH_2I_2 and CH_3I investigated in the previous subsections expectably trigger nuclear motion; in particular, the Coulomb repulsion of the emerging ions can initiate fragmentation which results in spatial separation of the repelling ions. The critical distance between molecular fragments that separates the molecular regime from the atomic regime in which no interatomic charge redistribution between the fragments can follow inner-shell ionization, has been found to be well estimated by the so-called over-the-barrier model [64, 66]. According to the over-the-barrier model, this critical distance between two ions is given by the distance where the maximum of the potential barrier between the ions involved seen by the most weakly bound valence electron, is equal to its binding energy. This distance is

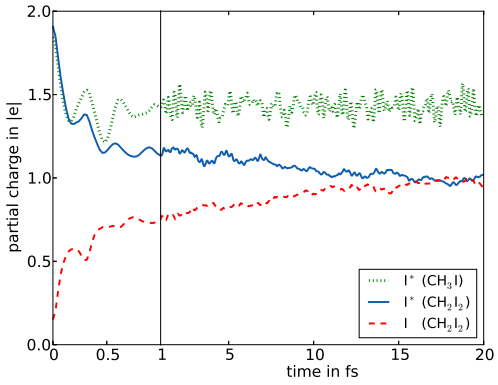

Figure 5.3: The time-dependent partial charges of the iodine atoms after the sudden removal of two atomic iodine valence electrons averaged over all possible initial states (i.e. all possible initial iodine double valence hole states). Here, I^* denotes the iodine site where the two holes were initially situated. In both molecules, most charge appears to be redistributed within less than 1 femtosecond. However, a complete charge equalization in CH_2I_2 occurs only after $\sim$ 15 fs. Note the different timescales used to resolve the fast charge dynamics during the first femtosecond. This figure has been published in Ref. [4].

given by (see Ref. [66]):

$$R_{crit} = \frac{Q_1 + 1 + 2\sqrt{(Q_1+1)Q_2}}{|E_{Q_1}|}. \tag{5.6}$$

Here, Q_1, Q_2 denote the charges of the two ions considered. E_{Q_1} denotes the atomic binding energy of the most weakly bound valence electron of the fragment with charge Q_1. For fragmenting molecules where a (first) photoionization triggers nuclear motion and atomic separation, this critical distance is associated with a critical timespan between this first photo ionization and a second one. That means, a first photoionization triggers the fragmentation; the respective ions start to separate due to Coulomb repulsion and when this critical timespan is elapsed, the fragments reach the critical distance from which on, according to the over-the-barrier model, no interatomic charge redistribution between the fragments can occur. Whether the second photon is absorbed before this critical timespan has elapsed or not determines if interatomic charge redistribution can follow the second photoionization. To obtain a rough estimate of this critical timespan, the following situation is considered: an iodine-4d electron is emitted caused by the absorption of a first XUV photon and the respective molecule undergoes

a molecular Auger decay leaving the molecule doubly ionized whereby positive charge is distributed throughout the entire molecule. Here, the situation is considered where a singly positively charged iodine ion separates from its molecular environment which is singly positively charged as well. On basis of a classical Coulomb explosion model in which both the iodine ion as well as its singly charged molecular environment are modeled by point like ions that solely interact via their Coulomb repulsion, the time-dependent distance between iodine ion and the other fragments is roughly estimated. The initial kinetic energy of the ions in the model is set to zero and their initial positions are set to the positions of the iodine atom in the neutral molecule and the center of mass of the iodine's molecular environment, respectively. Consequently, the critical timespan is estimated by the timespan at which this time-dependent distance coincides with the critical distance obtained from the over-the barrier model. Concretely, for CH_3I, the singly charged methyl group is modeled by a point like ion situated at the center of mass of the constituting carbon and the hydrogen atoms with a mass of 15 u. According to the over-the-barrier model, the critical distance between a singly charged iodine ion and the methyl group in CH_3I, is $\sim$ 7 au. This distance was determined by Eq. 5.6 with the ionization potential $|E_{1+}|$ of the singly charged CH_3 group estimated on the level of Koopmans' theorem to $\sim$ 26 eV. The Coulomb explosion model predicts that the iodine ion and the center of mass of the singly charged methyl group are separated by this distance already after $\sim$ 40 femtoseconds. For CH_2I_2, similar considerations concerning a singly charged iodine ion and a singly charged CH_2I group (with an ionization potential on the level of Koopmans theorem on the order of $\sim$ 17 eV) yield a critical distance on the order of 11 au which can be reached by these fragments after $\sim$ 180 femtoseconds. Importantly, for CH_3I, the iodine ion can apparently be separated from the other fragments within a timespan ($\sim$ 40 femtoseconds) that is smaller than the pulse duration (80 ± 30 femtoseconds). Therefore, for CH_3I, even for overlapping pulses, a singly charged iodine ion that is created by a first photoionization and subsequent Auger decay can be separated from the other fragments so that charge redistribution following a second photoionization is suppressed. In contrast, in CH_2I_2, the two singly positively charged iodine ions remain—within the pulse duration—in close vicinity so that for overlapping pump and probe pulse, charge rearrangement among them following a second photoionization is expectably not suppressed by the fragmentation triggered by the first photoionization. It should be noted that these very different timescales appear to be reflected in the significantly different widths (85 and 235 femtoseconds) of the dip in the I^{3+} signal (see Fig. 5.1). For the experiment considered, also these molecule specific fragmentation timescales can cause the transfer of positive charge from the iodine

sites to their molecular environment to be specific to the molecules considered.

A simplistic model of the relevant processes

In the previous considerations, two mechanisms were identified that can cause that in CH_2I_2 more positive charge is transferred from the iodine sites to their respective molecular environment than in CH_3I. In this subsection, it is pointed out by means of a simplistic model that these two mechanisms can indeed cause such a striking difference of the delay-dependent I^{3+} signal as observed in the experiment. It is important to note that the considerations in this subsection do not aim at a quantitative agreement with the experimental data. In this context, it should be noted that a rigorous theoretical modeling of the concerted motion of electrons and nuclei following ionization of polyatomic molecules appears to be still a general outstanding issue.

To compare with the experimental data, the I^{3+} signal is considered. A prominent sequence of processes that can cause the production of I^{3+} ions is the following one: A first iodine-4d photoionization ensued by a molecular Auger decay causes the distribution of positive charge throughout the entire molecules resulting in a singly charged iodine ion and a singly charged molecular environment of this iodine ion; the resulting charge distributions trigger the fragmentation so that the iodine ion isolates; a second photon ionizes the isolated iodine ion; the ensuing (atomic) Auger decay leaves the ionized iodine fragment triply charged. As discussed in the previous sections, both the distribution of positive charge within the molecule as well as the fragmentation dynamics that follow a first photoionization are strongly molecule specific. To exemplify that this can cause such a striking difference in the I^{3+} signal for vanishing time-delays with respect to large time delays for these two molecules, the following simplifications and assumptions are applied to the rather involved electronic and nuclear dynamics:

1. In accordance with experimental findings (see for instance Ref. [64]), it is assumed that the probability for a charge transfer between two fragments is essentially independent of the distance between them as long as the distance is smaller than the critical distance from which on, according to the over-the-barrier model, the transfer is suppressed.

2. The iodine partial charges are interpreted in terms of a transfer probability of a positive charge from an iodine atom to its molecular environment. For an isolated iodine ion, after an Auger decay, the partial charge would be 2. Neglecting processes in the molecules where two positive charges are transferred simultaneously

from the iodine atom, a partial charge between 1 and 2 can be related to a charge transfer probability. With this, for CH_2I_2, the effective transfer probability of a positive charge from the iodine atom to its molecular environment can be estimated to ~ 1.0 and for CH_3I to ~ 0.6.

3. For quadruply ionized molecules, charge transfer probabilies are assumed that are similar to those estimated for doubly ionized molecules. This assumption is supported by calculations similar to those presented in the above subsections but whose starting point where dicationic molecules. Provided the molecules are still intact when the second photon is absorbed, with these calculations, the partial charge of the iodine atom in CH_3I arising after the second photo ionization and subsequent Auger decay, was estimated to 2.66 $|e|$. After two photoionizations of an isolated iodine ion, each followed by an Auger decay, its partial charge would be 4; a charge expectation value smaller than three indicates a non-vanishing probability for two transfers. Interpreting this charge expectation value (2.66 $|e|$) in terms of a probability for two subsequent transfers, this probability would be 0.34. Consequently, the probability for the second transfer can be assumed to be similar to that for the first one (see assumption 2)) which is on the order of 0.6. (note, $0.6 \times 0.6 \sim 0.34$). Since in the experiment no I^{4+} fragments were found, the probability for the total absence of a transfer after two photo absorptions is concluded to be zero. For CH_2I_2 , iodine partial charges were determined to be on the order of 1.85 $|e|$ which indicates that after a second photoionization, even slightly more than a single positive charge is transferred. This is interpreted in terms of a vanishing probability for the emergence of I^{3+} ions in the situation where the CH_2I_2 molecule is still intact when the second photon is absorbed.

4. The fragmentation dynamics are taken into account phenomenologically in terms of the critical timescale determined in the previous section from which on interatomic charge rearrangement is suppressed.

5. The interaction of the molecules with the pump and the probe pulse are taken into account in a phenomenological way, i.e., the interaction of the molecules with the FEL pulses is modeled by assuming that a photon is absorbed during a pulse effectively within a time span T. The probability for photoionization events taking place in this timespan T during time intervals $[t, t + dt]$ is modeled to be time independent, i.e., independent of t. Here, dt denotes an infinitesimal timespan. In this context, it should be noted that the exact pulse forms are not known and in

particular, the pulse lengths varied significantly by ±30 femtoseconds (note, this corresponds to 0.3 to 0.4 of the average pulse length) so that a more accurate modeling of the FEL pulses appeared unreasonable.

6. Auger cascades, i.e., two subsequent secondary electron emissions following a single iodine 4d ionization, are neglected. This appears reasonable, since predominantly dicationic states are populated below the triple ionization threshold (see Fig. 5.2). For CH_3I, this triple ionization threshold is located approximately at an ionization energy on the order of ~ 50 eV and for CH_2I_2, at ~ 45 eV. The triple ionization threshold was estimated on the level of Koopmans' theorem applied to the dication.

Following a first iodine-4d photoionization of CH_3I molecules, the fragmentation dynamics that ensue a molecular Auger decay of the iodine-4d vacancy can cause spatial separation of the fragments that prevents interatomic charge rearrangement following a second iodine-4d photoionization, i.e., the critical timescale T_{frag} on which this separation occurs is smaller than the pulse length T. Considering the situation in which for vanishing time-delay, the conditional probability for an event in which a second photon is absorbed in time by a molecule (if it is absorbed) so that charge redistribution is still possible, can be estimated on the basis of the above assumption 5) to:

$$p^{t=0}_{\text{no-frag}}(T_{frag}, T) = (2 - \frac{T_{frag}}{T})\frac{T_{frag}}{T}. \tag{5.7}$$

In the experiment, for CH_3I, $\frac{T_{frag}}{T}$ is on the order of 0.5 ± 0.38 so that here, $p^{t=0}_{\text{no-frag}}$ is $\sim 0.75\pm^{0.21}_{0.16}$. For CH_2I_2, however, this probability is for the experimental conditions essentially equal to 1 since the critical timespan ($T_{frag} \sim 180$fs) exceeds the pulse length ($T \sim 100 \pm 30$ femtoseconds).

According to the above considerations and simplifications, the relevant processes for CH_2I_2 are sketched in Fig. 5.4 and for CH_3I in Fig. 5.5. Accordingly, this simplistic model predicts for CH_2I_2 a vanishing I^{3+} signal for vanishing time delays and in fact, in the experimental data one observes that the I^{3+} signal is strongly reduced to less than ~ 0.2 of the value that is obtained for large time delays (~ 400 femtoseconds). For CH_3I, the simplistic model predicts that the I^{3+} signal should be lowered by $0.16\ \pm^{0.06}_{0.12}$ of the value at large time delays ($t \gg 40$fs). Notably, within the error tolerances (which originate from the uncertainty of the pulse duration), this estimate is even in accordance with the experimental value which is found to be between 0.2 to 0.3. Clearly, the model represents a strong simplification of the rather complicated concerted electronic and nuclear motion and the assumptions made are not rigerous which strongly limits the model's

validity. Still, it clearly demonstrates that the two mechanisms presented can potentially cause such a strikingly different delay-dependent I^{3+} signal and thereby support the interpretation of the experimental data in terms of interatomic charge redistribution.

5.3 Conclusions

To conclude, two mechanism were presented that affect the amount of positive charge that is transferred from the iodine atoms in CH_2I_2 and CH_3I to their molecular environment. First, in the course of a molecular Auger decay, charge is predominantly distributed on the iodine atoms—i.e., the atoms with the lowest atomic ionization potential indicating a relaxation of hole charge. As a result, the number of iodine atoms affects the amount of positive charge distributed on each iodine atom. Second, the fragmentation dynamics take place on strongly molecule specific timescales crucially affecting the probability of a charge transfer after a second photo absorption. Based on these two mechanisms, a simplistic model of the relevant processes was developed which reproduces the trends in the experimental data and thereby supports their interpretation in terms of interatomic charge redistribution.

It should be noted that the two mechanisms causing interatomic charge redistribution to be strongly molecule specific can be expected to operate in many systems. For instance, based on the theoretical considerations presented in this chapter, one can expect that the two mechanisms identified can cause a (strongly) molecule specific interatomic charge redistribution also in molecules such as IBr,ICl,IF for which an accurate theoretical modeling appears easier. Using shorter pump and probe pulses might allow to disentangle the two mechanisms discussed. Moreover, based on the results presented in the previous chapters, future experiments might provide more detailed insight into interatomic charge redistribution by using ATAS. In particular, ATAS might reveal possible initial coherent electron dynamics in the dication that can potentially follow secondary electron emission.

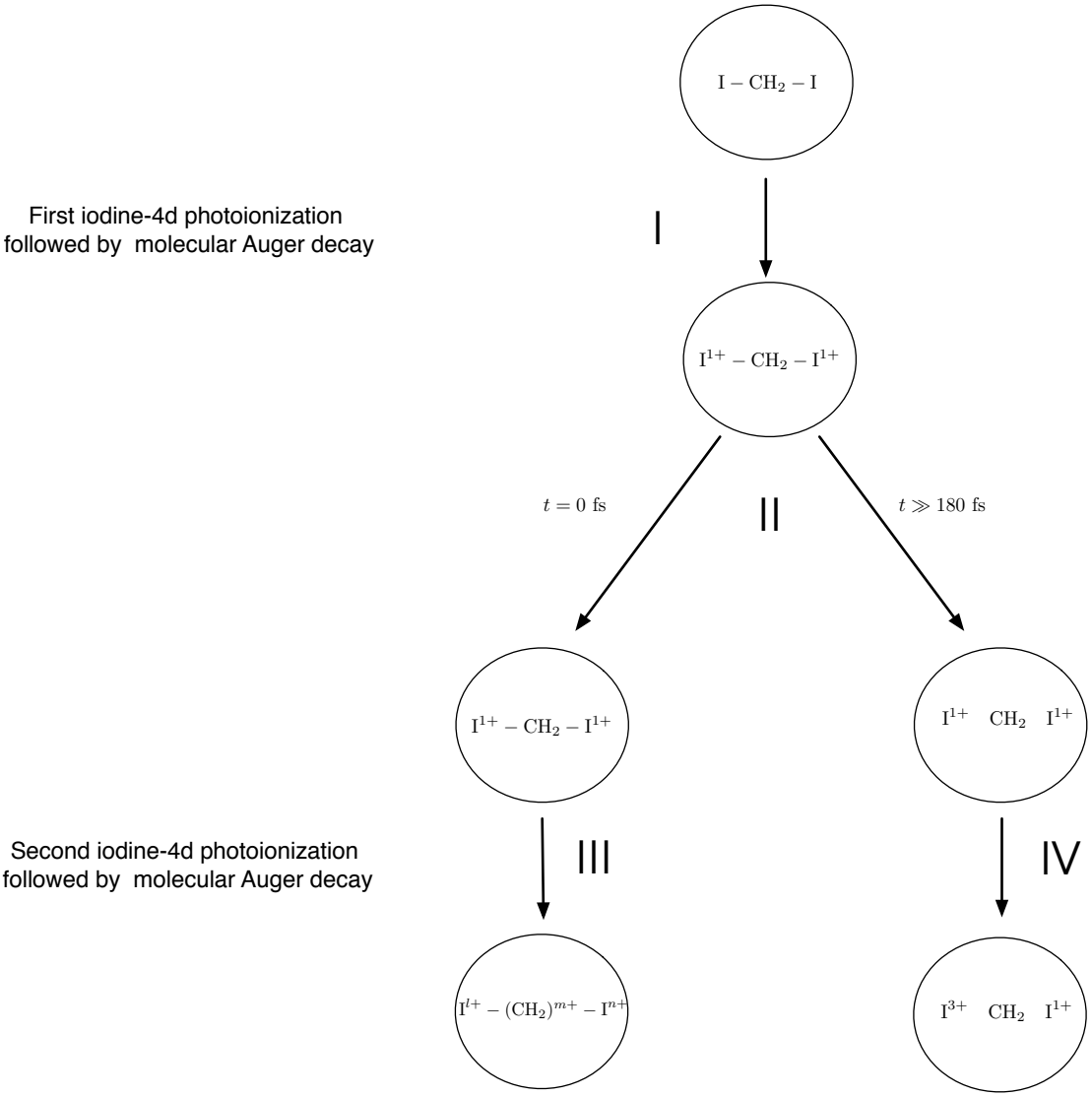

Figure 5.4: The relevant processes that, according to the simplistic model (see text), determine the I^{3+} ion yield arising after two subsequent iodine-4d photoionizations of CH_2I_2 molecules. Two situations are considered: no delay between pump and probe pulse (t = 0) and a delay that is significantly larger than the timescale on which spatial separation of the fragments can occur (i.e., $t \gg 180$ femtoseconds).

I Iodine-4d photo ionization and subsequent molecular Auger decay result in two singly charged iodine ions.

II For overlapping pulses ($t = 0$), the constituents of the doubly ionized molecule CH_2I_2 are in close vicinity to each other so that interatomic charge redistribution follwing a second iodine-4d ionization is possible. For a delay $t \gg 180$ femtoseconds, the fragments are isolated and positive charges induced by iodine-4d ionization remain on the iodine fragments.

III The positive charges are distributed within the entire molecule also after the second iodine-4d photo ionization. No I^{3+} ion is created (l,$n \leq 2$91).

IVA second photon ionizes an isolated singly charged iodine ion. The ensuing atomic Auger decay leaves the ion tripply charged.

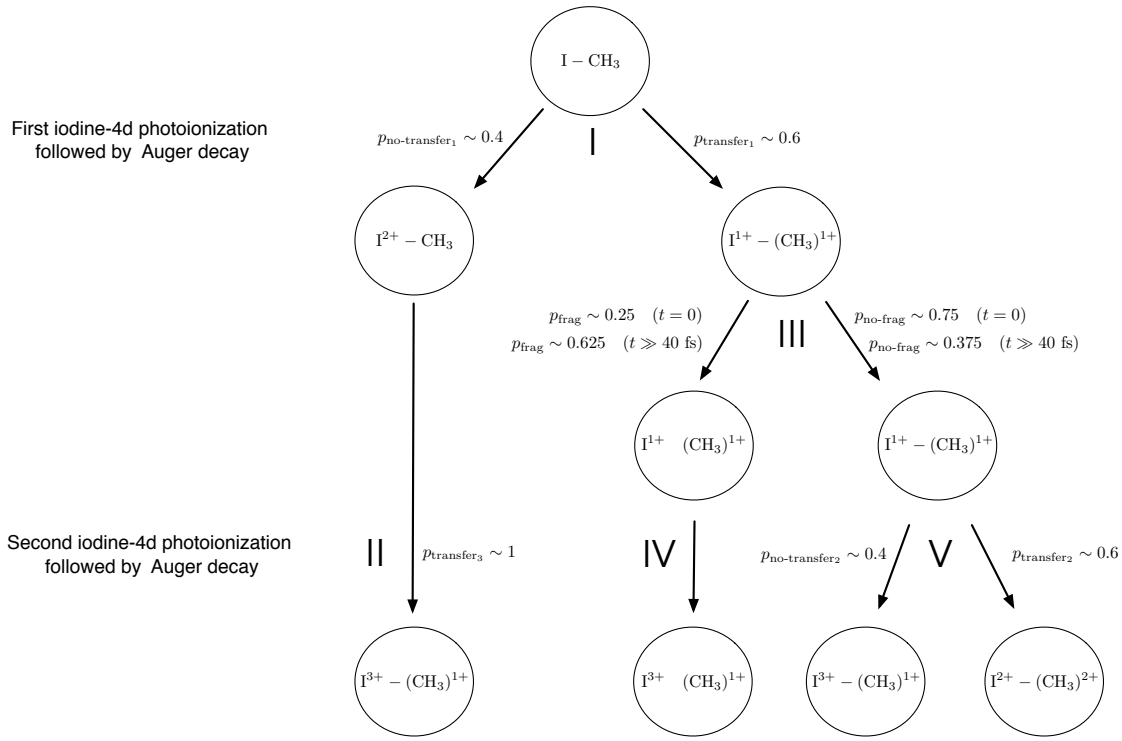

Figure 5.5: The relevant processes that, according to the simplistic model (see text), determine the I^{3+} ion yield arising after two subsequent iodine-4d photoionizations of CH_3I molecules. Two situations are considered: no delay between pump and probe pulse (t = 0) and a delay that is significantly larger than the timescale on which spatial separation of the fragments can occur (i.e., $t \gg 40$ femtoseconds). Note, a hyphen between I^{X+} and the $(CH_3)^{Y+}$ indicates that charge transfer between those ionic fragments can still occur.

I In the course of the molecular Auger decay following the first iodine-4d photoionization, a positive charge is transferred from the iodine atom to the CH_3-group with a probability of 0.6.

II In the experiment, no I^{4+} ions were observed. Therefore, one can conclude that the transfer probability $p_{\mathrm{transfer_3}}$ is ~ 1.

III Following the first photoionization and molecular Auger decay, the fragmentation of the molecule starts. With the probability of p_{frag}, the distance between the fragments enlarges so that no charge redistribution subsequent to a second photoionization is possible.

IV The second photon is absorbed when the iodine ion is separated from the other fragments and positive charge induced by a second photoionization and ensuing Auger decay remains on the isolated iodine atom.

V The second photon is absorbed when the iodine is still in the vicinity of the other fragments and charge redistribution is still possible. In accordance with the simplifying assumptions made, the probability of the first charge transfer can be estimated to 0.6 and the probability of two ensuing transfers—in the situation where the molecule is still intact—to 0.34. This indicates that also for the second photo absorption, the charge transfer probability $p_{\mathrm{transfer_2}}$ is on the order of 0.6.

This figure has been published in Ref. [4].

6 Conclusions and outlook

In **Chapter 2**, the strong-field tunnel ionization of a correlated two-electron quantum system was investigated with regard to multi-electron dynamics. For this, the TDCIS approach, which restricts the dynamics to a single actively participating electron, was benchmarked against the solution of the TDSE, which describes the dynamics of both electrons. The comparison of these two approaches revealed that light-induced multi-electron dynamics affect the ionization probability—i.e., the key observable associated with the process. Complementarily, the solution of the TDSE was analyzed with regard to a collective electron motion and electron correlations. With this, it was demonstrated that the multi-electron effects observed are not only due to ground state correlations but also due to a collective and correlated electron motion induced by the light field. Remarkably, this study also shows that quasi-adiabatic driving by an intense light-field can significantly enhance the correlations between the electrons while they are exposed to the field. Importantly, it was observed that these light-induced multi-electron dynamics become more important the larger the spatial extent of the system is. Hence, in general, multi-electron dynamics during strong-field ionization can be expected to be more prominent the larger the molecular system or nanostructure is that is exposed to a strong-low frequency field. Thus, these findings are relevant for the theoretical modeling and the understanding of strong-field ionization of a wide range of physically, chemically and biologically relevant systems.

In **Chapter 3**, it was demonstrated by means of specific examples how attosecond transient absorption spectroscopy could be used to monitor correlation-driven charge rearrangement. When it is possible to exploit element specific core-to-valence transitions, the electron dynamics can be traced with atomic spatial resolution. Notably, by making use of intra-atomic dipole transitions, the dynamics involving inner and outer-valence shell orbitals can be distinguished which makes ATAS particularly suitably to trace correlation-driven processes following inner-valence ionization. In this context, a characterization of correlation-driven dynamics in terms of the motion of electron holes and a spectating electron was found to be advantageous since it results in predictions that can be directly validated by ATAS. By means of this characterization, it was also

pointed out that correlation-driven processes can initiate coherent hole dynamics that in contrast to outer-valence ionization in general involve two electron holes. Based on the considerations presented, this kind of double-hole migration in polyatomic molecules can be expected to potentially also follow electronic decay processes associated with secondary electron emission.

In **Chapter 4**, the concept of correlation-driven charge migration was extended to double ionization. With this, it was demonstrated that in contrast to single ionization, in doubly ionized molecules, correlation-driven charge migration is particularly prominent; i.e., exceptionally rich and correlated electron dynamics can already follow outer-valence double ionization. Not only is this finding relevant for charge transfer processes following sequential or non-sequential double ionization induced by light pulses but it also concerns charge redistribution that follows inner-shell ionization ensued by secondary electron emission. Namely, as discussed in Chapter 3 and Chapter 5, a molecular Auger decay may initiate (partially) coherent electron dynamics in the dication. Hence, the findings presented concern the real-time dynamics of a multitude of fundamental processes that are relevant for charge redistribution in molecular systems exposed to XUV or X-ray radiation. On basis of the results presented in Chapter 4, one can expect that these electron dynamics are likely to be strongly correlated. It was also shown that these complex dynamics involving up to three vacancies can be well monitored by ATAS. By demonstrating that features in the cross section can be directly related to hole populations, the findings concerning ATAS presented in Chapter 3 are complemented by highlighting the detailedness with which hole dynamics can be monitored.

In **Chapter 5**, charge redistribution following iodine-4d inner-shell ionization of CH_2I_2 and CH_3I molecules was investigated with regard to a recent experiment indicating that interatomic charge redistribution ensuing XUV photoionization in these two molecules is very different—i.e., the amount of positive charge that is transferred from the iodine atoms to their molecular environment appeared to be strongly molecule specific. Here, two mechanism were presented that provide an explanation of the experimental result. First, in the course of a molecular Auger decay, charge is predominantly distributed on the iodine atoms. As a result, the number of iodine atoms determines the amount of positive charge distributed on a each iodine atom. Second, the ensuing fragmentation dynamics take place on strongly molecule specific timescales. The associated isolation of fragments occurring on correspondingly molecule specific timescales can suppress the charge rearrangement following a second iodine-4d photo ionization. Based on these two mechanisms, a simplistic model of the relevant processes was developed which reproduces the trends observed in the experiment.

Based on the results presented in this thesis, there are strong indications that electronic relaxation processes such as a molecular Auger decay can initiate (partially) coherent electron dynamics in the resulting multiply ionized molecular system. It should be noted that the considerations presented in this thesis appear to be the first of this kind concerning the real-time dynamics of electronic processes following secondary electron emission and following double ionization in general so that there remain many open questions. In particular, still unaddressed is the actual dicationic state prepared by secondary electron emission which is expectably strongly molecule specific. The finding that correlation-driven processes following double ionization are of particular importance indicates that the electron dynamics initiated by secondary electron emission are likely to be even more rich, exhibiting even more facets than the dynamics that have been predicted to follow single ionization [1, 10–13]. In addition, the interplay of these electronic charge transfer processes driven by the residual electron-electron interaction with processes induced by nuclear motion occurring on very same timescales [125] can further enhance the complexity of the initial electron dynamics which still remains largely unexplored.

Clearly, the findings presented in this thesis have implications concerning the modeling as well as the understanding of the real-time dynamics of ultrafast charge transfer processes following inner-shell ionization. However, it is not clear if initial electronic coherences have significant consequences for the evolution of molecular systems on long timescales. If this was the case, control of these initial coherent electron dynamics initiated by the secondary electron emission (for instance by a scheme as proposed in Ref. [126]) might provide a possibility to control the evolution that molecules undergo after inner-shell ionization.

This page is intentionally left blank.

7 Appendix to Chapter 2

7.0.1 Effective atomic units

In order to describe the strong-field tunnel ionization of both atomic and molecular systems as well as atom and molecule-like nanostructures (e.g. semiconductor quantum dots), an appropriate unit-system—in the following termed "effective atomic units"—is employed in Chapter 2. This unit system originates from the atomic units by allowing for an effective electron mass whose value does not necessarily coincide with the proper one and by allowing the dielectric constant to be different from one.

Hence, energies are given in effective Hartree $\tilde{E}_H$:

$$\tilde{E}_H = \frac{m^* e^4}{(4\pi\epsilon_0\epsilon_r\hbar)^2}; \tag{7.1}$$

length is given in units of the effective Bohr radius $\tilde{a}_0$:

$$\tilde{a}_0 = \frac{4\pi\epsilon_0\epsilon_r\hbar^2}{m^* e^2}; \tag{7.2}$$

time in units of $\tilde{t}_0$:

$$\tilde{t}_0 = \frac{\hbar}{\tilde{E}_H}; \tag{7.3}$$

velocity in units of $\tilde{v}_0$:

$$\tilde{v}_0 = \frac{\tilde{a}_0\tilde{E}_H}{\hbar}; \tag{7.4}$$

electric field strength in units of $\tilde{\mathcal{E}}_0$:

$$\tilde{\mathcal{E}}_0 = \frac{\tilde{E}_H}{e\tilde{a}_0}; \tag{7.5}$$

and intensity is given in units of $\tilde{I}_0$:

$$\tilde{I}_0 = \tilde{\mathcal{E}}_0^2; \tag{7.6}$$

where m_e^* denotes the effective electron mass, ϵ_0 is the electric constant, ϵ_r is the dielectric constant, $\hbar$ is the Planck constant and e is the electron charge.

For atoms and molecules, the effective electron mass m^* coincides with the electron mass and the dielectric constant ϵ_r is 1. Hence, for atoms and molecules, the chosen unit system coincides with the well-known atomic units. However, for instance for GaAs quantum dots, the effective electron mass m^* is only 0.067 times the electron mass and the dielectric constant ϵ_r is 12.4 so that there for instance an effective Hartree corresponds to ~ 10 meV and an intensity $1.0 \times \tilde{I}_0$ corresponds to only $\sim 2 \times 10^5 \frac{W}{cm^2}$.

7.0.2 Numerical Convergence

In this section of the appendix, the convergence of the numerical implementations of the algorithms described in Chapter 2 is demonstrated. The general proceeding is the following: the ionization probability—i.e. the key observable associated with the process investigated— is determined by the algorithms described. To demonstrate that the set of parameters that determine the accuracy of the algorithms employed is suitable to obtain reliable results, these parameters are varied. It is shown that a change of these parameters towards higher accuracy causes changes of the ionization probability on the order of 0.001 or smaller.

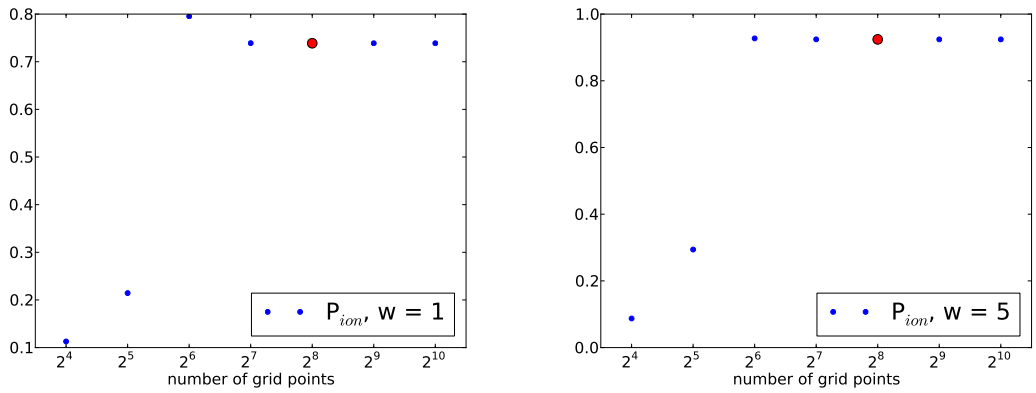

(a) w = 1 **(b)** w = 5

Figure 7.1: The ionization probability at T/2 obtained from the solution of the TDSE in dependence on the number of grid points employed. Δt is set to 0.1 and the parameter C, which determines the strength of the CAP, is set to 0.004. For the calculations presented in Chapter 2, 2^8 grid points (see the red marker in the plot) were employed.

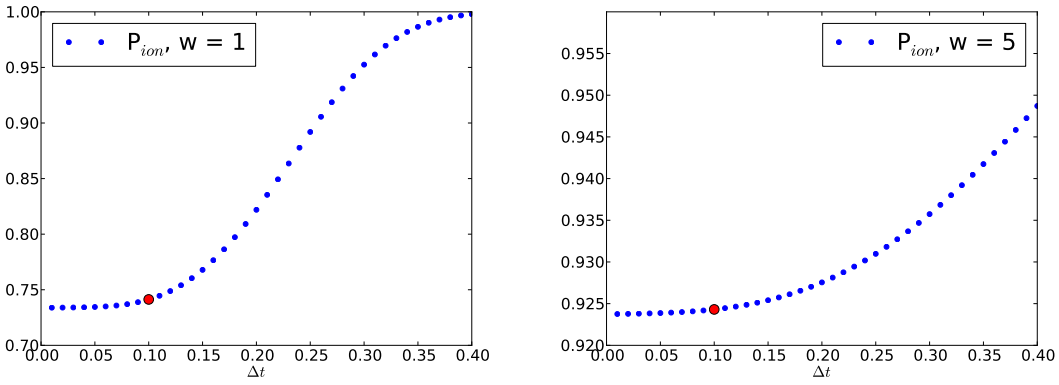

(a) w = 1 **(b)** w = 5

Figure 7.2: The ionization probability at T/2 obtained from the solution of the TDSE in dependence on Δt. The number of grid points employed is set to 2^8 and the parameter C, which determines the strength of the CAP, is set to 0.004. For the calculations presented in Chapter 2, Δt was set to 0.1 (see the red marker in the plot).

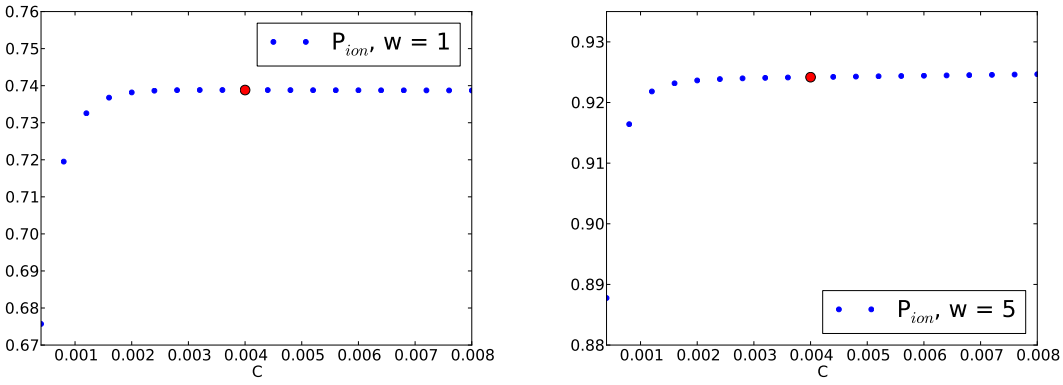

(a) w = 1 **(b)** w = 5

Figure 7.3: The ionization probability at T/2 obtained from the solution of the TDSE in dependence on the parameter C, which determines the strength of the CAP. The number of grid points employed is set to 2^8 and Δt is set to 0.1. For the calculations presented in Chapter 2, C was set to 4×10^{-3} (see the red marker in the plot).

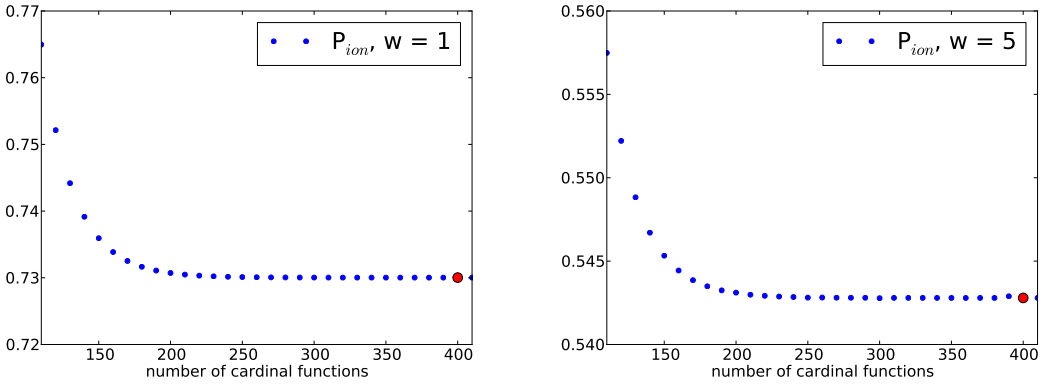

(a) w = 1 **(b)** w = 5

Figure 7.4: The ionization probability at T/2 obtained from the TDCIS approach in dependence on the number of cardinal functions employed for solving the Hartree-Fock equations. Δt is set to 0.1, the parameter C, which determines the strength of the CAP, is set to 0.004, the first 100 Hartree-Fock orbitals (ordered by their orbital energy) were employed to construct the CIS subspace and the Krylov space dimension is set to 10. For the calculations presented in Chapter 2, the number of cardinal functions was set to 400 (see the red marker in the plot).

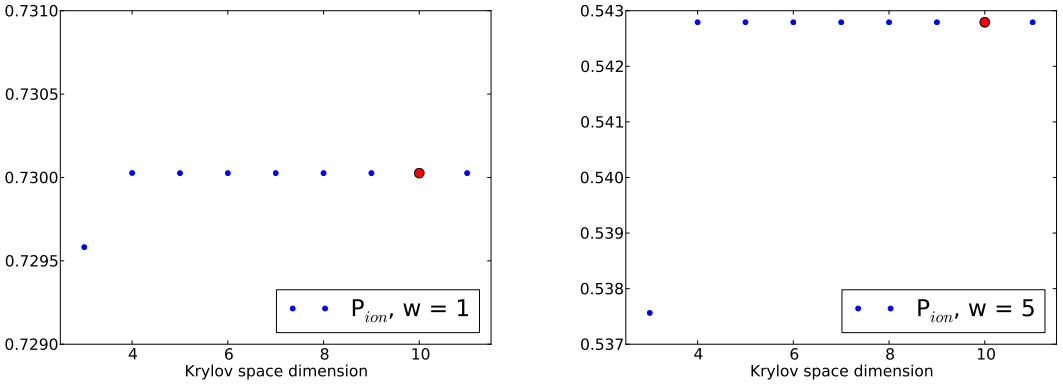

(a) w = 1 **(b)** w = 5

Figure 7.5: The ionization probability at T/2 obtained from the TDCIS approach in dependence on the Krylov space dimension employed for time-evolution. Δt is set to 0.1, the parameter C, which determines the strength of the CAP, is set to 0.004, the number of cardinal functions employed to solve the Hartree-Fock equations is set to 400 and the first 100 Hartree-Fock orbitals (ordered by their orbital energy) were employed to construct the CIS subspace. For the calculations presented in Chapter 2, the Krylov space dimension was set to 10 (see the red marker in the plot).

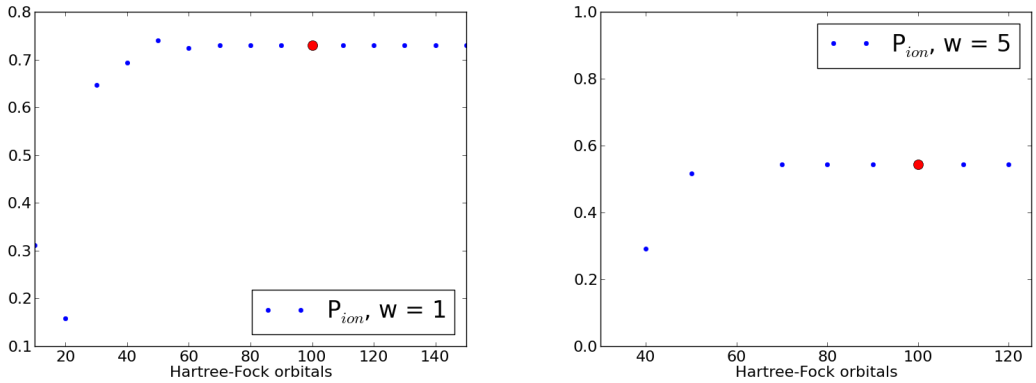

(a) w = 1 **(b)** w = 5

Figure 7.6: The ionization probability at T/2 obtained from the TDCIS approach in dependence on the Hartree-Fock orbitals (ordered by their orbital energy) that were employed to construct the CIS subspace. Δt is set to 0.1, the parameter C, which determines the strength of the CAP, is set to 0.004, the number of cardinal functions employed to solve the Hartree-Fock equations is set to 400 and and the Krylov space dimension is set to 10. For the calculations presented in Chapter 2, the number of Hartree-Fock was set to 100 (see the red marker in the plot).

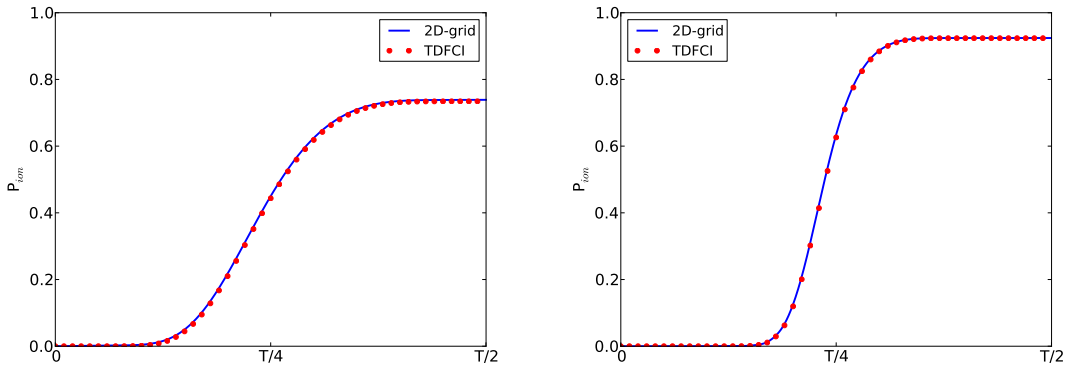

(a) w = 1 **(b)** w = 5

Figure 7.7: The time-dependent ionization probability during the first half-cycle of the laser field considered. By expanding the time-dependent wave function in terms of Hartree-Fock ground state, one-hole one-particle configurations and, two-hole two-particle configurations, the approach based on Hartree-Fock orbitals that was used to determine the TDCIS wave function can be extended to time-dependent Full-CI (TDFCI). Note that the TDFCI approach is equivalent to solving the TDSE. However, this is a much less efficient way to solve the TDSE in comparison to the grid-based approach (2D-grid) that was used to determine the data presented in Chapter 2 but it allows for a few (selected) model parameters (i.e., here for $w = 1$ and $w = 5$) to benchmark and test these two implementation against each other. As demonstrated in this figure, the time-dependent ionization probabilities obtained from these two approaches perfectly coincide. Here, for the TDFCI approach, seven-dimensional Krylov-spaces, 400 cardinal functions and, 70 Hartree-Fock orbitals were employed. For the grid based approach 2^8 grid points were used. Δt was set to 0.1.

8 Appendix to Chapter 3

8.0.1 Special molecular geometry of CH_2BrI

In Chapter 3, calculations were performed that concerned CH_2BrI in a special molecular geometry in which the bonding angle between bromine-carbon and carbon-iodine bond was artificially set to 180°. The actual geometry used for this calculation is given here (the coordinates are given in atomic units):

atom	x	y	z
carbon	0.0	0.0	0.0
hydrogen 1	0.0	-1.13	1.67
hydrogen 2	0.0	-1.13	-1.67
bromine	3.6591	0.0	0.0
iodine	-4.0747	0.0	0.0

8.0.2 Additional remarks concerning the von Neumann entropy

In Chapter 3, it was demonstrated that in C_6H_5Br after the sudden removal of a bromine-4s electron and the subsequent promotion of an electron to initially unoccupied orbitals due to correlation-driven processes within the first femtosecond, the two arising electron holes are initially—in comparison to later times ($\sim$ 10 femtoseconds)—weakly entangled with the excited electron. This is indicated by a von Neumann entropy determined from the normalized two-hole density matrix that, after the creation of both vacancies within one femtosecond, essentially monotonically increases indicating increasing entanglement between the excited electron and the two holes due to their coupling by the residual electron-electron interaction. Note, however, during the excitation dynamics, the von Neumann entropy obtained from the two-hole density matrix behaves differently—i.e., it transiently decreases (see Fig. 3.16a). This feature is not special for the initial state considered and for instance, it also occurs after the prompt removal of an electron from the HOMO-9 orbital (see Fig. 8.1):

$$|\Psi(t=0)\rangle = c_{HOMO-9}|\Psi_0\rangle. \tag{8.1}$$

Since the subsequent discussion is simpler for an initial Hartree-Fock 1h configuration, the feature will be discussed by means of the dynamics that follow the promt removal of a HOMO-9 electron from the CH_2BrI molecule. The conclusions drawn, however, also apply to the situation considered in Chapter 3 where a situation was investigated in which a superposition of two Hartree-Fock 1h configuration was considered. The dynamics that ensue the preparation of this HOMO-9 1h configuration are very similar to the dynamics that follow the preparation of a bromine-4s vacancy (in this context it should be noted that the overlap of the bromine-4s orbital with the HOMO-9 of the C_6H_5Br molecule is significant, i.e., $\langle$bromine-4s$|$HOMO-9$\rangle \sim 0.78$; hence these initial states are similar). As indicated in Fig. 8.1c, initially, during the excitation dynamics, predominantly 2h1p configurations are populated in which the spatial orbital of one of the two holes coincides with that of the initial hole while the spatial orbital of the other differs from it (denoted in Fig. 8.1c as (HOMO-9,x)). Only towards the end of the excitation dynamics, processes gain importance which lead to the population of 2h1p configurations in which the spatial orbitals of both holes differ from that of the initial one (denoted by (x,y)). This effect has already been observed in Refs. [70, 127]. Note, this population of the kind of 2h1p-configurations denoted as (x,y) accompanies the initial decrease of the von Neumann entropy (see Fig. 8.1c). In this context, one should note that the electron-electron interaction induces predominantly transitions between a 1h configuration $c_i|\Phi_0\rangle$ and those 2h1p configurations $c_k^\dagger c_l c_m|\Phi_0\rangle$ that are energetically close (as easily verified by considering the first order perturbation correction with respect to the residual electron-electron interaction), i.e.

$$\langle\Phi_0|c_i^\dagger H c_i|\Phi_0\rangle \sim \langle\Phi_0|c_m^\dagger c_l^\dagger c_k H c_k^\dagger c_l c_m|\Phi_0\rangle \tag{8.2}$$

where H denotes the ionic Hamiltonian.

When approximating the expectation values in terms of orbital energies and thereby neglecting, for the sake of transparency, the residual electron-electron interaction (note, this simplification does not affect the following arguments), the condition in Eq. 8.2 translates into:

$$0 \sim \epsilon_k - \epsilon_l - \epsilon_m + \epsilon_i \tag{8.3}$$

where ϵ_k denotes the orbital energy of the excited electron, i.e., the particle, $-\epsilon_l - \epsilon_m$ denotes the orbital energies of the two holes of the 2h1p configuration and $-\epsilon_i$ denotes the orbital energy of the hole in the 1h configuration. For the 2h1p configurations of type (HOMO-9,x), this means:

$$0 \sim \epsilon_k - \epsilon_x \tag{8.4}$$

where ϵ_k denotes the orbital energy of the particle and $-\epsilon_x$ is the orbital energy of the hole in the 2h1p configuration whose spatial orbital does not coincide with that of the initial one. Clearly, this energy constraint is more restrictive for 2h1p configurations of the kind (HOMO-9,x)(Eq. 8.4) than for those of the kind (x,y) (both hole orbital energies can be varied; Eq. 8.3) and hence, entanglement between holes and excited electron due to this constraint can be larger when 2h1p configurations of the kind (HOMO-9,x) are predominantly populated with respect to a situation in which essentially only those of the kind (x,y) are populated. This may provide an explanation for the initial decrease of the von Neumann entropy that accompanies the increase of the weight of 2h1p configurations of the kind (x,y) in the 2h1p component of the wave function during the first few hundred attoseconds.

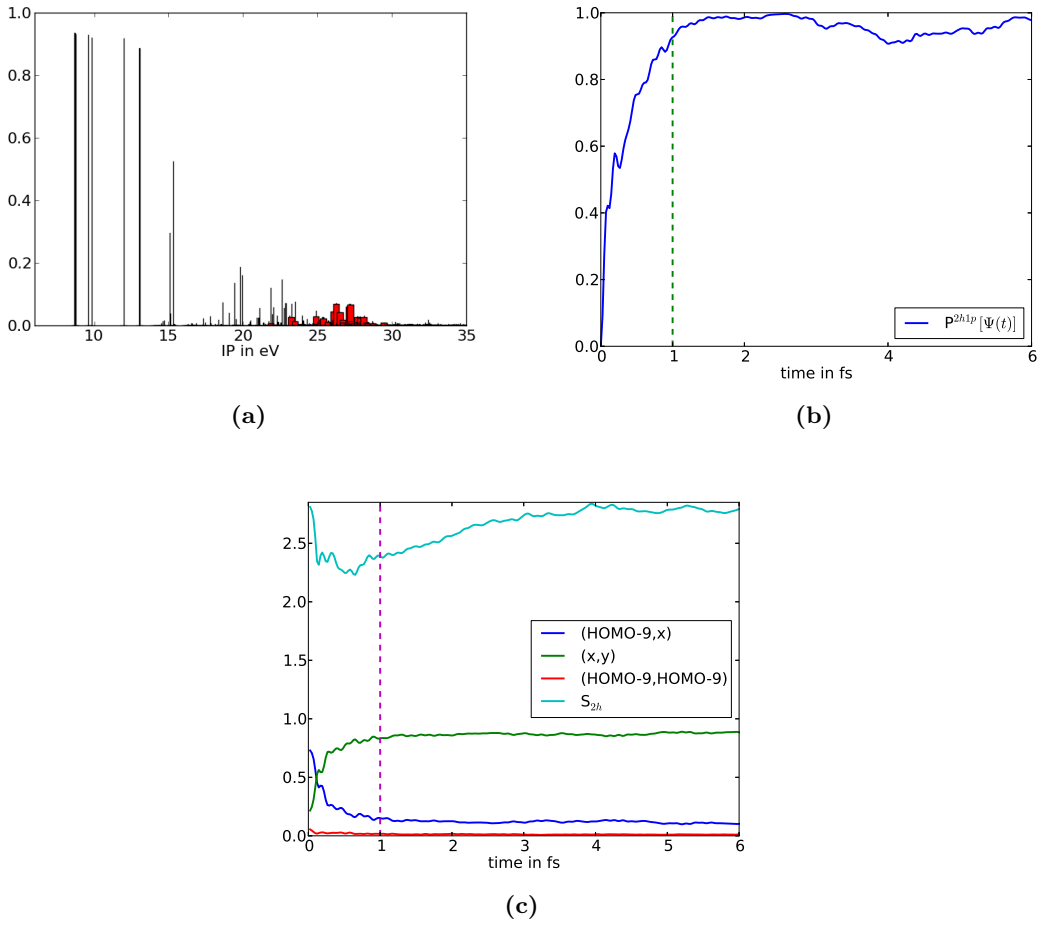

Figure 8.1: The dynamics following the prompt removal of an electron from the HOMO-9 of the CH_2BrI molecule is considered. a) The spectral decomposition of the HOMO-9 1h configuration(red bars) and the one-hole weights of the cationic eigenstates. IP denotes the ionization potential which is here approximated by difference of the energy associated with cationic eigenstates and the Hartree-Fock ground state energy. b) The 2h1p weight of the time-evolved state which increases within one femtosecond from 0 to ~ 1. Hence, within one femtosecond, an electron is promoted to the virtual orbitals. c) The time-dependent von Neuman entropy obtained from the two-hole density matrix (turquoise curve). The weight of the 2h1p configurations in the 2h1p component of the time-dependent wave function in which one vacancy coincides with the initial one whereas the other one is different (denoted by (HOMO-9,x), blue curve). The weight of the 2h1p configurations in which both vacancies are different from the initial vacancy (denoted by (x,y), green curve). The part of the 2h1p configurations in which both vacancies are in the HOMO-9 (denoted by (HOMO-9,HOMO-9), red curve). Note, before determining the weights (HOMO-9,HOMO-9),(HOMO-9,x) and (x,y), the 2h1p component of the time-dependent wave function was normalized.

8.0.3 Numerical convergence

In this subsection a few numerical details concerning the calculations presented in Chapter 3 are discussed.

Atomic orbital basis sets

For the calculations presented, effective core potentials and associated orbital basis sets taken from [107] (iodine), [108](carbon) and respectively [109](bromine) were used and for the hydrogen atoms 6-31G basis sets were employed.

Virtual orbitals - Calculations concerning CH_2BrI

Due to practical reasons, only a limited number of virtual orbitals can be included into the calculation (in particular, since the determination of the ATA spectra is computationally demanding). Here, the concrete number of virtuals was chosen such that trends are reproduced which were obtained from a reference calculation concerning solely the valence charge dynamics. For this reference calculation, valence orbital basis sets for the halogene atoms [124] were employed allowing to conveniently include all (38) virtual orbitals associated with that basis set. As shown in Fig. 8.2a, the trends are reproduced already when 15 virtual orbitals are included. All results presented in Chapter 3 were obtained from calculations in which 15 virtual orbitals were included.

Virtual orbitals - Calculations concerning C_6H_5Br

The charge dynamics in the C_6H_5Br molecule also discussed in Chapter 3 appears to be quickly converged already when only 5 virtual orbitals are included in the calculation. This is shown in Fig. 8.3 where two-hole partial charge of the hydrogen atom H_6 (see Fig. 3.13 in Chapter 3) is shown in dependence of the number of virtual orbitals (ordered by their orbital energy) included. For the results presented, 15 orbitals where employed.

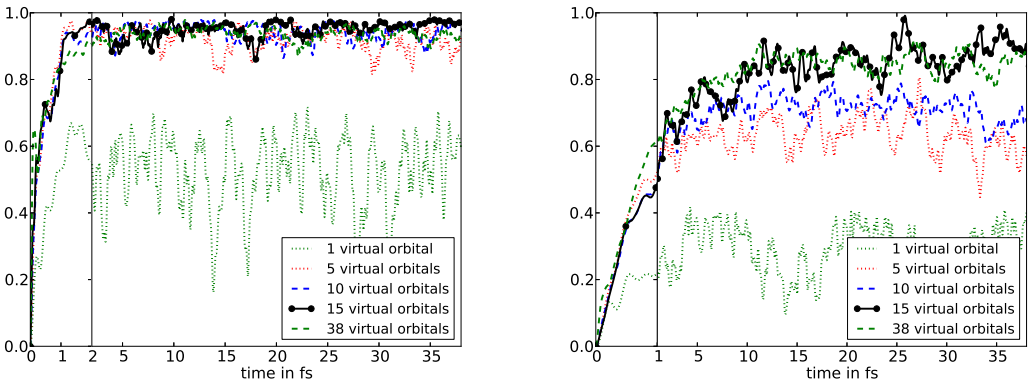

Figure 8.2: a) The time-dependent 2h1p weight (see Eq. 3.31) in dependence of the number of virtual orbitals (ordered by their orbital energy) included in the calculation. b) The time-dependent two-hole partial charge of the iodine atom in dependence of the number of virtual orbitals included. Except for fluctuations, the trends observed in a reference calculation including all 38 virtual orbitals (see text) are reproduced when those 15 virtual orbitals with the lowest orbital energies are taken into account in the calculation.

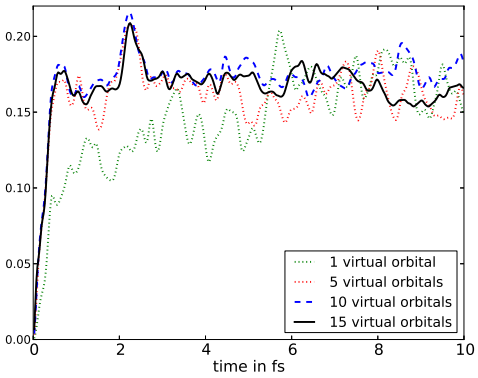

Figure 8.3: The time-dependent 2h partial charges of the hydrogen atom H_6 (see Fig. 3.13 in Chapter 3) considered in the calculation concerning C_6H_5Br. The short time dynamics (i.e., the initial few femtoseconds) discussed in Chapter 3 appears to be essentially converged when only 5 virtual orbitals are included in the calculation.

9 Appendix to Chapter 4

The accuracy of the results presented in Chapter 4 depends on the number of virtual orbitals included in the calculation. In the calculations presented, 4 virtual orbitals are considered. Here, it is demonstrated that the features in the ATA spectra discussed in Chapter 4 do not significantly change when the number of virtual orbitals (ordered by their orbital energy) is further increased. For this purpose, the ATA spectra were determined for various numbers of virtual orbitals included in the calculation. As shown in Fig. 9.1, the features discussed appear already when two virtual orbitals are included in the calculation and when more than two virtual orbitals are included, only minor changes occur.

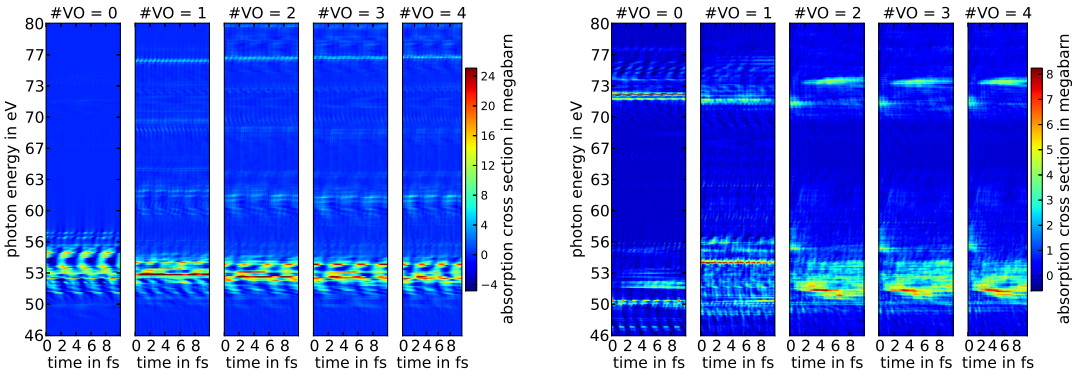

Figure 9.1: The time-resolved absorption cross section in dependence of the number of virtual orbitals (VO) that are included in the calculations. Here, the situations are considered where a) two electrons are removed from the HOMO and b) two electrons are removed from the HOMO-5. Already by inclusion of two virtual orbitals, the features discussed arise. The data presented in the chapter were obtained from calculations in which 4 virtual orbitals were included.

This page is intentionally left blank.

Bibliography

[1]L. Cederbaum and J. Zobeley, "Ultrafast charge migration by electron correlation", Chemical Physics Letters **307**, 205 –210 (1999).

[2]F. Lepine, M. Y. Ivanov, and M. J. J. Vrakking, "Attosecond molecular dynamics: fact or fiction?", Nat. Photon. **8**, 195–204 (2014).

[3]F. Calegari, D. Ayuso, A. Trabattoni, L. Belshaw, S. De Camillis, S. Anumula, F. Frassetto, L. Poletto, A. Palacios, P. Decleva, J. B. Greenwood, F. Martín, and M. Nisoli, "Ultrafast electron dynamics in phenylalanine initiated by attosecond pulses", Science **346**, 336–339 (2014).

[4]M. Hollstein, K. Mertens, N. Gerken, S. Klumpp, S. Palutke, I. Baev, G. Brenner, S. Dziarzhytski, W. Wurth, D. Pfannkuche, and M. Martins, "Ultrafast charge redistribution in small iodine containing molecules", arXiv:1605.09317 (2016).

[5]K. Glusac, "What has light ever done for chemistry?", Nat. Chem. **8**, 734–735 (2016).

[6]Editorial, "A sunny outlook", Nat. Photon. **6**, 129 (2012).

[7]G. Li, R. Zhu, and Y. Yang, "Polymer solar cells", Nat. Photon. **6**, 153–161 (2012).

[8]B. E. Hardin, H. J. Snaith, and M. D. McGehee, "The renaissance of dye-sensitized solar cells", Nat. Photon. **6**, 162–169 (2012).

[9]G. S. Engel, T. R. Calhoun, E. L. Read, T.-K. Ahn, T. Mancal, Y.-C. Cheng, R. E. Blankenship, and G. R. Fleming, "Evidence for wavelike energy transfer through quantum coherence in photosynthetic systems", Nature **446**, 782–786 (2007).

[10]A. I. Kuleff, S. Lünnemann, and L. S. Cederbaum, "Electron-correlation-driven charge migration in oligopeptides", Chemical Physics **414**, 100 –105 (2013).

[11]A. I. Kuleff, S. Lünnemann, and L. S. Cederbaum, "Ultrafast Charge Migration Following Valence Ionization of 4-Methylphenol: Jumping over the Aromatic Ring", The Journal of Physical Chemistry A **114**, 8676–8679 (2010).

[12]A. I. Kuleff and L. S. Cederbaum, "Charge migration in different conformers of glycine: the role of nuclear geometry", Chemical Physics **338**, 320 –328 (2007).

[13]A. I. Kuleff and L. S. Cederbaum, "Ultrafast correlation-driven electron dynamics", Journal of Physics B: Atomic, Molecular and Optical Physics **47**, 124002 (2014).

[14]F. Remacle and R. D. Levine, "An electronic time scale in chemistry", Proceedings of the National Academy of Sciences **103**, 6793–6798 (2006).

[15]M. Hentschel, R. Kienberger, C. Spielmann, G. A. Reider, N. Milosevic, T. Brabec, P. Corkum, U. Heinzmann, M. Drescher, and F. Krausz, "Attosecond metrology", Nature **414**, 509–513 (2001).

[16]F. Krausz and M. Ivanov, "Attosecond physics", Rev. Mod. Phys. **81**, 163–234 (2009).

[17]E. Goulielmakis, Z.-H. Loh, A. Wirth, R. Santra, N. Rohringer, V. S. Yakovlev, S. Zherebtsov, T. Pfeifer, A. M. Azzeer, M. F. Kling, S. R. Leone, and F. Krausz, "Real-time observation of valence electron motion", Nature **466**, 739–743 (2010).

[18]P. M. Kraus, B. Mignolet, D. Baykusheva, A. Rupenyan, L. Horný, E. F. Penka, G. Grassi, O. I. Tolstikhin, J. Schneider, F. Jensen, L. B. Madsen, A. D. Bandrauk, F. Remacle, and H. J. Wörner, "Measurement and laser control of attosecond charge migration in ionized iodoacetylene", Science **350**, 790–795 (2015).

[19]S. R. Leone, C. W. McCurdy, J. Burgdorfer, L. S. Cederbaum, Z. Chang, N. Dudovich, J. Feist, C. H. Greene, M. Ivanov, R. Kienberger, U. Keller, M. F. Kling, Z.-H. Loh, T. Pfeifer, A. N. Pfeiffer, R. Santra, K. Schafer, A. Stolow, U. Thumm, and M. J. J. Vrakking, "What will it take to observe processes in 'real time'?", Nat. Photon. **8**, 162–166 (2014).

[20]M. Hollstein and D. Pfannkuche, "Multielectron dynamics in the tunneling ionization of correlated quantum systems", Phys. Rev. A **92**, 053421 (2015).

[21]M. Lewenstein, P. Balcou, M. Y. Ivanov, A. L'Huillier, and P. B. Corkum, "Theory of high-harmonic generation by low-frequency laser fields", Phys. Rev. A **49**, 2117–2132 (1994).

[22]N. Rohringer and R. Santra, "Multichannel coherence in strong-field ionization", Phys. Rev. A **79**, 053402 (2009).

[23]K. C. Kulander, "Time-dependent theory of multiphoton ionization of xenon", Phys. Rev. A **38**, 778–787 (1988).

[24]K. Kulander and T. Rescigno, "Effective potentials for time-dependent calculations of multiphoton processes in atoms", Computer Physics Communications **63**, 523 –528 (1991).

[25]K. C. Kulander and B. W. Shore, "Calculations of multiple-harmonic conversion of 1064-nm radiation in xe", Phys. Rev. Lett. **62**, 524–526 (1989).

[26]N. Rohringer, A. Gordon, and R. Santra, "Configuration-interaction-based time-dependent orbital approach for *ab initio* treatment of electronic dynamics in a strong optical laser field", Phys. Rev. A **74**, 043420 (2006).

[27]S. Pabst and R. Santra, "Strong-field many-body physics and the giant enhancement in the high-harmonic spectrum of xenon", Phys. Rev. Lett. **111**, 233005 (2013).

[28]J. C. Tremblay, T. Klamroth, and P. Saalfrank, "Time-dependent configuration-interaction calculations of laser-driven dynamics in presence of dissipation", The Journal of Chemical Physics **129**, 084302 (2008).

[29]W. A. de Heer, "The physics of simple metal clusters: experimental aspects and simple models", Rev. Mod. Phys. **65**, 611–676 (1993).

[30]S. M. Reimann and M. Manninen, "Electronic structure of quantum dots", Rev. Mod. Phys. **74**, 1283–1342 (2002).

[31]K. Raghavachari and J. B. Anderson, "Electron correlation effects in molecules", The Journal of Physical Chemistry **100**, 12960–12973 (1996).

[32]D. Pfannkuche, V. Gudmundsson, and P. A. Maksym, "Comparison of a Hartree, a Hartree-Fock, and an exact treatment of quantum-dot helium", Phys. Rev. B **47**, 2244–2250 (1993).

[33]D. Pfannkuche, R. R. Gerhardts, P. A. Maksym, and V. Gudmundsson, "Theory of quantum dot helium", Physica B: Condensed Matter **189**, 6 –15 (1993).

[34]B Szafran, J Adamowski, and S Bednarek, "Electron-electron correlation in quantum dots", Physica E: Low-dimensional Systems and Nanostructures **5**, 185 –195 (1999).

[35]T. M. Henderson, K. Runge, and R. J. Bartlett, "Electron correlation in artificial atoms", Chemical Physics Letters **337**, 138 –142 (2001).

[36]L. V. Keldysh, "Ionization in the field of a strong electromagnetic wave", Soviet Phys. JETP **2354**, 1307 (1964).

[37]L. Jacak, P. Hawrylak, and A. Wojs, *Quantum dots (nanoscience and technology)* (Springer, 1998).

[38]J. Adamowski, M. Sobkowicz, B. Szafran, and S. Bednarek, "Electron pair in a gaussian confining potential", Phys. Rev. B **62**, 4234–4237 (2000).

[39]W.-C. Liu, J. H. Eberly, S. L. Haan, and R. Grobe, "Correlation effects in two-electron model atoms in intense laser fields", Phys. Rev. Lett. **83**, 520–523 (1999).

[40]D. Bauer, "Two-dimensional, two-electron model atom in a laser pulse: exact treatment, single-active-electron analysis, time-dependent density-functional theory, classical calculations, and nonsequential ionization", Phys. Rev. A **56**, 3028–3039 (1997).

[41]M. S. Pindzola, F. Robicheaux, and P. Gavras, "Double multiphoton ionization of a model atom", Phys. Rev. A **55**, 1307–1313 (1997).

[42]J. Rapp and D. Bauer, "Effects of inner electrons on atomic strong-field-ionization dynamics", Phys. Rev. A **89**, 033401 (2014).

[43]W. Häusler and B. Kramer, "Interacting electrons in a one-dimensional quantum dot", Phys. Rev. B **47**, 16353–16357 (1993).

[44]O. Ciftja and M. G. Faruk, "Two interacting electrons in a one-dimensional parabolic quantum dot: exact numerical diagonalization", Journal of Physics: Condensed Matter **18**, 2623 (2006).

[45]Y. Sajeev and N. Moiseyev, "Theory of autoionization and photoionization in two-electron spherical quantum dots", Phys. Rev. B **78**, 075316 (2008).

[46]U. Merkt, J. Huser, and M. Wagner, "Energy spectra of two electrons in a harmonic quantum dot", Phys. Rev. B **43**, 7320–7323 (1991).

[47]P.-O. Löwdin and H. Shull, "Natural orbitals in the quantum theory of two-electron systems", Phys. Rev. **101**, 1730–1739 (1956).

[48]O. Shemer, D. Brisker, and N. Moiseyev, "Optimal reflection-free complex absorbing potentials for quantum propagation of wave packets", Phys. Rev. A **71**, 032716 (2005).

[49]L. Greenman, P. J. Ho, S. Pabst, E. Kamarchik, D. A. Mazziotti, and R. Santra, "Implementation of the time-dependent configuration-interaction singles method for atomic strong-field processes", Phys. Rev. A **82**, 023406 (2010).

[50]M. Feit, J. Fleck, and A Steiger, "Solution of the Schrödinger equation by a spectral method", Journal of Computational Physics **47**, 412 –433 (1982).

[51]MATLAB, *Version 8.1.0.604 (r2013a)* (The MathWorks Inc., Natick, Massachusetts, 2013).

[52]M. Nest, T. Klamroth, and P. Saalfrank, "The multiconfiguration time-dependent Hartree-Fock method for quantum chemical calculations", The Journal of Chemical Physics **122**, 124102 (2005).

[53]J. Wang, S.-I. Chu, and C. Laughlin, "Multiphoton detachment of h^-. ii. intensity-dependent photodetachment rates and threshold behavior complex-scaling generalized pseudospectral method", Phys. Rev. A **50**, 3208–3215 (1994).

[54]M. Galassi et al., *Gnu scientific library reference manual - third edition* (Network Theory Ltd., 2009).

[55]T. J. Park and J. C. Light, "Unitary quantum time evolution by iterative Lanczos reduction", The Journal of Chemical Physics **85**, 5870 (1986).

[56]G. Guennebaud, B. Jacob, et al., *Eigen v3*, http://eigen.tuxfamily.org, 2010.

[57]P.-O. Löwdin, "Quantum theory of cohesive properties of solids", Advances in Physics **5**, 1–171 (1956).

[58]U. Merkt, J. Huser, and M. Wagner, "Energy spectra of two electrons in a harmonic quantum dot", Phys. Rev. B **43**, 7320–7323 (1991).

[59]K. J. H. Giesbertz, Ph.D. thesis, Free University Amsterdam (2010).

[60]M. Brics and D. Bauer, "Time-dependent renormalized natural orbital theory applied to the two-electron spin-singlet case: ground state, linear response, and autoionization", Phys. Rev. A **88**, 052514 (2013).

[61]S. L. Haan, R. Grobe, and J. H. Eberly, "Numerical study of autoionizing states in completely correlated two-electron systems", Phys. Rev. A **50**, 378–391 (1994).

[62]M. Lezius, V. Blanchet, D. M. Rayner, D. M. Villeneuve, A. Stolow, and M. Y. Ivanov, "Nonadiabatic multielectron dynamics in strong field molecular ionization", Phys. Rev. Lett. **86**, 51–54 (2001).

[63]M. Hollstein, R. Santra, and D. Pfannkuche, "Exceptionally strong correlation-driven charge migration and attosecond transient absorption spectroscopy", arXiv:1605.06762 (2016).

[64]B. Erk, R. Boll, S. Trippel, D. Anielski, L. Foucar, B. Rudek, S. W. Epp, R. Coffee, S. Carron, S. Schorb, K. R. Ferguson, M. Swiggers, J. D. Bozek, M. Simon, T. Marchenko, J. Küpper, I. Schlichting, J. Ullrich, C. Bostedt, D. Rolles, and A. Rudenko, "Imaging charge transfer in iodomethane upon x-ray photoabsorption", Science **345**, 288–291 (2014).

[65]B. Erk, D. Rolles, L. Foucar, B. Rudek, S. W. Epp, M. Cryle, C. Bostedt, S. Schorb, J. Bozek, A. Rouzee, A. Hundertmark, T. Marchenko, M. Simon, F. Filsinger, L. Christensen, S. De, S. Trippel, J. Küpper, H. Stapelfeldt, S. Wada, K. Ueda, M. Swiggers, M. Messerschmidt, C. D. Schröter, R. Moshammer, I. Schlichting, J. Ullrich, and A. Rudenko, "Ultrafast Charge Rearrangement and Nuclear Dynamics upon Inner-Shell Multiple Ionization of Small Polyatomic Molecules", Phys. Rev. Lett. **110**, 053003 (2013).

[66]K. Schnorr, A. Senftleben, M. Kurka, A. Rudenko, G. Schmid, T. Pfeifer, K. Meyer, M. Kübel, M. F. Kling, Y. H. Jiang, R. Treusch, S. Düsterer, B. Siemer, M. Wöstmann, H. Zacharias, R. Mitzner, T. J. M. Zouros, J. Ullrich, C. D. Schröter, and R. Moshammer, "Electron Rearrangement Dynamics in Dissociating I_2^{n+} Molecules Accessed by Extreme Ultraviolet Pump-Probe Experiments", Phys. Rev. Lett. **113**, 073001 (2014).

[67]L. S. Cederbaum, J. Zobeley, and F. Tarantelli, "Giant intermolecular decay and fragmentation of clusters", Phys. Rev. Lett. **79**, 4778–4781 (1997).

[68]K. Gokhberg, P. Kolorenc, A. I. Kuleff, and L. S. Cederbaum, "Site- and energy-selective slow-electron production through intermolecular Coulombic decay", Nature **505**, 661–663 (2014).

[69]T. Jahnke, "Interatomic and intermolecular coulombic decay: the coming of age story", Journal of Physics B: Atomic, Molecular and Optical Physics **48**, 082001 (2015).

[70]A. I. Kuleff and L. S. Cederbaum, "Tracing ultrafast interatomic electronic decay processes in real time and space", Phys. Rev. Lett. **98**, 083201 (2007).

[71]S. Pabst, L. Greenman, P. J. Ho, D. A. Mazziotti, and R. Santra, "Decoherence in attosecond photoionization", Phys. Rev. Lett. **106**, 053003 (2011).

[72]E. Anderson, Z. Bai, C. Bischof, S. Blackford, J. Demmel, J. Dongarra, J. Du Croz, A. Greenbaum, S. Hammarling, A. McKenney, and D. Sorensen, *LAPACK users' guide*, Third (Society for Industrial and Applied Mathematics, Philadelphia, PA, 1999).

[73]G. Karlström, R. Lindh, P.-Å. Malmqvist, B. O. Roos, U. Ryde, V. Veryazov, P.-O. Widmark, M. Cossi, B. Schimmelpfennig, P. Neogrady, and L. Seijo, "MOLCAS: a program package for computational chemistry ", Computational Materials Science **28**, Proceedings of the Symposium on Software Development for Process and Materials Design, 222–239 (2003).

[74]E. F. Valeev, "LIBINT: A library for the evaluation of molecular integrals of many-body operators over Gaussian functions, Version 2.0.3", http://libint.valeyev.net/.

[75]T. Kuś, B. Mignolet, R. D. Levine, and F. Remacle, "Pump and Probe of Ultrafast Charge Reorganization in Small Peptides: A Computational Study through Sudden Ionizations", The Journal of Physical Chemistry A **117**, 10513–10525 (2013).

[76]B. Mignolet, R. D. Levine, and F. Remacle, "Localized electron dynamics in attosecond-pulse-excited molecular systems: probing the time-dependent electron density by sudden photoionization", Phys. Rev. A **86**, 053429 (2012).

[77]B. Cooper and V. Averbukh, "Single-photon laser-enabled Auger spectroscopy for measuring attosecond electron-hole dynamics", Phys. Rev. Lett. **111**, 083004 (2013).

[78]J. Leeuwenburgh, B. Cooper, V. Averbukh, J. P. Marangos, and M. Ivanov, "High-order harmonic generation spectroscopy of correlation-driven electron hole dynamics", Phys. Rev. Lett. **111**, 123002 (2013).

[79]D. Popova-Gorelova and R. Santra, "Imaging instantaneous electron flow with ultrafast resonant x-ray scattering", Phys. Rev. B **91**, 184303 (2015).

[80]A. D. Dutoi, K. Gokhberg, and L. S. Cederbaum, "Time-resolved pump-probe spectroscopy to follow valence electronic motion in molecules: theory", Phys. Rev. A **88**, 013419 (2013).

[81]H. Wang, M. Chini, S. Chen, C.-H. Zhang, F. He, Y. Cheng, Y. Wu, U. Thumm, and Z. Chang, "Attosecond time-resolved autoionization of argon", Phys. Rev. Lett. **105**, 143002 (2010).

[82]M. Holler, F. Schapper, L. Gallmann, and U. Keller, "Attosecond electron wave-packet interference observed by transient absorption", Phys. Rev. Lett. **106**, 123601 (2011).

[83]K. Ramasesha, S. R. Leone, and D. M. Neumark, "Real-time probing of electron dynamics using attosecond time-resolved spectroscopy", Annual Review of Physical Chemistry **67**, 41–63 (2016).

[84]S. Chen, M. J. Bell, A. R. Beck, H. Mashiko, M. Wu, A. N. Pfeiffer, M. B. Gaarde, D. M. Neumark, S. R. Leone, and K. J. Schafer, "Light-induced states in attosecond transient absorption spectra of laser-dressed helium", Phys. Rev. A **86**, 063408 (2012).

[85]M. Chini, X. Wang, Y. Cheng, Y. Wu, D. Zhao, D. A. Telnov, S.-I. Chu, and Z. Chang, "Sub-cycle Oscillations in Virtual States Brought to Light", Scientific Reports **3**, 1105 (2013).

[86]C. Ott, A. Kaldun, L. Argenti, P. Raith, K. Meyer, M. Laux, Y. Zhang, A. Blattermann, S. Hagstotz, T. Ding, R. Heck, J. Madronero, F. Martin, and T. Pfeifer, "Reconstruction and control of a time-dependent two-electron wave packet", Nature **516**, 374–378 (2014).

[87]S. G. Sayres, E. R. Hosler, and S. R. Leone, "Exposing the role of electron correlation in strong-field double ionization: x-ray transient absorption of orbital alignment in Xe+ and Xe2+", The Journal of Physical Chemistry A **118**, 8614–8624 (2014).

[88]M. Schultze, E. M. Bothschafter, A. Sommer, S. Holzner, W. Schweinberger, M. Fiess, M. Hofstetter, R. Kienberger, V. Apalkov, V. S. Yakovlev, M. I. Stockman, and F. Krausz, "Controlling dielectrics with the electric field of light", Nature **493**, 75–78 (2013).

[89]M. Schultze, K. Ramasesha, C. Pemmaraju, S. Sato, D. Whitmore, A. Gandman, J. S. Prell, L. J. Borja, D. Prendergast, K. Yabana, D. M. Neumark, and S. R. Leone, "Attosecond band-gap dynamics in silicon", Science **346**, 1348–1352 (2014).

[90]A. D. Dutoi and L. S. Cederbaum, "Time-resolved pump-probe spectroscopy to follow valence electronic motion in molecules: application", Phys. Rev. A **90**, 023414 (2014).

[91]R. Santra, V. S. Yakovlev, T. Pfeifer, and Z.-H. Loh, "Theory of attosecond transient absorption spectroscopy of strong-field-generated ions", Phys. Rev. A **83**, 033405 (2011).

[92]O. Keski-Rahkonen and M. O. Krause, "Total and partial atomic-level widths", Atomic Data and Nuclear Data Tables **14**, 139 –146 (1974).

[93]J. N. Cutler, G. M. Bancroft, and K. H. Tan, The Journal of Chemical Physics **97**, 7932–7943 (1992).

[94]F. Jensen, *Introduction to computational chemistry* (Wiley, 1998).

[95]P.-O. Löwdin, "On the nonorthogonality problem connected with the use of atomic wave functions in the theory of molecules and crystals", The Journal of Chemical Physics **18**, 365–375 (1950).

[96]G. Bruhn, E. R. Davidson, I. Mayer, and A. E. Clark, "Löwdin population analysis with and without rotational invariance", International Journal of Quantum Chemistry **106**, 2065–2072 (2006).

[97]P.-O. Löwdin, "Quantum theory of many-particle systems. i. physical interpretations by means of density matrices, natural spin-orbitals, and convergence problems in the method of configurational interaction", Phys. Rev. **97**, 1474–1489 (1955).

[98]M. B. Plenio and S. S. Virmani, *An introduction to entanglement theory*, edited by E. Andersson and P. Öhberg (Springer International Publishing, Cham, 2014), pp. 173–209.

[99]T. Koopmans, "Über die Zuordnung von Wellenfunktionen und Eigenwerten zu den Einzelnen Elektronen Eines Atoms", Physica **1**, 104 –113 (1934).

[100]J. Breidbach and L. S. Cederbaum, "Migration of holes: formalism, mechanisms, and illustrative applications", The Journal of Chemical Physics **118**, 3983–3996 (2003).

[101]J. E. Bækhøj, L. Yue, and L. B. Madsen, "Nuclear-motion effects in attosecond transient-absorption spectroscopy of molecules", Phys. Rev. A **91**, 043408 (2015).

[102]F. Schwabl, *Quantenmechanik (QM I): Eine Einführung*, Springer-Lehrbuch (Springer Berlin Heidelberg, 2013).

[103]D. Coster and R. D. L. Kronig, "New type of Auger effect and its influence on the X-ray spectrum", Physica **2**, 13 –24 (1935).

[104]A. I. Kuleff, J. Breidbach, and L. S. Cederbaum, "Multielectron wave-packet propagation: general theory and application", The Journal of Chemical Physics **123**, 044111 (2005).

[105]H. Hennig, J. Breidbach, and L. S. Cederbaum, "Electron correlation as the driving force for charge transfer: charge migration following ionization in n-methyl acetamide", The Journal of Physical Chemistry A **109**, 409–414 (2005).

[106]J. Breidbach and L. S. Cederbaum, "Migration of holes: numerical algorithms and implementation", The Journal of Chemical Physics **126**, 034101 (2007).

[107]K. A. Peterson, B. C. Shepler, D. Figgen, and H. Stoll, "On the Spectroscopic and Thermochemical Properties of ClO, BrO, IO, and Their Anions", The Journal of Physical Chemistry A **110**, 13877–13883 (2006).

[108]A. Bergner, M. Dolg, W. Küchle, H. Stoll, and H. Preuß, "Ab initio energy-adjusted pseudopotentials for elements of groups 1317", Molecular Physics **80**, 1431–1441 (1993).

[109]K. A. Peterson, D. Figgen, E. Goll, H. Stoll, and M. Dolg, The Journal of Chemical Physics **119**, 11113–11123 (2003).

[110]A. R. Attar, L. Piticco, and S. R. Leone, "Core-to-valence spectroscopic detection of the ch2br radical and element-specific femtosecond photodissociation dynamics of ch2ibr", The Journal of Chemical Physics **141**, 164308 (2014).

[111]L. S. Cederbaum, J. Schirmer, W. Domcke, and W. von Niessen, "Complete breakdown of the quasiparticle picture for inner valence electrons", Journal of Physics B: Atomic and Molecular Physics **10**, L549 (1977).

[112]J. Schirmer, W. Domcke, L. S. Cederbaum, and W. von Niessen, "Break-down of the molecular-orbital picture of ionization: cs, pn and p2", Journal of Physics B: Atomic and Molecular Physics **11**, 1901 (1978).

[113]E. M. Ohrendorf, F. Tarantelli, and L. S. Cederbaum, "Dicationic states of hydrocarbons and a statistical approach to their Auger spectra", The Journal of Chemical Physics **92**, 2984–2999 (1990).

[114]G. Dixit, O. Vendrell, and R. Santra, "Imaging electronic quantum motion with light", Proceedings of the National Academy of Sciences **109**, 11636–11640 (2012).

[115]G. Dixit, J. M. Slowik, and R. Santra, "Theory of time-resolved nonresonant x-ray scattering for imaging ultrafast coherent electron motion", Phys. Rev. A **89**, 043409 (2014).

[116]H.-C. Shao and A. F. Starace, "Imaging coherent electronic motion in atoms by ultrafast electron diffraction", Phys. Rev. A **88**, 062711 (2013).

[117]A. Wirth, R. Santra, and E. Goulielmakis, "Real time tracing of valence-shell electronic coherences with attosecond transient absorption spectroscopy", Chemical Physics **414**, 149 –159 (2013).

[118]B. Erk, D. Rolles, L. Foucar, B. Rudek, S. W. Epp, M. Cryle, C. Bostedt, S. Schorb, J. Bozek, A. Rouzee, A. Hundertmark, T. Marchenko, M. Simon, F. Filsinger, L. Christensen, S. De, S. Trippel, J. Küpper, H. Stapelfeldt, S. Wada, K. Ueda, M. Swiggers, M. Messerschmidt, C. D. Schröter, R. Moshammer, I. Schlichting, J. Ullrich, and A. Rudenko, "Inner-shell multiple ionization of polyatomic molecules with an intense x-ray free-electron laser studied by coincident ion momentum imaging", Journal of Physics B: Atomic, Molecular and Optical Physics **46**, 164031 (2013).

[119]R. Boll, B. Erk, R. Coffee, S. Trippel, T. Kierspel, C. Bomme, J. D. Bozek, M. Burkett, S. Carron, K. R. Ferguson, L. Foucar, J. Küpper, T. Marchenko, C. Miron, M. Patanen, T. Osipov, S. Schorb, M. Simon, M. Swiggers, S. Techert, K. Ueda, C. Bostedt, D. Rolles, and A. Rudenko, "Charge transfer in dissociating iodomethane and fluoromethane molecules ionized by intense femtosecond x-ray pulses", Structural Dynamics **3**, 043207 (2016).

[120]W. Ackermann et al., "Operation of a free-electron laser from the extreme ultraviolet to the water window", Nat. Photon. **1**, 336–342 (2007).

[121]K. Tiedtke, A. Azima, N. von Bargen, L. Bittner, S. Bonfigt, S. Dusterer, B. Faatz, U. Fruhling, M. Gensch, C. Gerth, N. Guerassimova, U. Hahn, T. Hans, M. Hesse, K. Honkavaar, U. Jastrow, P. Juranic, S. Kapitzki, B. Keitel, T. Kracht, M. Kuhlmann, W. B. Li, M. Martins, T. Nunez, E. Plonjes, H. Redlin, E. L. Saldin, E. A. Schneidmiller, J. R. Schneider, S. Schreiber, N. Stojanovic, F. Tavella, S. Toleikis, R. Treusch, H. Weigelt, M. Wellhöfer, H. Wabnitz, M. V. Yurkov, and J. Feldhaus, "The soft x-ray

free-electron laser FLASH at DESY: beamlines, diagnostics and end-stations", New Journal of Physics **11**, 023029 (16pp) (2009).

[122]D. E. Parry, "Atomic calculation of photoionization cross-sections and asymmetry parameters", Rapid Communications in Mass Spectrometry **8**, 579–579 (1994).

[123]F. Tarantelli, A. Sgamellotti, and L. S. Cederbaum, "Many dicationic states and two-hole population analysis as a bridge to Auger spectra : Strong localization phenomena in BF3", The Journal of Chemical Physics **94**, 523–532 (1991).

[124]A. Bergner, M. Dolg, W. Küchle, H. Stoll, and H. Preuß, "Ab initio energy-adjusted pseudopotentials for elements of groups 13–17", Molecular Physics **80**, 1431–1441 (1993).

[125]Z. Li, O. Vendrell, and R. Santra, "Ultrafast charge transfer of a valence double hole in glycine driven exclusively by nuclear motion", Phys. Rev. Lett. **115**, 143002 (2015).

[126]N. V. Golubev and A. I. Kuleff, "Control of charge migration in molecules by ultrashort laser pulses", Phys. Rev. A **91**, 051401 (2015).

[127]A. I. Kuleff, N. V. Kryzhevoi, M. Pernpointner, and L. S. Cederbaum, "Core ionization initiates subfemtosecond charge migration in the valence shell of molecules", Phys. Rev. Lett. **117**, 093002 (2016).